Sea Surface Height Signatures of Internal Gravity Waves

by

Anna Savage

A dissertation submitted in partial fulfillment
of the requirements for the degree of
Doctor of Philosophy
(Applied Physics)
in The University of Michigan
2017

Doctoral Committee:

Associate Professor Brian Arbic, Chair
Associate Professor Mark Flanner
Assistant Professor Eric Kort
Research Scientist James Richman, Florida State University
Professor Richard Rood

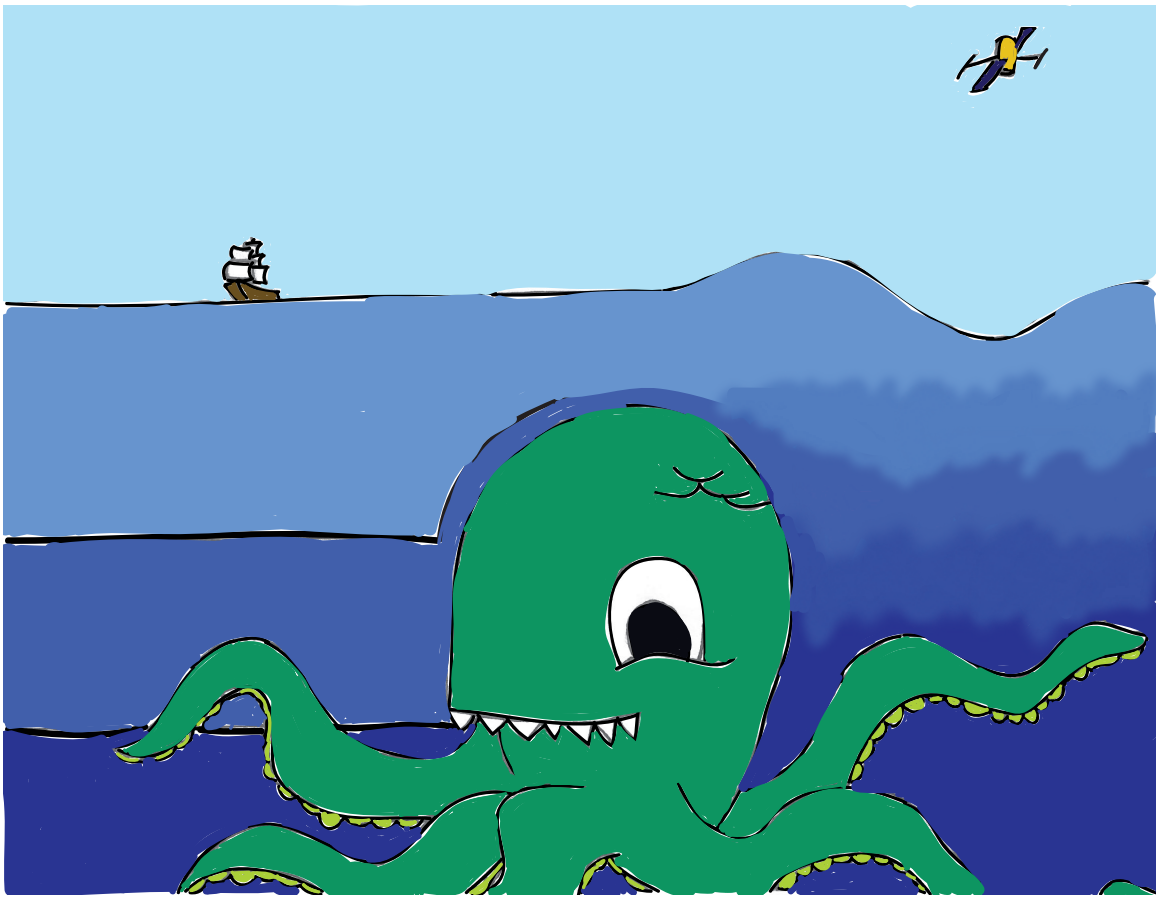

Anna C. Savage

savagea@umich.edu

ORCID iD: 0000-0003-1288-8636

For Mr. DaCorte, my high school physics teacher.

ACKNOWLEDGEMENTS

The number of people who made this thesis possible is truly immense. On the top of that list, however, is Brian Arbic, without whom I could not have realized my potential as a scientist. Thank you also to my thesis committee for helping me through the final steps of my degree. I'd also like to thank a large number of collaborators, including those who ran these massive models and collected and archived the data used in this thesis. Included in this are my many coauthors: Joseph Ansong, Matthew Alford, Maarten Buijsman, Tom Farrar, Dimitris Menemenlis, Amanda O'Rourke, Jim Richman, Hari Sharma, Jay Shriver, Gunnar Voet, Alan Wallcraft, and Luis Zamudio. A special thanks to all of the lab group members who have been in the Ocean Modeling Lab during my tenure, who made the work environment fun and friendly and who taught me so much about linear algebra and writing Matlab code.

A big shout out to my friends, from all the different times in my life, who offered support (and sometimes housing, food, and moving assistance) whenever they could. An especially giant thanks to the friends I've made in grad school, who filled these past six years with great food, ski trips, frisbee, river flotillas, and some pretty terrible movies. I also share my gratitude to my parents and my brother, who've always encouraged me to defy expectations. And finally, a special thanks to Daniel Barter, from whom I learned absolutely everything I know about both partnership and representation theory.

TABLE OF CONTENTS

LIST OF FIGURES

Figure

LIST OF TABLES

Table

LIST OF APPENDICES

Appendix

ABSTRACT

Sea surface height signatures of internal gravity waves

by

Anna Savage

Chair: Brian Arbic

Sea surface height (SSH) is a fundamental variable in physical oceanography and is the key observable quantity in global satellite altimetry. SSH is a complicated manifestation of many oceanic processes, and, as such, exhibits variability over a wide range of space and time scales. It is well known that tides are of first order importance in SSH, but SSH contributions outside of this narrow band are also of great interest. Satellite altimetry has become an invaluable tool in the study of the global ocean. However, the long repeat period (of order ten to 40 days) of altimeters implies that high-frequency motions will be aliased in altimeter records. In order to study the lower-frequency SSH variability, the aliased high-frequency variability must first be accurately removed. Some of these high-frequency motions, such as the stationary component of surface and internal tides, can be adequately removed even from aliased records, via harmonic analysis or response methods, as long as the signal-to-noise ratio is relatively high. However, the challenge of removing SSH signals associated with motions that are less predictable, for instance, the non-stationary component of the internal tides, or the internal gravy wave (IGW) continuum, is much greater. To quantify the magnitude of this challenge, high resolution global general circulation

ocean models are used to simulate and study internal tides, the IGW continuum, and other contributions to sea surface variability. Using these models, we examine the space- and time-scales of SSH variability. For instance, we compute frequency-horizontal wavenumber ($\omega - K$) spectral densities over a several oceanic regions that collectively represent different regimes of global ocean variability. These $\omega - K$ spectral densities show high energy along lines representing the linear dispersion relations predicted by the Sturm-Liouville problem for internal waves. In many oceanic regions, the high-frequency motions dominate the small-scale (high-wavenumber) SSH spectra. This has implications for upcoming wide-swath satellite altimeter missions, which will focus on high-wavenumber SSH spectra. In addition to quantifying the frequency-horizontal wavenumber spectral densities, we estimate the SSH variance in subtidal, tidal, and supertidal phenomena through the use of frequency spectral densities. This temporally driven approach allows us to create global maps of SSH variance in these frequency bands. The global band-integrated maps are further divided into steric and non-steric SSH components, which further helps to delineate different classes of oceanic motions. These global band-integrated maps provide both results consistent with previous studies (e.g., of subtidal steric SSH, dominated by mesoscale eddies and well-measured by current generation satellite altimeters), as well as unprecedented global maps of the non-stationary component of the internal tides and of the IGW continuum. As global general circulation ocean models have only begun to be able to partially resolve the IGW continuum, we believe that our estimate represents a lower bound of variance in the IGW continuum, and will likely increase with increased horizontal and vertical resolution of ocean models. Indeed, comparisons of the models used here with in-situ data strongly suggest that the models used here underestimate the IGW continuum, while representing other motions with a higher accuracy.

CHAPTER I

Introduction

1.1 Internal gravity waves

In geophysical fluid dynamics, a gravity wave is defined simply as a wave for which gravity acts as the restoring force. An internal gravity wave, or IGW, is a gravity wave that has its maximal signals in the interior of a fluid, as opposed to at the surface of the fluid. Internal gravity waves can only propagate in stratified fluids. In the ocean, stratification is generally dominated by temperature, although salinity also plays an important role, and tends to be more important than temperature in high-latitude conditions. The continuous stratification of the ocean is often approximated in models with a discrete set of layers that become progressively denser with depth. Internal gravity waves take place at the interfaces of these layers and the at-depth amplitudes of these waves can be as large as 100 m (*Alford et al.*, 2015). These large amplitude IGWs can be caused by a variety of internal and surface ocean dynamics. Barotropic tides, the signals of large water mass movements caused primarily by the gravitational pull of moon, are a large driver of internal gravity waves. The IGWs in the Luzon Strait and north of the Hawai'ian islands, for example, are caused primarily by the barotropic tide flowing over rough topography (*Ray and Mitchum*, 1997). Internal gravity waves with frequencies equal to the frequencies of barotropic tidal constituents are known as internal, or baroclinic tides. As with the barotropic

tides they are forced by, internal tides can be either semidiurnal (twice per day), or diurnal (once per day). Ocean currents, such as western boundary currents, can also create IGWs as they flow over rough topography. Internal gravity waves also result from wind blowing over the surface of the ocean. Such waves are called near-inertial waves and have a frequency close to the Coriolis parameter f, to be defined later (*D'Asaro*, 1984). As IGWs break, they facilitate mixing across stratified layers and contribute to the total energy dissipation within the ocean interior. IGWs are of interest due to the control they exert over deep ocean mixing (*Munk and Wunsch*, 1998; *Ferrari and Wunsch*, 2009); a control which covers a large range of space and time scales (*Garrett and Munk*, 1972; *Whalen et al.*, 2012).

While IGWs can have at-depth interface displacement signatures as large as 100 m, their signatures at the surface are often only a few centimeters. These sea surface height (SSH) signatures arise from baroclinic flow, defined as the displacement from barotropic, or depth-averaged, flow. Steric SSH is sea surface height due to baroclinic motions, or variations in the temperature and salinity structure of the water column. These variations can be caused by phenomena such as fronts and eddies, as well as IGWs. The steric SSH can be computed from temperature and salinity measurements that span the entire water column. In-situ instruments that measure temperature and salinity in the vertical, such as stationary moorings and mobile floats, are generally not able to cover all ocean depths at all times, even in one location. The calculation for dynamic height, which will be discussed in Chapter II, specifically Equation 2.4, is similar to that of steric SSH, but can be computed over any pressure interval in the water column. This similarity can be used to gain useful information about steric SSH using available vertically sampled data.

As IGWs cover a wide range of time scales, we often refer to the IGW continuum to describe IGWs that span frequencies (ω) between the buoyancy and inertial frequencies ($N < \omega < f$), to be defined later. Recently, high-resolution ocean models

forced by both atmospheric fields and tides (*Arbic et al.*, 2010, 2012) have begun to resolve the IGW continuum (*Müller et al.*, 2015). In *Müller et al.* (2015), two simulations of the HYbrid Coordinate Ocean Model (HYCOM; *Chassignet et al.*, 2009) were compared against an array of moorings in the North Pacific. Frequency spectral densities of surface kinetic energy computed from 1/12.5° and 1/25° simulations of HYCOM, and from a mooring, were shown against the Garrett-Munk spectral slope (*Garrett and Munk*, 1975) for internal waves, that varies as ω^{-2}. The moorings most closely match the theoretical slope, followed by the spectral density computed from the 1/25° simulation of HYCOM. *Müller et al.* (2015) also showed kinetic energy frequency-horizontal wavenumber spectral density computed from a box in the North Pacific in 1/25° HYCOM. This showed peaks at the near-inertial and semidiurnal bands, and significant energy along the linear dispersion relation curves for IGWs (described in Section 3.2.2), the latter in accordance with the notion that an IGW spectrum is developing. Additionally, the nonlinear kinetic energy transfers in frequency-horizontal wavenumber space computed in *Müller et al.* (2015) showed that energy is being extracted from near-inertial and semidiurnal frequencies and added at high-frequencies along the linear dispersion curves for internal waves. *Müller et al.* (2015) was the first study to demonstrate that high-resolution general circulation global ocean models with tidal and atmospheric forcing are beginning to resolve the IGW continuum. The work done here builds upon the findings in *Müller et al.* (2015), and examines the SSH signatures of internal gravity waves, using high-resolution ocean models as well as observational data.

1.2 Ocean mixing and global climate

To quote *Ferrari and Wunsch* (2009), "That turbulent mixing processes in the ocean are extremely important in determining the oceanic general circulation, and are major limiting factors in the ability to calculate future climate states, is a cliché in

oceanography and climate dynamics. Unlike some other hackneyed statements, this one does retain much of its validity." This is due, in great part, to the ocean's role as a heat engine; aiding the atmosphere in the redistribution of heat from warm equatorial regions to cold polar regions, known as meridional heat transport. Meridional heat transport in the ocean accounts for a little less than half of the heat transported poleward by both the atmosphere and ocean, and is the key means of transport at low latitudes (*Hastenrath*, 1982). At the surface, poleward heat transport is acheived in the strong western boundary currents, such as the Gulf Stream and Kuroshio currents. The Atlantic, like other ocean basins, participates in the global meridional overturning circulation. The Atlantic branch is known as the Atlantic Meridional Overturning Circulation (AMOC). After warm water is transported poleward via western boundary currents, cold water must return equatorward to complete the circulation. Cold, dense water in the North Atlantic sinks to depth due to the bouyancy driven convection, and travels toward the equator as North Atlantic Deep Water. This water is then mixed with warmer tropical and subtropical water, and brought to the surface, or upwelled. The upwelling brings nutrient rich water from the deep ocean to the surface, supporting marine life in the upper ocean. Abyssal mixing due to processes including the breaking of IGWs is thought to provide $\sim 0.4\,\mathrm{TW}$ of the $2.1\,\mathrm{TW}$ necessary to maintain circulation of the global meridional overturning circulation (*Munk and Wunsch*, 1998; *Wunsch and Ferrari*, 2004), and contributes greatly to the upwelling in tropical and subpolar regions. The AMOC, along with other branches of global meridional overturning circulation, sets up a sort of conveyer belt that transports not only temperature, but oxygen and nutrients as well. Abrupt changes in these gyres have large impacts on our global climate (*Alley*, 2007), as they help maintain the redistribution of the global heat budget.

As well as playing a large role in meridional heat transport, the ocean has been observed to absorb excess heat introduced to the atmosphere by anthropogenic activities

over the last century (*Levitus et al.*, 2001). Between the years of 1955-1996, the heat content of the ocean increased by approximately an order of magnitude more than the heat content of the atmosphere, implying that the ocean has essentially acted as a buffer for the atmosphere and has helped to moderate global atmospheric temperatures. In addition to heat, the ocean has acted as a large carbon dioxide sink. The rate of carbon dioxide increase in the atmosphere is only half of the rate produced by anthropogenic activity (*Houghton et al.*, 2001), while the other half has been absorbed into land and ocean. The ocean is the primary sink of carbon dioxide and certain high absorption areas are becoming saturated. This saturation decreases the rate at which these high absorption areas subsume excess carbon dioxide (*Le Quéré et al.*, 2007). Upper ocean mixing (*Moum and Smyth*, 2000), caused in part by breaking IGWs and breaking surface waves, plays an important role in dissipating heat energy and vertically mixing carbon dioxide, and thus contributes to the distribution of heat and carbon dioxide throughout the ocean interior. The consequences of changes in oceanic heat and carbon dioxide uptake include great changes to ocean biogeochemistry. The additional heat and ocean acidification caused by excess carbon dioxide have lead to the deterioration and bleaching of many tropical reefs, including the Great Barrier Reef, which has supported many endangered and endemic species, and has experienced eight massive bleaching events since 1979 (*Hennessy et al.*, 2007). These bleaching events have large effects on the local biodiversity, which can, in turn, effect the health of the global ocean.

1.3 Satellite altimetry

Although the most effective way to measure ocean mixing is via in-situ instrumentation, this method suffers from severe spatial limitations. Ship board instruments offer a unique opportunity to analyze frequently sampled oceanographic data, but only at limited times and in limited locations. Autonomous vehicles, such as Argo

floats (*Roemmich and Owens*, 2000), have helped to vastly improve the spatial coverage of in-situ data, sampling globally on a relatively coarse $\sim 3^\circ$ grid. This grid spacing prohibits study of small scale ocean dynamics, including parts of the internal gravity wave continuum.

As of the 1960s, satellites have been developed to collect data from the ocean surface, such as temperature, salinity, chlorophyll, and sea surface height anomalies. Satellite altimetry, which provides near-global coverage of sea surface height, is an invaluable tool in the study of the global ocean (*Fu and Cazenave*, 2001). Many studies have used in-situ data in tandem with altimeter data. For example, *Wunsch* (1991) used both types of data to examine global SSH variability, and *Ray and Mitchum* (1997) used tide gauges and altimetry to examine internal tides. Altimeters have also been used in tandem with other satellite missions, such as *Chambers* (2006), which used the Gravity Recovery and Climate Experiment, GRACE satellite, in conjunction with the current altimeter technology to study the seasonal variability of steric SSH.

Satellite altimetry has enabled global-scale examination of SSH, including calculations of SSH wavenumber spectral density whose slope has been used to diagnose low-frequency dynamics of the ocean surface (*Stammer*, 1997; *Le Traon et al.*, 2008; *Sasaki and Klein*, 2012; *Richman et al.*, 2012; *Xu and Fu*, 2012). Swath altimetry, as in the upcoming Surface Water and Ocean Topography (SWOT) satellite mission, is unlike current altimeter technology, which samples SSH along one-dimensional tracks. Swath altimetry will sample SSH along two-dimensional swaths, which, for SWOT, will measure 100 km wide with 1 km x 1 km pixels (*Fu et al.*, 2012). These swaths will provide a new opportunity to compute SSH wavenumber spectral density from two-dimensional data (*Fu et al.*, 2012). There is growing interest in the satellite altimeter community in the SSH signatures of internal tides and the IGW continuum, particularly because internal tides and IGWs have significant variance at high wavenumbers (*Richman et al.*, 2012; *Callies and Ferrari*, 2013; *Rocha et al.*, 2016a).

These high wavenumbers are targeted for study by planned two-dimensional swath altimeter missions (*Fu et al.*, 2012). As with previous altimeter missions, SWOT will suffer from infrequent temporal sampling and will therefore alias the SSH signatures of high-frequency motions, such as internal tides and the internal gravity wave continuum. The aliasing of such motions contaminates low-frequency signals in altimeter data (*Ray and Byrne*, 2010; *Shriver et al.*, 2012). Because the non-stationary internal tides and the IGW continuum are less predictable than the stationary internal tides, they may represent an even greater challenge to the altimetry community than do stationary internal tides. Additionally, maps of SSH signatures of internal gravity waves may aid in locating regions of high mixing activity.

1.4 Overview

Here we aim to develop estimates of SSH variance in internal tides and the internal gravity wave continuum through analysis of frequency, frequency-horizontal wavenumber, and horizontal wavenumber spectral densities. We differentiate ocean dynamics by frequency using four bands; a low-frequency band (subtidal), two tidal bands (diurnal and semidiurnal), and a high-frequency band (supertidal). These bands are shown over an example frequency spectral density of total SSH in Figure 1.1. The division of SSH dynamics into these frequency bands, and into steric and non-steric components (non-steric being total SSH minus steric SSH, and related to barotropic flow), aids in assigning variance to different phenomena. For example, subtidal steric and non-steric SSH signatures include mesoscale eddies and seasonal effects, the two tidal bands include SSH signatures of both barotropic (non-steric) and baroclinic (steric) tides, and steric and non-steric SSH signatures in the supertidal band include higher harmonics of tides and the IGW continuum.

In Chapter II, we compare two high-horizontal resolution ocean models to two different datasets. Two simulations of the HYbrid Coordinate Ocean Model (HY-

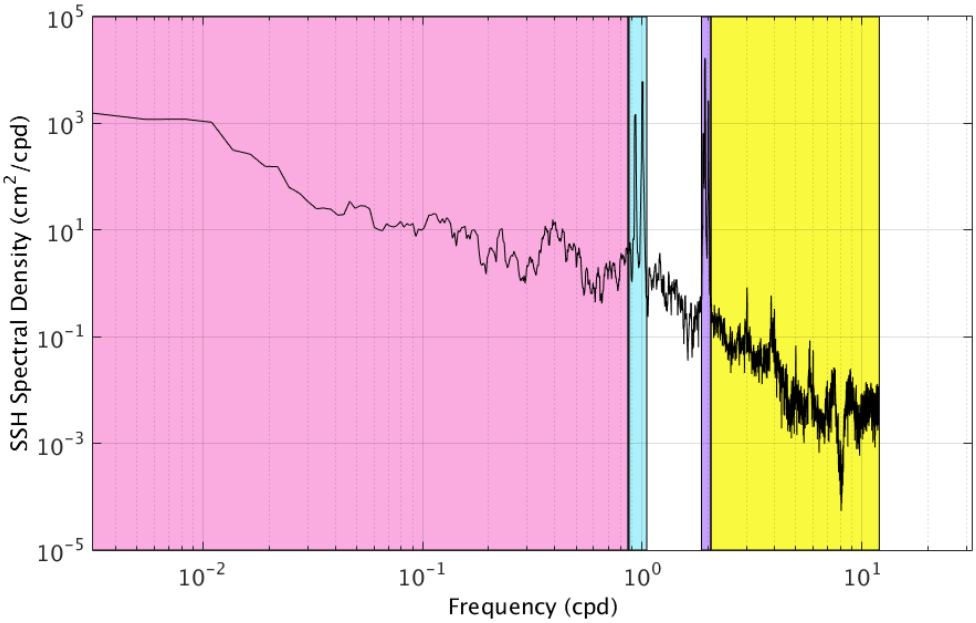

Figure 1.1: Example frequency spectral density of total SSH from the 1/25° simulation of HYCOM near Hilo, Hawai'i (204.96E, 19.70N) with colors shading the frequency bands used in this study. The pink region represents the subtidal band, the teal region is the diurnal band, the purple region is the semidiurnal band, and the yellow region represents the supertidal band. Reprited from *Savage et al.* (2017a).

COM; *Chassignet et al.*, 2009) and one simulation of the Massachusetts Institute of Technology general circulation model (MITgcm; *Marshall et al.*, 1997), general circulation models forced both by atmospheric fields and tides, are compared to two in-situ data sets. We compared the frequency spectral density in HYCOM to the frequency spectral density computed from a collection of 351 globally distributed tide gauges. We also compare HYCOM, as well as MITgcm, to a collection of nine in-situ profiling instruments. These instruments sample temperature and salinity at high temporal and vertical resolution. From this we compare frequency spectral densities of dynamic height—a quantity similar to steric SSH, that can be computed over any pressure interval. The comparison of HYCOM to tide gauges has been published in *Savage et al.* (2017a), while the comparison of HYCOM and MITgcm to in-situ depth profiling instruments has been submitted in *Savage et al.* (2017b).

In Chapter III, we analyze SSH variance frequency-horizontal wavenumber spectral density to demonstrate that high-frequency, high-wavenumber dynamics in the simulations are primarily a result of internal gravity waves. We compare the frequency-horizontal wavenumber spectral densities from seven regions around the globe in five simulations of HYCOM and MITgcm. We then integrate the frequency-horizontal wavenumber spectral densities over three frequency bands–subtidal, tidal and supertidal–to examine which frequencies dominate at the large wavenumbers (small spatial scales) of interest for the upcoming SWOT mission. The results in this chapter were submitted in *Savage et al.* (2017b).

In Chapter IV, we take advantage of the global coverage of HYCOM to create maps of SSH variability in non-steric and steric SSH attributable to a variety of phenomena in the ocean. We compute pointwise frequency spectral densities from a subsampled $1/4^\circ$ global map and integrate over the four frequency bands shown in Figure 1.1. This method allows us to recreate maps of the SSH signatures of several classes of well-documented oceanic motions, as well as create new global estimates of

supertidal steric SSH variance, dominated by the internal gravity wave continuum, as shown in Chapter III. The global maps in this chapter were published in *Savage et al.* (2017a).

The final chapter, Chapter V, contains a summary of our findings and a discussion on their bearings on ocean mixing and satellite altimetry. As much of the work described here has been previously published, some of the passages are rewritten verbatim from *Savage et al.* (2017a,b). Additionally, all of the following figures have been reprinted from *Savage et al.* (2017a,b), identified in the figure captions.

CHAPTER II

Validation of two high-resolution global ocean models

"Essentially, all models are wrong, but some are useful."

- George Box

2.1 Introduction

In order to determine the accuracy of global general circulation ocean models in representing true ocean dynamics, it is necessary to compare them against observational data. Several model-data comparisons have been performed with the HYbrid Coordinate Ocean Model (HYCOM; *Chassignet et al.*, 2009) tidal simulations. These studies include a comparison of barotropic and internal tide SSH signatures to altimetry (*Shriver et al.*, 2012; *Stammer et al.*, 2014; *Ansong et al.*, 2015; *Ngodock et al.*, 2016), comparison of surface tidal elevations to pelagic tide gauges (*Stammer et al.*, 2014), comparison of tidal currents to moored current meter records (*Timko et al.*, 2012, 2013; *Stammer et al.*, 2014), comparison of internal gravity wave (IGW) kinetic energy frequency spectral densities to current meter spectral densities (*Müller et al.*, 2015), and comparison of baroclinic tidal energy fluxes to fluxes computed from current meter records (*Ansong et al.*, 2017). The MIT general circulation model

(MITgcm; *Marshall et al.*, 1997) tidal simulations are newer than the HYCOM tidal simulations, and have received much less vetting. The accuracy of the barotropic and internal tides has not yet been tested on a global scale. Published model-data comparisons to date are limited to a Drake Passage study (*Rocha et al.*, 2016a), which compared along-track wavenumber spectra of kinetic energy in a high-horizontal resolution simulation of MITgcm versus Acoustic Doppler Current Profiler data, and a Kuroshio Extension study (*Rocha et al.*, 2016b), which established that the upper ocean stratification and variability in that region is well captured by several MITgcm simulations.

To test model accuracy in both coastal and open-ocean regions, we compare model output to tide gauge and in-situ depth profiling observations. We compare the sea surface height (SSH) frequency spectral densities computed from HYCOM to those computed from 351 tide gauges in a global database over all frequencies. Additionally, we compare the frequency spectral densities of dynamic height computed from HYCOM, from MITgcm and from 9 in-situ depth-profiling instruments. The small number of in-situ depth-profiling instruments used here feature high-frequency sampling in time as well as high vertical resolution, thus enabling a model-data comparison of dynamic height over tidal and supertidal bands. The tide gauge and in-situ vertical profiler datasets we use here are the only observational datasets we are aware of that offer a wide (quasi-global, in the case of the tide gauges) geographical coverage at the same time that they cover a wide range of frequencies. For this reason, we compare model output to both tide gauge and in-situ vertical profiler datasets, while being fully aware that the two datasets are rather distinct.

2.2 Models and observations

2.2.1 HYCOM simulations

General information about HYCOM can be found in *Chassignet et al.* (2009). Two simulations of HYCOM are used in this study: one with a 1/12.5° horizontal resolution (HYCOM12; $\sim 8\,\text{km}$), the other with a 1/25° horizontal resolution (HYCOM25; $\sim 4\,\text{km}$). The hybrid coordinate vertical layers, that define models such as HYCOM, are a combination of three popular vertical layer schemes: (1) z-layer coordinates which are defined by depth, (2) isopycnals coordinate, which are defined by density, and (3) σ cooridinates, which follow bottom topography. The hybrid coordinate system uses all three schemes where appropriate. HYCOM uses z-layer coordinates in the upper ocean, isopycnal coordinates in the open interior ocean, and σ-coordinates in coastal and deep open ocean regions. Both simulations have 41 hybrid layers in the vertical direction. The atmospheric fields, including atmospheric pressure, buoyancy, and wind forcing, used in both HYCOM simulations are taken from the U.S. Navy Global Environmental Model, NAVGEM (*Hogan et al.*, 2014). HYCOM25 is forced by NAVGEM every three hours while HYCOM12 is forced hourly. The HYCOM simulations are forced using a 0.5° application grid interpolated from NAVGEM's primary 37 km grid. The HYCOM simulations are simultaneously forced by the astronomical tidal potential (*Cartwright*, 1999) of the two largest diurnal constituents (K_1 and O_1) and the three largest semidiurnal constituents (M_2, S_2, and N_2). The five tidal constituents used in the HYCOM simulations account for $\sim 97\%$ of the global variance in the ten largest tidal constituents in the Global Ocean Tide Model (GOT99.2; *Ray* (1999)). A Smagorinsky scheme, in which viscosity is nonlinearly dependant on velocity, is used for vertical viscosity (*Smagorinsky*, 1993). For horizontal diffusivity, a Laplacian scheme is used, while a K-Profile Parametrization (KPP) scheme is used for vertical diffusivity and viscosity (*Large et al.*, 1994). The

self-attraction and loading (SAL, *Hendershott* (1972)) term is computed iteratively as described in *Buijsman et al.* (2015). A topographic wave drag field, a parameterization for flow over rough topography used to dissipate energy in the deep ocean, is taken from *Jayne and St. Laurent* (2001). The wave drag field is tuned to minimize barotropic tidal errors with respect to the altimeter-constrained tide model TPXO (*Egbert et al.*, 1994). The same wave drag tuning computed for HYCOM12 was used for HYCOM25. A description of the wave drag tuning can be found in *Buijsman et al.* (2015), and more information on the importance of the wave drag on barotropic and baroclinic tides can be found in *Ansong et al.* (2015) and *Buijsman et al.* (2016). An Augmented State Ensemble Kalman Filter is implemented in both simulations to reduce the global RMS error of M_2 barotropic tidal elevations in waters deeper than 1 km, with respect to TPXO, to approximately 2.6 cm (*Ngodock et al.*, 2016). The HYCOM output is saved hourly for one full year, yielding $\sim$ 1 TB of SSH fields for HYCOM25. HYCOM12 output spans October 2011 through September 2012, while HYCOM25 output spans January 2014 through December 2014. The difference in record periods has little effect on the frequency spectral densities used for analysis, as both simulations have one year record durations.

2.2.2 MITgcm simulations

Three global ocean simulations of MITgcm (*Marshall et al.*, 1997) are used in this study: one with 1/12° (3-9 km) horizontal grid spacing (hereinafter MITgcm12), one with 1/24° (2-5 km) grid spacing (MITgcm24), and one with 1/48° (.75-2.3 km) grid spacing (MITgcm48). While only the highest resolution simulation of MITgcm is compared to in-situ data in this chapter, the 1/12° and 1/24° simulations used in Chapter III are described here. All three simulations have 90 z-levels in the vertical direction with thicknesses ranging from 1 m at the surface to 480 m near the bottom at a maximum model depth of 7 km. Bathymetry is from *Smith and Sandwell* (1997)

Version 14.1 and IBCAO Version 2.23 (*Jakobsson et al.*, 2008). The model is forced at the surface with six-hourly atmospheric fields from the 0.14° European Center for Medium-Range Weather Forecasts (ECMWF) atmospheric operational model analysis, which, starting in 2011, is converted to surface fluxes using the bulk formulae of *Large and Yeager* (2004). Over ice-covered regions, ocean surface fluxes are computed using the sea ice model of *Losch et al.* (2010). The model includes atmospheric pressure forcing and tidal forcing for 16 tidal constituents, the latter applied to MITgcm as additional atmospheric pressure forcing (*Ponte et al.*, 2015). The 16 tidal constituents are made up of 8 long-period tides, (M_t, M_f, M_m, M_{sm}, M_{sf}, S_{sa}, S_s, and L_n) and the 8 largest diurnal (K_1, O_1, P_1, and Q_1) and semidiurnal (M_2, S_2, N_2, and K_2) tidal constituents. An enstrophy conserving Leith scheme (*Leith*, 1996) is used for horizontal diffusivity and a KPP scheme is used for vertical diffusivity (*Large et al.*, 1994). The MITgcm12 simulation is initialized on January 1, 2010 from a data constrained 1/6° simulation provided by the Estimating the Circulation and Climate of the Ocean, Phase II (ECCO2) project (*Menemenlis et al.*, 2008) and integrated for one year without tides with ERA-Interim (*Dee et al.*, 2011) surface boundary conditions. The application of tidal forcing and atmospheric boundary conditions from the 0.14° ECMWF analysis starts on January 1, 2011. The MITgcm24 simulation is initialized from MITgcm12 fields on January 17, 2011. The MITgcm48 simulation is initialized from MITgcm24 fields on September 10, 2011. In this study, we use 90 days of hourly model output from the three MITgcm simulations for the following periods: March 1, 2014 through May 29, 2014 for MITgcm12 and October 31, 2011 through January 28, 2012 for MITgcm24 and MITgcm48. The horizontal resolution and record times for each HYCOM and MITgcm simulation are listed in Table 2.1 for reference.

Model	Horizontal resolution	Record times
HYCOM12	1/12.5°	October 1, 2011-September 31, 2012
HYCOM25	1/25°	January 1, 2014-December 31, 2014
MITgcm12	1/12°	March 1, 2014-May 29, 2014
MITgcm24	1/24°	October 31, 2011-January 28, 2012
MITgcm48	1/48°	October 31, 2011-January 28, 2012

Table 2.1: Horizontal resolution and record times of the five simulations used to compute frequency-horizontal wavenumber spectral densities. Reprinted from *Savage et al.* (2017b).

2.2.3 Tide Gauge Data

The tide gauge data are taken from the University of Hawai'i Sea Level Center (UHSLC) tide gauge database (*Caldwell et al.*, 2015). We use hourly tide gauge data, to match the hourly HYCOM output. For each tide gauge, one year of continuous data is extracted from the UHSLC database. The HYCOM output used for comparison with the tide gauges is taken at the nearest neighbor model gridpoints corresponding to the tide gauge locations. The one-year time period is dictated by the duration of available tide gauge records in the UHSLC database as well as the duration of available HYCOM output. Out of almost $1,000$ tide gauges in the UHSLC database, 351 tide gauge locations meet our criteria of having one year of continuous hourly output. A map of the 351 locations is given in Figure 2.1a. As seen in Figure 2.1a, there is a noticeable continental coastal bias in the tide gauge locations. At each tide gauge location, the most recent full year of hourly data was chosen for comparison. A histogram of the years covered by the tide gauge data is shown in Figure 2.1b. The majority of the tide gauges used cover years in the 21st century.

2.2.4 McLane profilers

The locations of the 9 McLane profilers (*Doherty et al.*, 1999) used in this study are given in Table 2.2. The profilers are clustered in three regions in the Pacific:

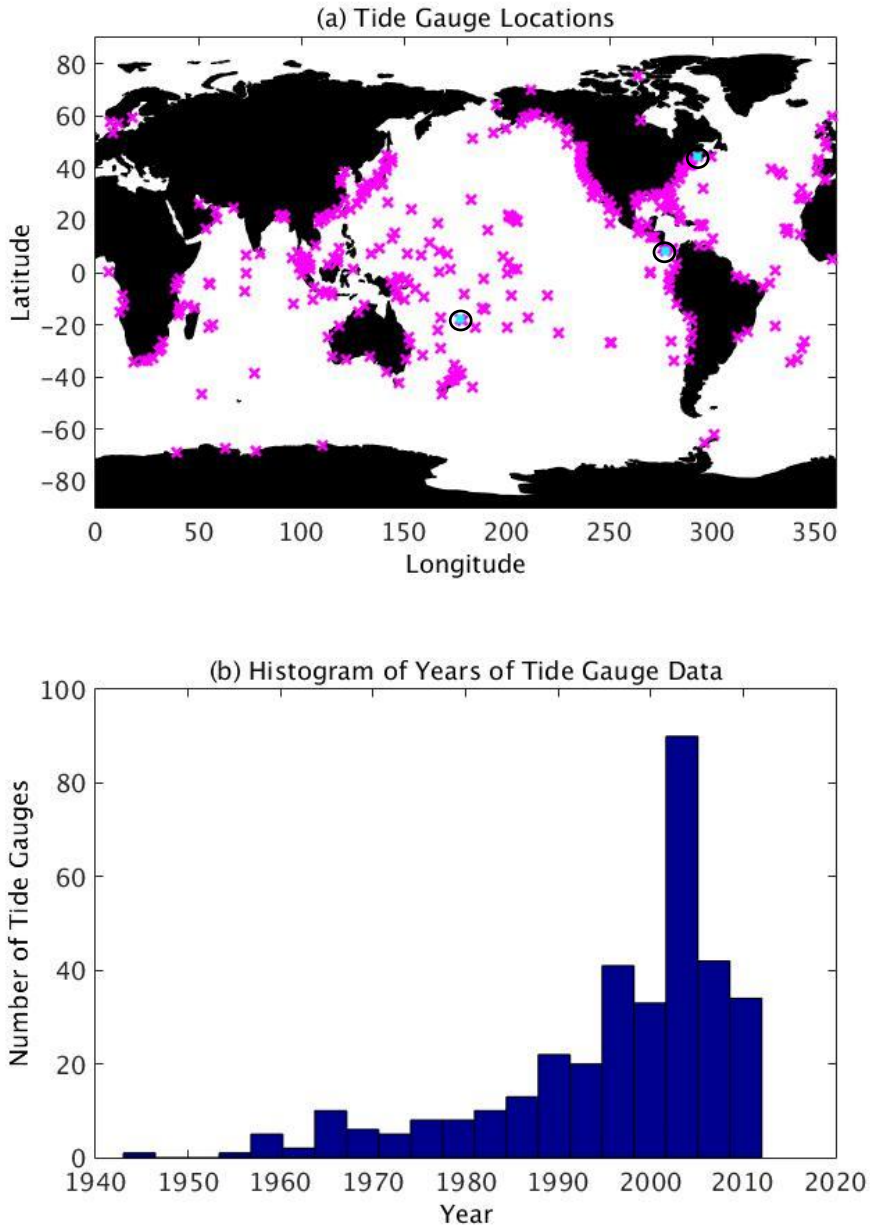

Figure 2.1: (a) Map of 351 tide gauges used in comparison of full SSH variance with HYCOM results. The locations marked with the filled cyan squares (circled in black for emphasis) are used for comparison in Figure 2.3. Longitude (latitude) is measured in degrees north (east) in Figures 2.1 and 2.5. All tide gauges are in the University of Hawai'i Sea Level Center (UHSLC) database. Only gauges with one year of continuous hourly data are used here. (b) Histogram of years of data collected from the UHSLC tide gauge database. Reprinted from *Savage et al.* (2017a).

Profiler	Longitude	Latitude	Min. Pressure	Max. Pressure	Start Date	Record Length
a	$194.8°E$	$25.5°N$	97	1403	Apr 25, 2006	36
b	$196.5°E$	$28.9°N$	97	1418	May 10, 2006	34
c	$197.1°E$	$30.1°N$	97	1430	Apr 25, 2006	22
d	$200.8°E$	$37.1°N$	97	1410	Apr 25, 2006	22
e	$121.0°E$	$19.3°N$	373	1223	June 17, 2011	51
f	$117.9°E$	$20.9°E$	111	1303	May 6, 2007	31
g	$233.7°E$	$43.2°N$	138	2121	Sept 15, 2005	40
h	$234.9°E$	$43.9°N$	73	1332	Sept 14, 2005	40
i	$235.0°E$	$43.2°N$	236	1063	Sept 13, 2005	40

Table 2.2: Location, minimum and maximum pressures (db), start date, and record length (days) for each of the nine McLane profilers used in this study. Profilers a-d are located in the North Pacific, profilers e and f are located in the Luzon Strait, and profilers g-i are located off the Oregon coast of the United States. Reprinted from *Savage et al.* (2017b).

profilers a-d are located in the central North Pacific near Hawai'i (*Alford et al.*, 2007; *Zhao et al.*, 2010; *MacKinnon et al.*, 2013a,b), profilers e and f are located in the Luzon Strait (*Alford et al.*, 2011), and profilers g-i are located off of the Oregon coast (*Nash et al.*, 2007; *Martini et al.*, 2011, 2013). The McLane profilers travel vertically at $\sim$ 25-33 cm/s, and sample temperature and salinity coincidentally throughout the profile. The McLane profiler data is then interpolated in depth and time to even 2 db vertical intervals and hourly time intervals. Table 2.2 gives the maximum and minimum pressures used in this study from each instrument. For each instrument, the pressure intervals were chosen so that there were no missing data over the duration of the record. Only profilers in water deeper than 1 km were chosen, as high-frequency dynamic height in shallow water is not necessarily a good representation of internal tides and the IGW continuum. The dynamic height is computed at each hourly time step. Record durations range in length from approximately 22-51 days, and are given in Table 2.2.

2.3 Methodology

2.3.1 Frequency spectral density

Frequency spectral densities are computed from time series of SSH at each tide gauge location and corresponding model gridpoint in HYCOM12 and HYCOM25 for model validation against tide gauges. Frequency spectral densities are also computed from the dynamic height computed from McLane profiler data, HYCOM25, and MITgcm48 for comparison to open water in-situ data. Both a linear trend and mean are removed from each time series. Each time series is multiplied by a Tukey window having a taper-to-constant ratio of 0.2, which enforces the periodicity necessary for Fourier transforms of this type. The dynamic height frequency spectral densities are computed for each one year HYCOM25 time series, each three month MITgcm48 time series, and each McLane profiler time series, varying in length, whereas the SSH frequency spectral densities computed from the tide gauges and HYCOM are all computed from one-year long records. A discrete Fourier Transform is used, given by

$$\hat{\eta}_m(\omega_m) = \sum_{n=0}^{N-1} \eta_n e^{\frac{-2\pi imn}{N}}, \tag{2.1}$$

where ω denotes frequency, m and n are indices for the Fourier series and physical series, respectively, and N is the total number of samples. The Fourier Transform is then normalized to give the frequency spectral density

$$Spectral\,density = \frac{2}{N}|\widehat{\eta}(\omega)|^2. \tag{2.2}$$

The variance in four frequency bands (Figure 1.1)—the subtidal [frequencies between 1/366 cpd and 0.86 cpd], the diurnal [frequencies between 0.87 cpd and 1.05 cpd], the semidiurnal [frequencies between 1.86 cpd and 2.05 cpd] and the supertidal [frequencies greater than 2.06 cpd]—are computed by integrating over the unsmoothed peri-

odogram, $|\widehat{\eta}(\omega)|^2$ as

$$\eta^2 = \frac{2}{N^2} \sum_{m=a/2}^{b/2} |\hat{\eta}_m(\omega_m)|^2, \tag{2.3}$$

where a and b are indices such that ω_a and ω_b are the limiting frequencies, defined above. As the time series collected from the McLane profilers are of short duration, the subtidal band was omitted from their comparison, but is used in the tide gauge comparison.

2.3.2 Dynamic height

The comparison of modeled versus observed dynamic height variance is done using methods similar to those used in Section 3.2 of *Savage et al.* (2017a). However, whereas *Savage et al.* (2017a) integrated the model results from the maximum pressure of the profiling instrument to the surface to estimate modeled steric SSH, here we integrate both the models and observations over the pressure intervals covered by the McLane profilers, yielding an improved model-data comparison. Dynamic height, $h(p_1, p_2)$, is computed as an integral of the specific volume, α, using the standard definition (*Knauss*, 1997) given as

$$h(p_1, p_2) = \frac{1}{g} \int_{p_1}^{p_2} \alpha(S, T, p) dp. \tag{2.4}$$

The specific volume, $\alpha(S, T, p)$, is defined as $1/\rho(S, T, p)$ where ρ is density and S, T, and p denote salinity, temperature, and pressure, respectively. The factor of $1/g$ accounts for gravity, and we solve for height, $h(p_1, p_2)$, where p_1 and p_2 are the minimum and maximum pressure levels over which we perform the integration. A trapezoidal integration technique is used in Equation (2.4). Before integration, HYCOM25 temperature and salinity are interpolated onto even 50 db pressure intervals, as the large pressure intervals in the deep ocean in HYCOM output do not provide the vertical

resolution necessary for computation of dynamic height. Dynamic height variance at tidal frequencies is dominated by internal tides, while dynamic height variance at supertidal frequencies is dominated by the IGW continuum. Figure 2.2 displays time-pressure series of density profiles from one of the profilers off the Oregon coast in (a) the McLane profiler, (b) HYCOM25, and (c) MITgcm48. The average number of pressure levels used to compute dynamic height is ~ 630 in the McLane profilers, ~ 26 in HYCOM25, and ~ 36 in MITgcm48. Over the pressure intervals shown in the figure, the model profiles of background density gradient appear similar to the McLane profiles, with MITgcm48 appearing less dense than the McLane profiler or HYCOM25 near the bottom of the water column. The records shown are taken from the first 200 hours of each dataset, and therefore do not span the same time intervals. The McLane profiler data was collected beginning in September, the HYCOM25 data shown is from January, and the MITgcm48 data shown begins in October (Tables 2.2 and 2.1). Time series of dynamic height anomaly about the time mean are shown in (Figure 2.2d) McLane Profiler, (2.2e) HYCOM25, and (2.2f) MITgcm48. The variabilities in the three time series span $\sim 4\,\mathrm{cm}$, but while the HYCOM25 time series of dynamic height (Figure 2.2e) appears to oscillate smoothly with the semidiurnal signal, both the McLane profiler and the MITgcm48 time series appear to have higher frequency signals in addition to the semidiurnal signal.

2.4 Results

2.4.1 Comparison to tide gauges

HYCOM versus tide gauge data frequency spectral density comparisons at three example locations are given in Figure 2.3. The three locations are indicated on Figure 2.1a by filled cyan squares. Figures 2.3a and 2.3c display the comparisons at Eastport, Maine, and Lautoka, Fiji, which were chosen to represent continental and

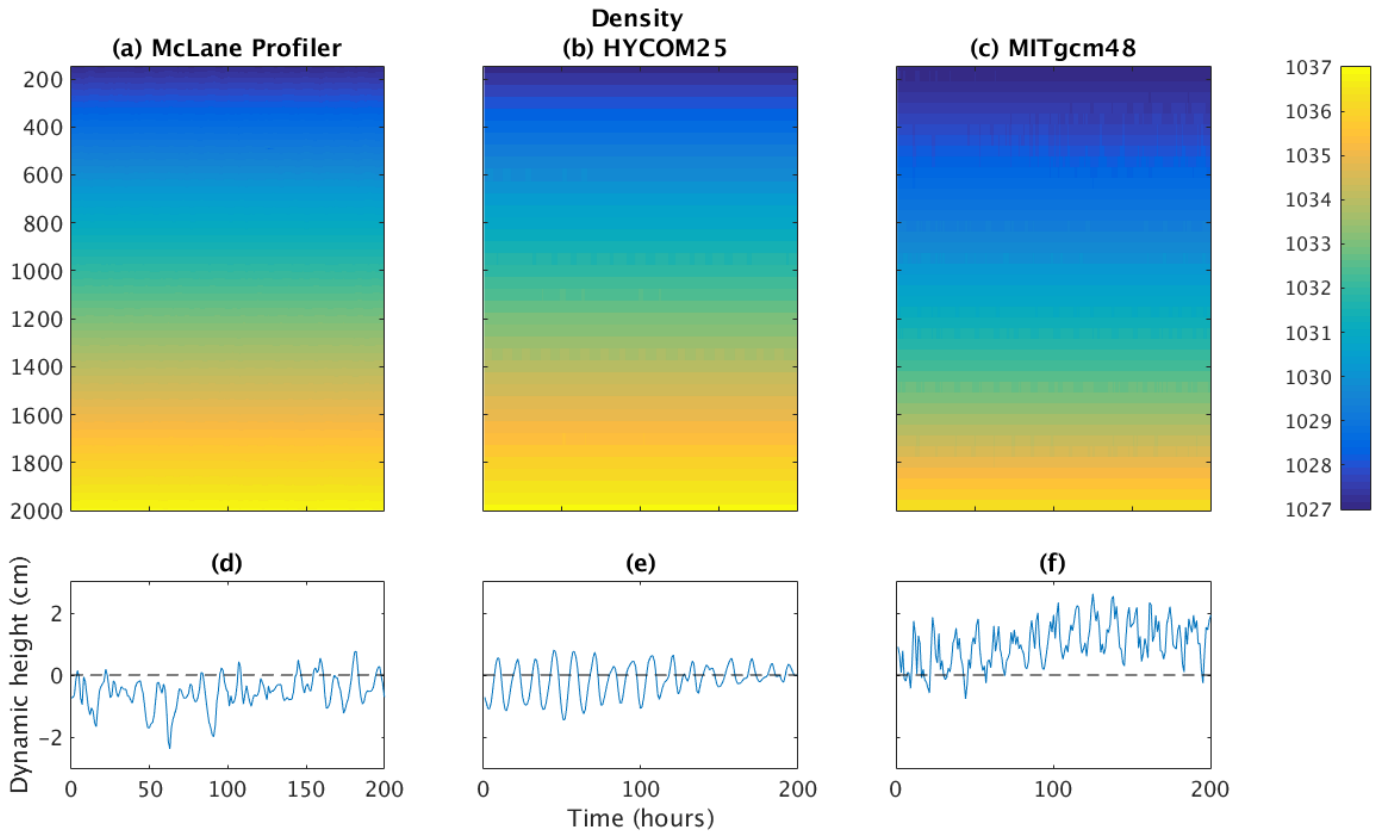

Figure 2.2: Density profile time series (kg/m^3) over the pressure intervals sampled by the McLane profiler located at 233.7°E 43.2°N from (a) a McLane profiler, (b) HYCOM25, and (c) MITgcm48. The bottom row displays time series of dynamic height anomaly (cm) computed as in equation (1) for (d) a McLane profiler, (e) HYCOM25, (f) MITgcm48. Data is shown from the first 200 hours of each dataset, and is therefore shown over different time intervals (September for (a) and (d), January for (b) and (e), and October for (c) and (f)). Reprinted from *Savage et al.* (2017b).

island locations, respectively, where the model performs well. The spectral densities are relatively well matched, although the model is deficient at supertidal frequencies in Figures 2.3a and 2.3b. In both the model output and the tide gauge data, large peaks in SSH variance are seen at the diurnal and semidiurnal bands near one and two cycles per day, showing large tidal signals. Many of the tide gauges display a relatively flat spectrum at supertidal frequencies, which may be indicative of instrument noise or poorly resolved coastal or harbor dynamics. Figure 2.3b, the comparison for Puerto Armuelles, Panama, was chosen to exemplify a location with a greater model/data discrepancy. The model/data differences are particularly large between frequencies ranging from slightly less than diurnal to slightly more than semidiurnal.

We compute the variance in all four frequency bands shown in Figure 1.1 via Equation 2.3. The band-integrated variances in the model are reasonably well matched with the band-integrated tide gauge variances. Figure 2.4 shows scatter plots of the band-integrated SSH variances in the model vs. tide gauge data. In the subtidal band, Figure 2.4a, the model shows scatter, but little to no bias. In the diurnal (Figure 2.4b) and semidiurnal (Figure 2.4c) bands, the model shows less scatter and little bias, except at low-variance values in the semidiurnal plot, where the model is biased high compared to the 1-to-1 (black dashed) line. In the supertidal band, Figure 2.4d, the model shows scatter and a low model bias, in accordance with Figures 2.3a and 2.3b.

Discrepancies between the model and tide-gauge data could be due to a combination of factors, including inadequate model representation of complex coastal bathymetries and instrument noise at supertidal frequencies. The percent error in HYCOM25-to-tide gauge band-integrated variances is calculated as

$$Error = 100 \times \frac{|Tide\,Gauge\,Variance - HYCOM25\,Variance|}{Tide\,Gauge\,Variance} \tag{2.5}$$

and is mapped in Figure 2.5. In the subtidal, diurnal, and semidiurnal maps, (Figures

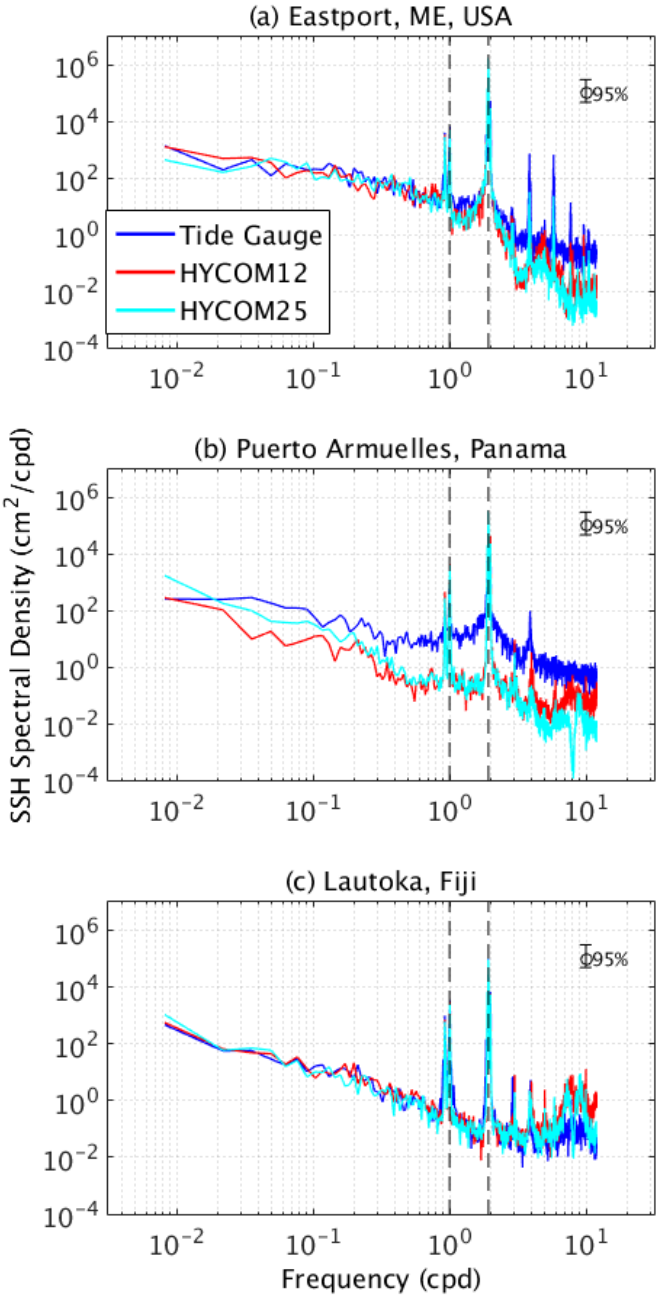

Figure 2.3: Example SSH frequency spectral densities of tide gauge data and corresponding model gridpoint output in (a) Eastport, Maine (b) Puerto Armuelles, Panama and (c) Lautoka, Fiji. Dashed lines denote K_1 diurnal and M_2 semidiurnal tidal frequencies. The 95% confidence interval shown accounts only for random error in spectral density calculations. Reprinted from *Savage et al.* (2017a).

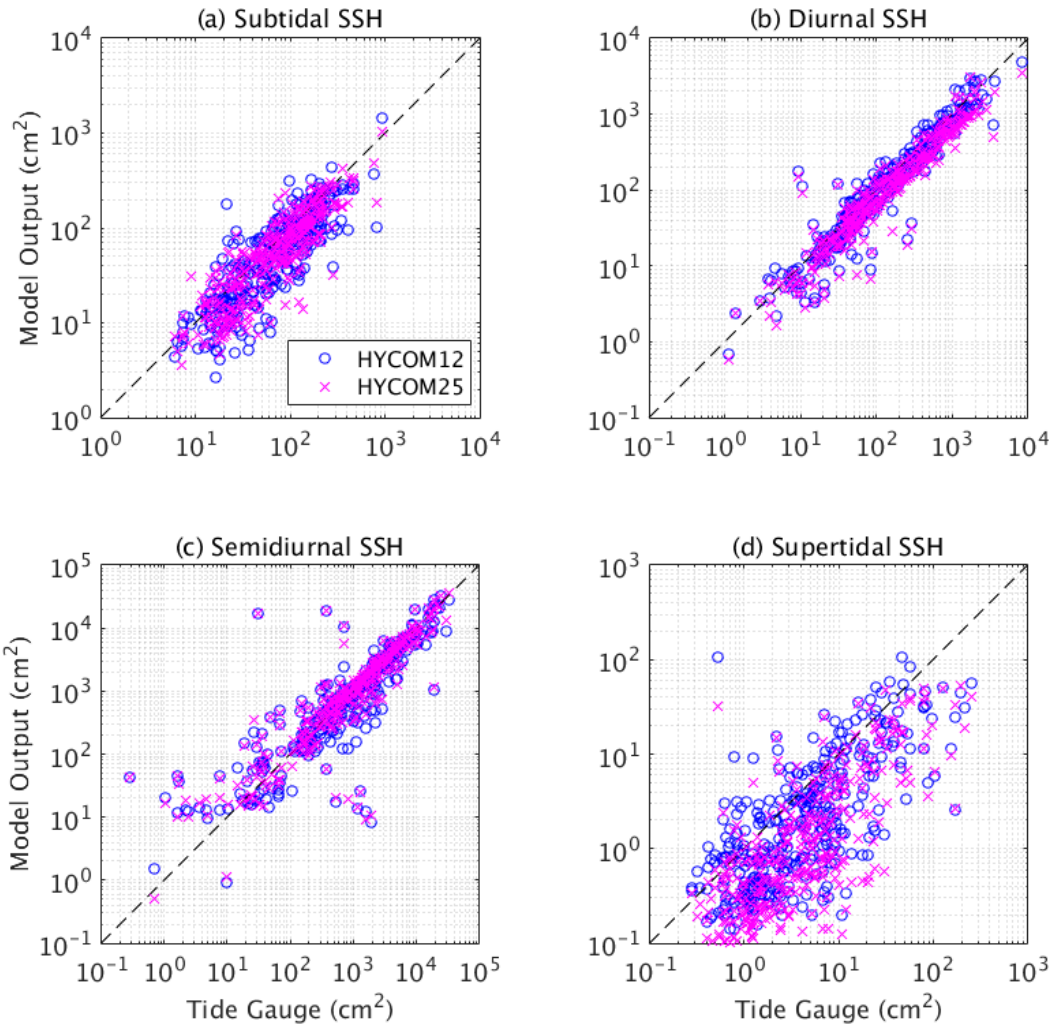

Figure 2.4: Scatter plot of full SSH variance (cm^2) in model output vs. tide gauge data in (a) subtidal, (b) diurnal, (c) semidiurnal, and (d) supertidal frequency bands. Axis limits differ between subplots. Reprinted from *Savage et al.* (2017a).

2.5a, 2.5b, and 2.5c), the error is approximately 10% over much of the globe, with higher error near Japan in the subtidal band and in the Gulf of Mexico in the semidiurnal band. It is unclear why the model is not performing as well in the subtidal band near Japan–a highly energetic region for the subtidal flows–as in other similarly high subtidal variance regions. The supertidal band (Figure 2.5d) in general shows higher error across the globe, approximately 100%, in most locations. Considering Figure 2.5d along with Figure 2.4d, we see that the error in the supertidal map is caused by the model underestimating the supertidal variance at most locations. Again, this is consistent with what is seen in the example frequency spectral densities, Figures 2.3a and 2.3b.

The averages of the band-integrated full SSH variances, computed over the 351 tide gauge locations, from the tide gauge data and both HYCOM simulations, are given in Table 2.3. HYCOM25 is more closely matched to the tide gauge data in total, subtidal, and semidiurnal variance, but underestimates the variance in the diurnal and supertidal frequency bands, where HYCOM12 performs better. These rather substantial drops in variance from HYCOM12 to HYCOM25 ($\sim$ 20% in the diurnal band and $\sim$ 33% in the supertidal band) indicate that the resolution of complex bathymetries is not the primary cause of HYCOM error in these two bands; if it were, then the HYCOM25 simulations should perform better. In the supertidal band, Figure 2.3 show that HYCOM25 is lower than HYCOM12 in all three locations. In this band, coastal variances are in part associated with overtides (*Ray*, 2007), which can be seen clearly in Figures 2.3a and 2.3c as peaks at $\sim$ 3, 4, and 6 cpd. Again, HYCOM25 measures low compared to HYCOM12 in these overtidal peaks, suggesting HYCOM25 may have lower amplitude overtides compared to HYCOM12 globally. This may be related to the fact that the wave drag was not retuned in HYCOM25. *Ansong et al.* (2015) shows that the strength of wave drag tuning substantially affects the barotropic and internal tides in HYCOM. *Egbert et al.* (2004) and *Arbic et al.*

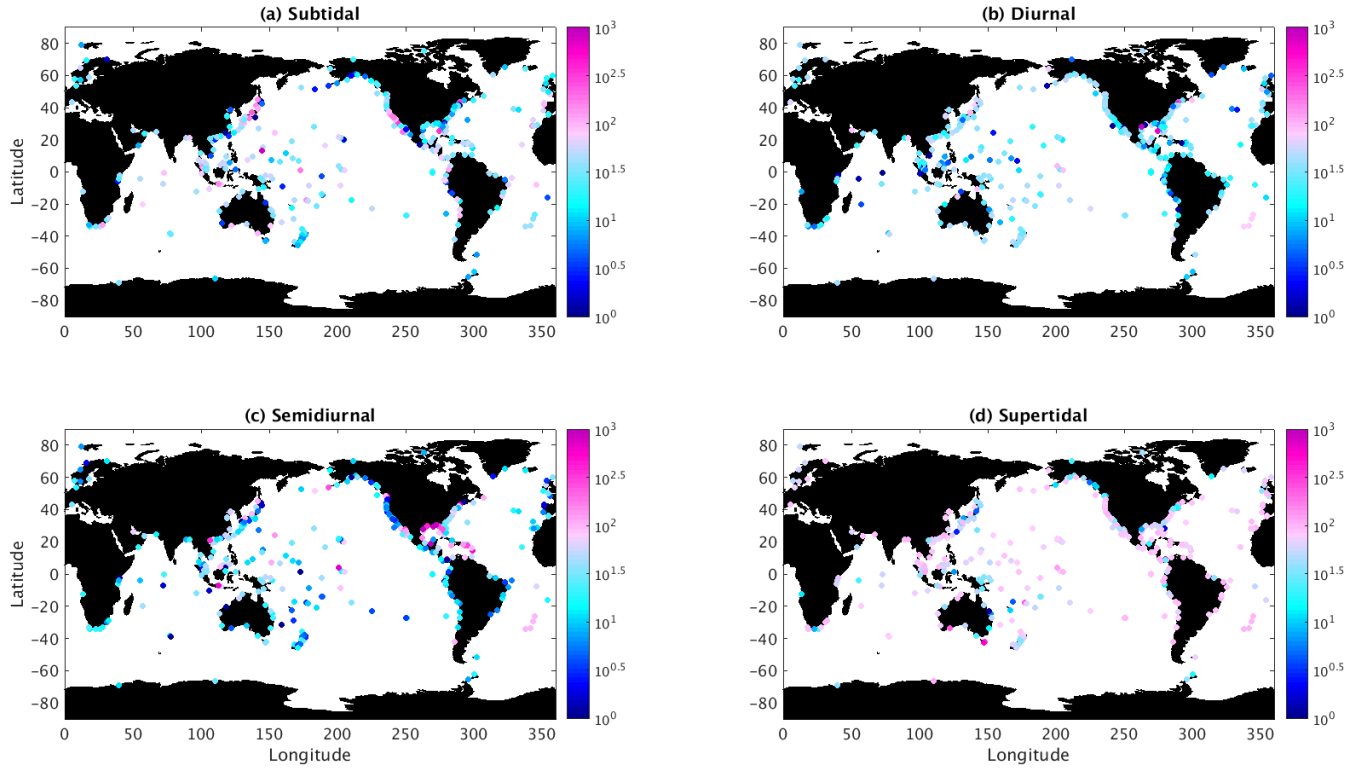

Figure 2.5: Percent error of HYCOM25 variance relative to tide gauge variance (see Equation 2.5) at each tide gauge location in (a) subtidal, (b) diurnal, (c) semidiurnal, and (d) supertidal frequency bands. Reprinted from *Savage et al.* (2017a).

	Tide Gauge	HYCOM12	HYCOM25
Average total variance ($*10^3$)	3.2	2.9 (0.91)	3.0 (0.94)
Average subtidal variance	103.7	82.9 (0.80)	104.4 (1.01)
Average diurnal variance	402.3	336.6 (0.84)	271.1 (0.67)
Average semidiurnal variance ($*10^3$)	2.7	2.5 (0.93)	2.6 (0.96)
Average supertidal variance	13.1	6.3 (0.48)	4.1 (0.31)

Table 2.3: The mean of SSH variance in cm^2 computed over all 351 tide gauge locations for tide gauges and corresponding model gridpoints in HYCOM12 and HYCOM25. The parenthetical values are ratios of HYCOM variance to tide gauge variance. Reprinted from *Savage et al.* (2017a).

(2008) show that even barotropic tides are impacted by the resolution of models, and that the optimal strength of wave drag in models depends on model resolution.

2.4.2 Comparison with McLane profilers

Dynamic height variance frequency spectral density comparisons between HYCOM25, MITgcm48, and the 9 McLane profilers are shown in Figure 2.6. The order of the subplots corresponds to the order of profilers in Table 2.2. At low frequencies, ($\omega \leq 0.2\,\mathrm{cpd}$), both models agree with data in five of the nine locations. Large peaks are seen at semidiurnal frequencies at six of the nine locations, indicative of large semidiurnal internal tides. Additionally, large peaks are seen at diurnal frequencies in Figures 2.6e and 2.6f, representing the Luzon Strait where diurnal internal tides are known to be large (*Jan et al.*, 2008). Diurnal peaks are also clear in Figures 2.6h and 2.6i, off the Oregon coast, where the strength of diurnal tides is known to be highly variable (*Erofeeva et al.*, 2003). In the Hawai'i cluster (Figures 2.6a-2.6d) as well as Figure 2.6g (Oregon coast), both models are deficient compared to data at frequencies ranging from $\sim 0.2\,\mathrm{cpd} - 1\,\mathrm{cpd}$, for reasons that are not clear but may have to do with the inability of the models to represent fast submesoscale motions. In most locations, MITgcm48 matches the observations better than HYCOM25 does in supertidal frequencies ($\omega > 2.06\,\mathrm{cpd}$), consistent with *Savage et al.* (2017a), that showed that

HYCOM25 SSH is deficient compared to observations at supertidal frequencies.

This low bias of HYCOM25 at supertidal frequencies is confirmed in Table 2.4, that lists the standard deviation (computed as the square root of the band-integrated variance [Equation 3]) at all nine locations. The model performances are similar in the diurnal and semidiurnal tidal ranges. However, in the supertidal band, MITgcm48 is substantially closer to the McLane observations than HYCOM25 is, in five of the nine locations. Figure 2.7 shows the band-integrated variance (the squares of standard deviations listed in Table 2.4) in the form of scatter plots. In diurnal and semidiurnal bands (Figures 2.7a and 2.7b), variance estimates from HYCOM25 and MITgcm48 agree with observations with respect to the 1-to-1 (black dashed) lines. Additionally, the variance estimates from both models are near equal at all locations. In Figure 2.7c, the supertidal band, HYCOM25 is biased low compared to the 1-to-1 line, particularly at locations g-i, the profilers located off the Oregon coast. This deficiency in HYCOM25 may be due to the lower horizontal and vertical resolution of HYCOM25 relative to MITgcm48. It has been shown that model horizontal resolution affects the strength of the IGW continuum (*Müller et al.*, 2015; *Savage et al.*, 2017a). Another possible source of discrepancy between the model estimates of supertidal variance is the lack of wave drag parametrization in MITgcm, that would tend to yield strong high-frequency motions in MITgcm relative to HYCOM. As there are only nine McLane profilers that provide the high vertical resolution and high-frequency data necessary for calculation of dynamic height, this model/observation comparison offers limited insight into which model, if either, is accurately representing oceanic high-frequency dynamics. While MITgcm certainly appears to be outperforming HYCOM in these nine locations, we cannot say that this is representative of model performance on a global scale.

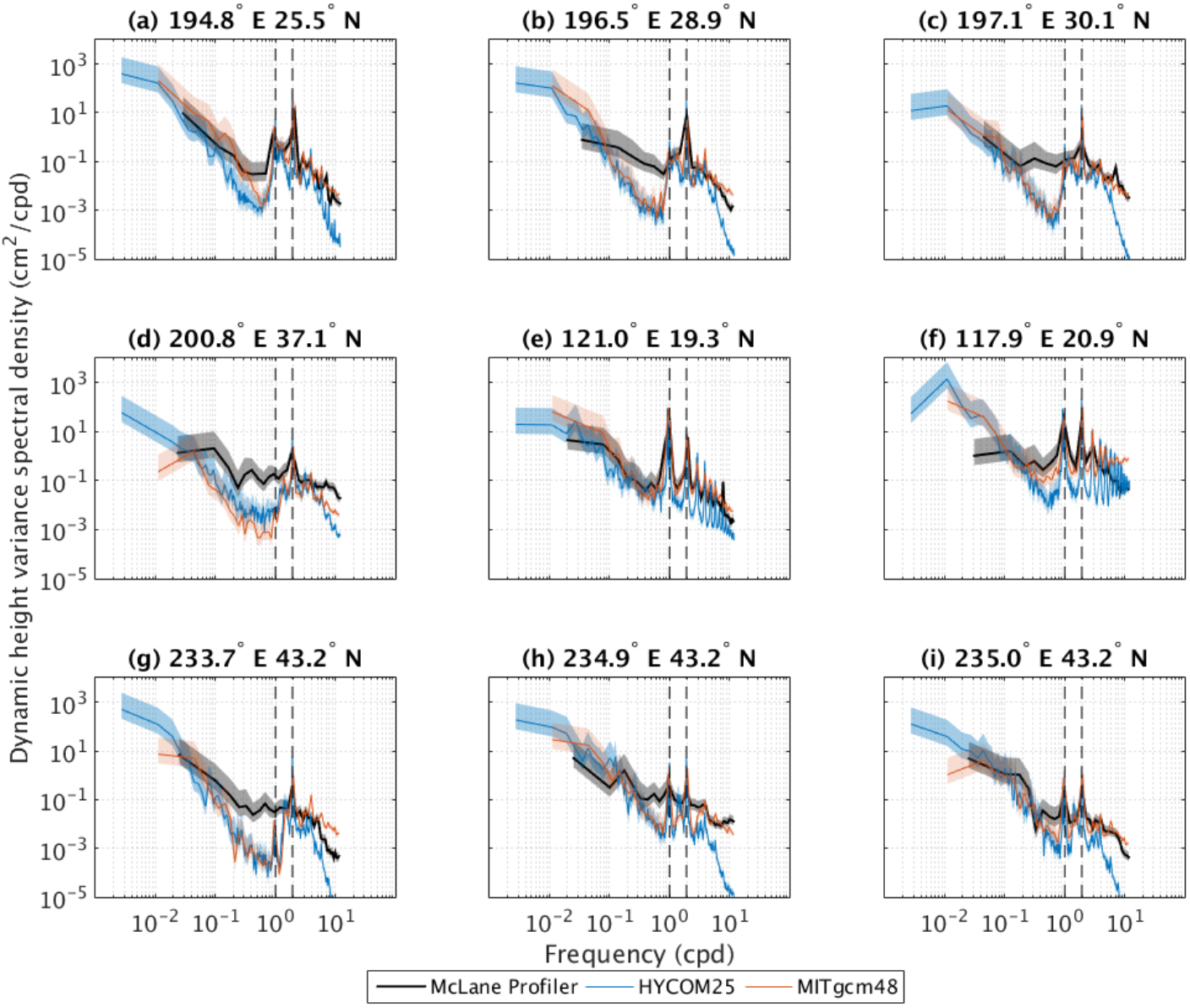

Figure 2.6: Dynamic height variance frequency spectral densities from McLane profilers and nearest neighbor HYCOM25 and MITgcm48 gridpoints. The dashed vertical lines denote K_1 diurnal and M_2 semidiurnal tidal frequencies. The shaded regions are the 95% confidence intervals, that account only for random error in spectral density calculations. Reprinted from *Savage et al.* (2017b).

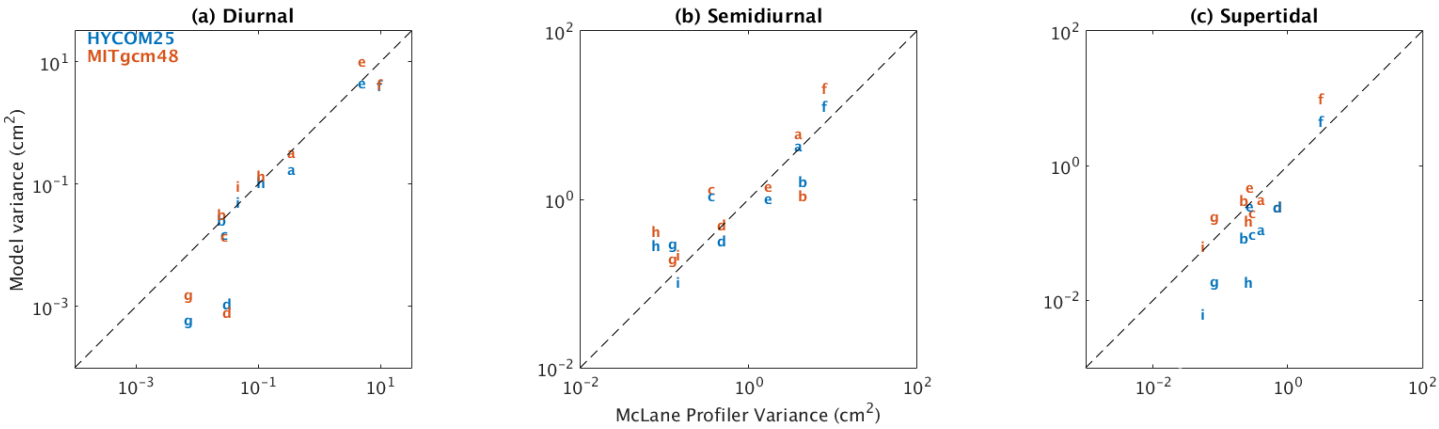

Figure 2.7: Scatter plots of band-integrated dynamic height variance vs. McLane profilers in 1/25° HYCOM and 1/48° MITgcm in (a) diurnal, (b) semidiurnal, and (c) supertidal frequency bands. Letters on scatter plots correspond to profiler locations listed in Table 2.2. Reprinted from *Savage et al.* (2017b).

Profiler	a	b	c	d	e	f	g	h	i
Diurnal									
McLane Profiler	0.541	0.144	0.154	0.160	2.039	2.930	0.078	0.302	0.207
HYCOM25	0.415	0.160	0.123	0.033	2.144	2.008	0.025	0.323	0.226
MITgcm48	0.576	0.178	0.119	0.029	3.178	2.048	0.040	0.366	0.305
Semidiurnal									
McLane Profiler	1.869	1.969	0.573	0.654	1.239	2.713	0.333	0.263	0.367
HYCOM25	2.075	1.277	1.049	0.565	1.013	3.577	0.545	0.533	0.324
MITgcm48	2.461	1.047	1.153	0.707	1.194	4.534	0.445	0.644	0.467
Supertidal									
McLane Profiler	0.587	0.433	0.512	0.782	0.486	1.687	0.265	0.471	0.226
HYCOM25	0.335	0.292	0.310	0.493	0.504	2.147	0.139	0.136	0.079
MITgcm48	0.559	0.555	0.446	0.497	0.693	3.142	0.424	0.390	0.252

Table 2.4: Standard deviation of dynamic height variance (cm) at each profiler location for McLane profiler, HYCOM25, and MITgcm48 in diurnal, semidiurnal, and supertidal frequency bands. Reprinted from *Savage et al.* (2017b).

2.5 Summary

In comparing both HYCOM and MITgcm to in-situ data, we find that both models are relatively well matched to the available data. Full SSH frequency spectral densities computed from HYCOM are well matched compared to SSH frequency spectral densities computed from tide gauges. We find that HYCOM is well matched to data in subtidal, diurnal, and semidiurnal frequencies, but is deficient compared to data in the supertidal band. We also find that there is no geographical dependence on the error (Equation 2.5); HYCOM does not appear to be performing better in either deep or coastal waters.

The comparison of dynamic height spectral densities computed from HYCOM25 and MITgcm48 to those computed from McLane profiler data shows that, once again, HYCOM25 is well matched to data in the tidal (diurnal and semidiurnal bands), but deficient in the supertidal band. MITgcm48 appears to be well matched to data in all frequency bands. This low bias in HYCOM may be due to the lower horizontal and vertical resolution of the HYCOM simulation, to the differences in vertical discretization and/or subgridscale closures, or to the effects of wave drag parametrization in HYCOM. As the observational data needed to study high-frequency and small scale IGWs is very limited, models may be useful in creating global estimates of energy contained in IGWs. Here, we have shown that two global high-resolution general circulation ocean models–HYCOM and MITgcm–may be useful for such studies.

CHAPTER III

Frequency-wavenumber spectral density of sea surface height

3.1 Introduction

As discussed in Chapter I, high-resolution ocean models, like those studied in Chapter II, are beginning to resolve a partial internal gravity wave (IGW) continuum (*Müller et al.*, 2015). Here, we build upon results in *Müller et al.* (2015) by examining SSH spectral density in seven regions in the HYbrid Coordinate Ocean Model (HYCOM) and the MIT general circulation model (MITgcm), simulations forced by both atmospheric fields and tides. We aim to quantify some of the differences in the dynamics of these models, particularly at high-frequency and -wavenumber, where global ocean models are only beginning to perform. In addition, we aim to provide estimates of the contributions of different frequency bands to the small-scale dynamics of interest for the Surface Water and Ocean Topography (SWOT; *Fu et al.*, 2012) mission.

To identify the differences between the two models, we use hourly HYCOM and MITgcm output from two HYCOM simulations and three MITgcm simulations of varying horizontal resolution to compute frequency-horizontal wavenumber spectral density in seven regions. The seven regions were chosen to exemplify areas dominated

by different ocean dynamics, e.g. internal tides versus mesoscale eddies. As in *Müller et al.* (2015), we show that large peaks exist along the linear dispersion curves for the first three vertical modes, indicating partial resolution of the IGW continuum. We also examine the impact of horizontal resolution on the ability of models to simulate the IGW continuum (*Müller et al.*, 2015).

To study the contributions of different frequency bands to wavenumber spectral density, we integrate the frequency-horizontal wavenumber spectral densities over three frequency bands of interest: subtidal, tidal, and supertidal (as in Figure 1.1, except the tidal band includes both the diurnal and semidiurnal bands and the frequencies between them). We examine whether high-frequency motions dominate at high-wavenumbers, as has been done in earlier studies (*Richman et al.*, 2012; *Callies and Ferrari*, 2013; *Rocha et al.*, 2016a), and whether the dominance of high-frequency motions increases with increased horizontal resolution of the models.

3.2 Methodology

3.2.1 Frequency-horizontal wavenumber spectral density

Frequency-horizontal wavenumber spectral densities of SSH are computed from the HYCOM and MITgcm simulations over seven regions. The locations and bathymetries of the seven regions are displayed in Figure 3.1a and the HYCOM25 subtidal SSH variance in each region is shown in Figure 3.1b. The longitudinal and latitudinal ranges of each region are listed in Table 3.1, along with abbreviations for each region used in several figures. Three-month blocks of hourly data were used from all five simulations. The three-month time period is dictated by the amount of data available from the highest resolution model, MITgcm48, at the time of output collection. The first three months of the records listed in Table 2.1 for HYCOM12 and HYCOM25 were used to computed frequency-horizontal wavenumber spectral densities. Before

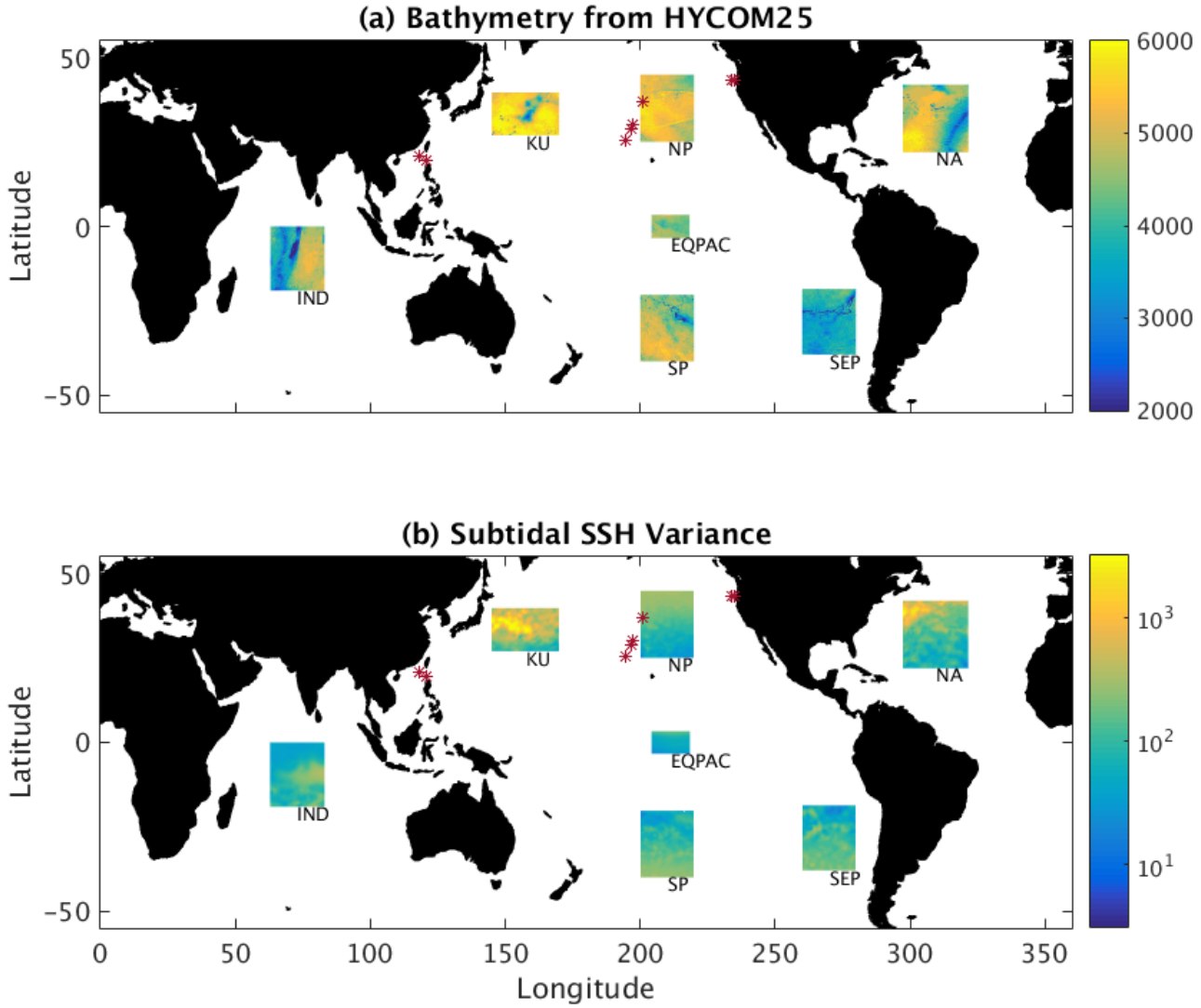

Figure 3.1: (a) HYCOM25 bathymetries (m) from seven regions used to compute frequency-horizontal wavenumber spectral densities overlaid on map of regions. Bathymetries from MITgcm48 are comparable. Abbreviations for the regions are listed in Table 3.1. Locations of nine McLane profilers are overlaid on map as red stars. (b) Low frequency SSH variance (cm^2) from HYCOM25 computed as in *Savage et al.* (2017a) in seven regions used in study. Reprinted from *Savage et al.* (2017b).

the spectral densities are computed, the temporal and two-dimensional spatial trends and means are removed and a Tukey window having a taper-to-constant ratio of 0.2 is employed in time and along both spatial dimensions. Frequency-horizontal wavenumber spectral density is computed via a discrete three-dimensional Fourier Transform, given as

$$\hat{\eta}_{p,h,m}(k_p, l_h, \omega_m) = \sum_{q=0}^{Q-1} \sum_{g=0}^{G-1} \sum_{n=0}^{N-1} \eta_{q,g,n} e^{-2\pi i(\frac{pq}{Q} + \frac{hg}{G} + \frac{mn}{N})}, \tag{3.1}$$

where η denotes sea surface height, ω denotes frequency, k denotes zonal wavenumber, and l denotes meridional wavenumber. Indices p, h, and m are for the Fourier series, and q, g, and n are indices for the physical series. The total number of samples in the zonal, meridional, and temporal directions are denoted as Q, G, and N, respectively.

The three-dimensional Fourier transform in (3.1) is used to compute a two-dimensional spectral density, $|\hat{\eta}(K, \omega)|^2$, along isotropic (radial) wavenumber, K (*Lumley*, 1970). The isotropic wavenumber vector, K, is defined here as an evenly distributed discrete set of wavenumbers whose length is arbitrarily chosen to equal the artithmetic mean of the lengths of k and l. The minimum and maximum values of the vector K are the minimum and maximum values of $\sqrt{k^2 + l^2}$, respectively. The spectral density contribution to the r^{th} element of isotropic wavenumber, K_r, can be computed as

$$|\hat{\eta}_r(K_r, \omega)|^2 = \begin{cases} \frac{2}{QGN} \Big[\sum_{p=1}^{\chi} \sum_{h=1}^{\zeta} |\hat{\eta}_{p,h}(k_p, l_h, \omega)|^2 \Big], & \text{if } r = 1 \\ \frac{2}{QGN} \Big[\sum_{p=1}^{\chi} \sum_{h=1}^{\zeta} |\hat{\eta}_{p,h}(k_p, l_h, \omega)|^2 \Big] - \sum_{\gamma=1}^{r-1} |\hat{\eta}_{\gamma}(K_{\gamma}, \omega)|^2, & \text{if } r > 1 \end{cases} \tag{3.2}$$

where $k_\chi^2 + l_\zeta^2 < K_r^2$, and r is an index which spans 1 to the length of K. This definition of $|\hat{\eta}(K, \omega)|^2$ is computed iteratively. The first term on the right hand side of Equation (3.2) is a sum over all values of $|\hat{\eta}(k, l, \omega)|^2$ for which k and l satisfy the condition $k_\chi^2 + l_\zeta^2 < K_r^2$, and the second term on the right hand side in the condition

that $r > 1$ is a sum over all previously computed values of $|\hat{\eta}(K, \omega)|^2$. This method conserves variance when transforming from anisotropic to isotropic spectral density.

3.2.2 The dispersion relation for internal gravity waves

The dispersion relation for internal gravity waves describes the relationship between frequencies and wavenumbers for IGWs. In this study, the dispersion relation is used to identify variance attributed to the IGW continuum. The following derivation of the dispersion relation, and the following related description of the vertical modal structure, is adopted from *Kundu* (1990). We begin with the linearized momentum equations for zonal and meridional flow, and the equation for conservation of mass, in an unstratified (barotropic) flow :

$$\frac{\partial u}{\partial t} - fv = -g\frac{\partial \eta}{\partial x} \tag{3.3}$$

$$\frac{\partial v}{\partial t} + fu = -g\frac{\partial \eta}{\partial y} \tag{3.4}$$

$$\frac{\partial \eta}{\partial t} + H\Big[\frac{\partial u}{\partial x} + \frac{\partial v}{\partial y}\Big] = 0 \tag{3.5}$$

Here, $(u,\ v)$ are the velocities in $(x,\ y)$ respectively, g is the acceleration due to gravity, f is the Coriolis parameter, H is water column height, and η is a perturbation sea surface height under the condition $H >> \eta$. We assume that u, v, and η are of the typical waveform $u(x, y, t) = Ue^{i(kx+ly-\omega t)}$, and H and f are assumed constant. We can rewrite the above equations as:

$$-i\omega u - fv = -igk\eta \tag{3.6}$$

$$-i\omega v + fu = -igl\eta \tag{3.7}$$

$$-i\omega\eta + ikHu + ilHv = 0. \tag{3.8}$$

This system of equations can be rewritten as the product of two matrices as

$$\begin{pmatrix} -i\omega & -f & igk \\ f & -i\omega & igl \\ ikH & ilH & -i\omega \end{pmatrix} \begin{pmatrix} u \\ v \\ \eta \end{pmatrix} = \begin{pmatrix} 0 \\ 0 \\ 0 \end{pmatrix}. \tag{3.9}$$

We can solve this system of equations by computing the determinant of the first matrix, which must be equal to zero for non-trivial solutions. We have then derived the relation

$$\omega^2 = f^2 + gH(k^2 + l^2) \tag{3.10}$$

or, in terms of the isotropic wavenumber, K,

$$\omega^2 = f^2 + gHK^2. \tag{3.11}$$

This relationship is known as the dispersion relation and describes the relationship between the propagation of gravity waves in time (ω) and space (K‘). Using dimensional analysis, we can prove that a shallow water gravity wave in a homogeneous layer propagates with a phase speed $c = \sqrt{gH}$. In a stratified fluid, each vertical mode, denoted by a subscript n, is associated with a with phase speed c_n. We can rewrite the dispersion relation, solving for c_n, as

$$c_n^2 = \frac{\omega^2 - f^2}{K_n^2}. \tag{3.12}$$

To understand the vertical mode structure of a stratified fluid, it can be convenient to write a variable, such as zonal velocity u, as a summation over the vertical modes as

$$u(x, y, z, t) = \sum_{n=0}^{\infty} U_n(x, y, t) F_n(z). \tag{3.13}$$

We can now solve for the vertical structure, $F(z)$, by solving the Sturm-Liouville

equation for vertical modes

$$\frac{d}{dz}\Big(\frac{\omega^2 - f^2}{N^2 - \omega^2}\frac{dF}{dz}\Big) + \frac{1}{\lambda^2}F(z) = 0 \tag{3.14}$$

with boundary conditions

$$\frac{dF}{dz} = 0,\ z = 0, -H \tag{3.15}$$

where λ are the eigenvalues, N^2 is the Brunt-Väisälä frequency, defined as $N^2 = -\frac{g}{\bar{\rho}}\frac{d\rho_o}{dz}$, $\rho_o(z)$ is a background density function, and $\bar{\rho}$ is a constant density. We solve for the eigenvalues and orthogonal eigenfunctions of this equation using the shooting method. This method estimates the eigenvalues, checks whether the Sturm-Liouville equations satisfy the boundary conditions, and adjusts the estimate based on the error. The number of eigenvalues is dependent on the number of vertical modes of interest. To create an accurate representation of the vertical structure of velocity, up to 20 vertical modes can be necessary. However, for the display of SSH frequency-horizontal wavenumber spectra that is focused on here, only the first three vertical modes are needed. Each vertical mode has a distinct horizontal scale, and the eigenvalues can be defined as $\lambda_n^2 = 1/K_n^2$. We then solve for each of the three constant eigenspeeds (*Munk*, 1981) by setting ω equal to the M_2 frequency in Equation 3.12. The eigenspeeds then describe the relationship between all values of ω and K computed as in Section 3.2.1. As in *Müller et al.* (2015), we use the extreme eigenspeed values, computed for local values of f, N^2, and H for each grid point on the northern and southern boundaries of a region, in order to ascertain bounding dispersion curves. Although both models are hydrostatic, the Sturm-Liouville equation that we solve uses a non-hydrostatic vertical momentum equation. The differences that may arise from this discrepancy would most prominently affect frequencies near the buoyancy frequency, and would not greatly affect the frequencies of interest in this study. Because the eigenspeeds are greatly dependent on water column depth, H, the

Region	Abbreviation	Longitude range	Latitude range	Average transition length scale
North Pacific	NP	200.0° E–220.0° E	25.0° N–45.0° N	80.0 km
South East Pacific	SEP	260.0° E–279.9° E	18.6° S–37.9° S	58.3 km
Kuroshio	KU	145.0° E–169.9° E	27.0° N–39.7° N	22.7 km
Equatorial Pacific	EQPAC	204.2° E–218.3° E	3.4° S–3.4° N	124.2 km
South Pacific	SP	200.0° E–220.0° E	20.3° S–40.0° S	53.6 km
North Atlantic	NA	297.4° E–321.66° E	22.0° N–41.8° N	37.8 km
Indian Ocean	IND	63.0° E–83.0° E	0°-19.0° S	120.0 km

Table 3.1: Longitudinal and latitudinal ranges of the seven boxes used for calculation of frequency-horizontal wavenumber spectral densities. The second column lists the abbreviation for each region used in Figures 3.1 and 3.7. The final column lists the average transition length scale across all five simulations and is discussed in Section 4.3. Reprinted from *Savage et al.* (2017b).

extreme eigenspeeds were chosen from grid points with $H > 1\,\text{km}$. The assumption of a relatively constant bottom depth H is only really valid in the North Pacific region (Figure 3.1a). While it is difficult to find large regions in the ocean that have nearly constant bottom depth, we note that grid points with depths shallower than 500 m comprise less than 0.5% of the grid points in each of the seven regions used for this study. The validity of frequency-horizontal wavenumber spectral densities also hinges on horizontal homogeneity of the fields. Figure 3.1b shows the HYCOM25 subtidal SSH variance (computed as in *Savage et al.* (2017a)) in the boxes used in this study. While the majority of our boxes are horizontally homogeneous, the Kuroshio and especially the North Atlantic regions have areas of large subtidal variance that changes rapidly in space. However, we find that this horizontal inhomogeneity does not significantly affect the IGW modes of main interest in this study. We also note that the desire for large horizontal regions with relatively constant bottom depth prohibits our ability to calculate frequency-horizontal wavenumber spectral density in regions colocated with our in-situ data in the Luzon Strait and off of the Oregon coast.

3.3 Results

3.3.1 Frequency-horizontal wavenumber spectral density of SSH

Sea surface height variance frequency-horizontal wavenumber spectral densities, computed from MITgcm48 over all seven regions shown in Figure 3.1, are displayed in Figure 3.2. Similar collections of frequency-horizontal wavenumber spectral densities computed from HYCOM12, HYCOM25, MITgcm12, and MITgcm24 in all seven regions are given in the supplementary material. To allow for easier comparison across simulations, the wavenumber axis in all subplots of Figure 3.2, and in the corresponding supplementary figures, is set to the maximum horizontal wavenumber computed for HYCOM25. All of the subplots in Figure 3.2 show the linear dispersion curves for the first three IGW vertical modes, depicted as white curves. The dispersion curves are computed from the Sturm-Liouville problem at all the model gridpoints (in water deeper than 1 km) along the northern and southern boundaries of the regions. As in *Müller et al.* (2015), maxima and minima of the eigenspeeds are used to draw bounding dispersion curves for each mode in each region. The IGW dispersion relation curves vary greatly between regions. In each region, the areas within the bounding dispersion curves stand out as having larger variance compared to the background, and appear most prominently in the North Pacific (Figure 3.2a), the Equatorial Pacific (Figure 3.2d) and the Indian Ocean (Figure 3.2g), all regions known to have a large IGW SSH signature (*Savage et al.*, 2017a). The Kuroshio (Figure 3.2c) and the North Atlantic (Figure 3.2f) display large variance at low-frequency and low-wavenumber, indicative of regions with strong mesoscale activity. The high variance lying along the dispersion curves in these strongly eddying regions appear more blurred in the wavenumber direction than in some weakly eddying regions, such as the North Pacific, suggesting that the low frequency modulation of IGWs by mesoscale eddies in these regions affects the dynamics of the IGW SSH signatures. The semidiurnal internal

tides are prominent (appearing as spots of large variance within the dispersion curves at 2 cpd) in the spectral densities of all regions. These semidiurnal internal tides have larger variance than the background semidiurnal tidal variance (horizontal stripes at 2 cpd) in the Kuroshio (Figure 3.2c), the Equatorial Pacific (Figure 3.2d), the North Atlantic (Figure 3.2f), and the Indian Ocean (Figure 3.2g). The dispersion curves for the other simulations, shown in the supplementary material, are qualitatively similar to the MITgcm48 plots shown in Figure 3.2.

SSH variance frequency-horizontal wavenumber spectral densities in the North Pacific region from all five simulations are shown in Figure 3.3. Increasing horizontal resolution yields a more energetic IGW continuum (*Müller et al.*, 2015). For instance, the HYCOM25 spectral densities are noticeably more spread out along the dispersion curves than the HYCOM12 spectral densities (Figure 3.3). Similarly, the MITgcm48 spectral densities are more spread out along the dispersion curves than the MITgcm24 spectral densities, that in turn are more filled out than the MITgcm12 spectral densities. There are large peaks at higher tidal harmonics; however they appear to be less prominent in HYCOM25 than in HYCOM12. Similarly, it appears that the higher harmonics become less prominent as resolution increases in the MITgcm simulations. We speculate that the prominent higher harmonics arise from a combination of several aspects of our analysis. These large variance horizontal stripes may be artifacts of the lack of resolution of internal wave triads in lower resolution simulations. The higher harmonics become less prominent as resolution increases and models are better able to represent more wave triads, thus filling out the spectrum more completely (*Müller et al.*, 2015).

We also conjecture that these stripes are, to some extent, artifacts of the Tukey window used to enforce periodicity prior to the calculation of the discrete Fourier Transform (Equation 4). Tukey windows, like other rectangular windows, are known to have problems with spectral leakage (*Harris*, 1976). We choose to use a Tukey

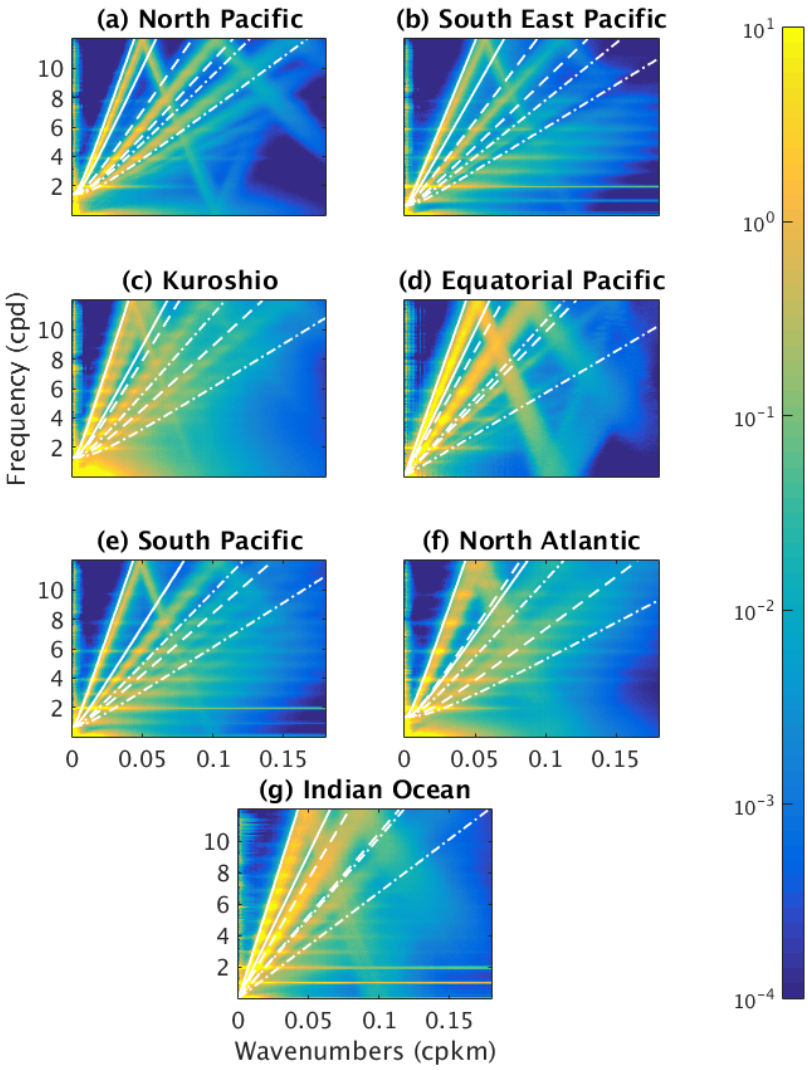

Figure 3.2: Sea surface height variance frequency-horizontal wavenumber spectral density [$\mathrm{cm}^2/(\mathrm{cpd}\,\mathrm{cpkm})$] computed over seven regions from MITgcm48. Wavenumber axes are set to the maximum wavenumber for each region computed in HYCOM25. White curves show theoretical IGW linear dispersion relations for first (solid), second (dashed), and third (dashed-dotted) vertical modes. Bounding curves for each vertical mode are computed from the maximal and minimal eigenspeeds along the northern and southern boundaries, as in *Müller et al.* (2015). Reprinted from *Savage et al.* (2017b).

window because using a windowing function that minimizes the spectral leakage also removes more of the variability of interest. HYCOM12 and MITgcm12 show similar dynamics, with slightly larger variance along the first mode in MITgcm12. Similarly, MITgcm24 has more variance along the first mode than HYCOM25. In the HYCOM25, MITgcm24, and MITgcm48 spectral densities, the high variance along the dispersion curves folds back after reaching the Nyquist frequency of 12 cpd. This indicates that the hourly sampling is insufficient because, in some regions, there is significant variance in high-frequency motions that are not resolved with one hour sampling. Additionally, the aliasing seems to be strong in the North Pacific (Figure 3.2a), the Equatorial Pacific (Figure 3.2d), and the Indian Ocean (Figure 3.2g), where the IGW signal is known to be large.

3.3.2 Frequency band contributions to wavenumber spectral density

To quantify the contributions from different frequency bands to the wavenumber spectral density, the frequency-horizontal wavenumber spectral densities (Equation 3.2) are integrated over three frequency bands: the subtidal band [$\omega < 0.86$ cpd], the tidal band [$0.87 < \omega < 2.05$ cpd], and the supertidal band [$\omega > 2.06$ cpd]. Due to known impacts of dissipation schemes on the effective resolution of ocean models (*Soufflet et al.*, 2016), a caveat of this study is that we are unable to examine the high-wavenumbers affected by the spectral roll off associated with eddy viscosity. This roll off can be clearly seen at the high-wavenumber [$\sim (3\delta x)^{-1}$] end of the wavenumber spectral densities discussed in this section (Figures 3.4 and 3.5). For these reasons, we limit our study to wavenumbers $< (3\delta x)^{-1}$. The MITgcm48 wavenumber spectral densities for all seven regions shown in Figure 3.1 from the three frequency bands of interest are given in Figure 3.4. The ratio of supertidal variance to total variance is plotted as a purple dashed-dotted line and references the right axes in Figures 3.4 and 3.5. Supplementary Figures 5-8 show the wavenumber spectral density contributions

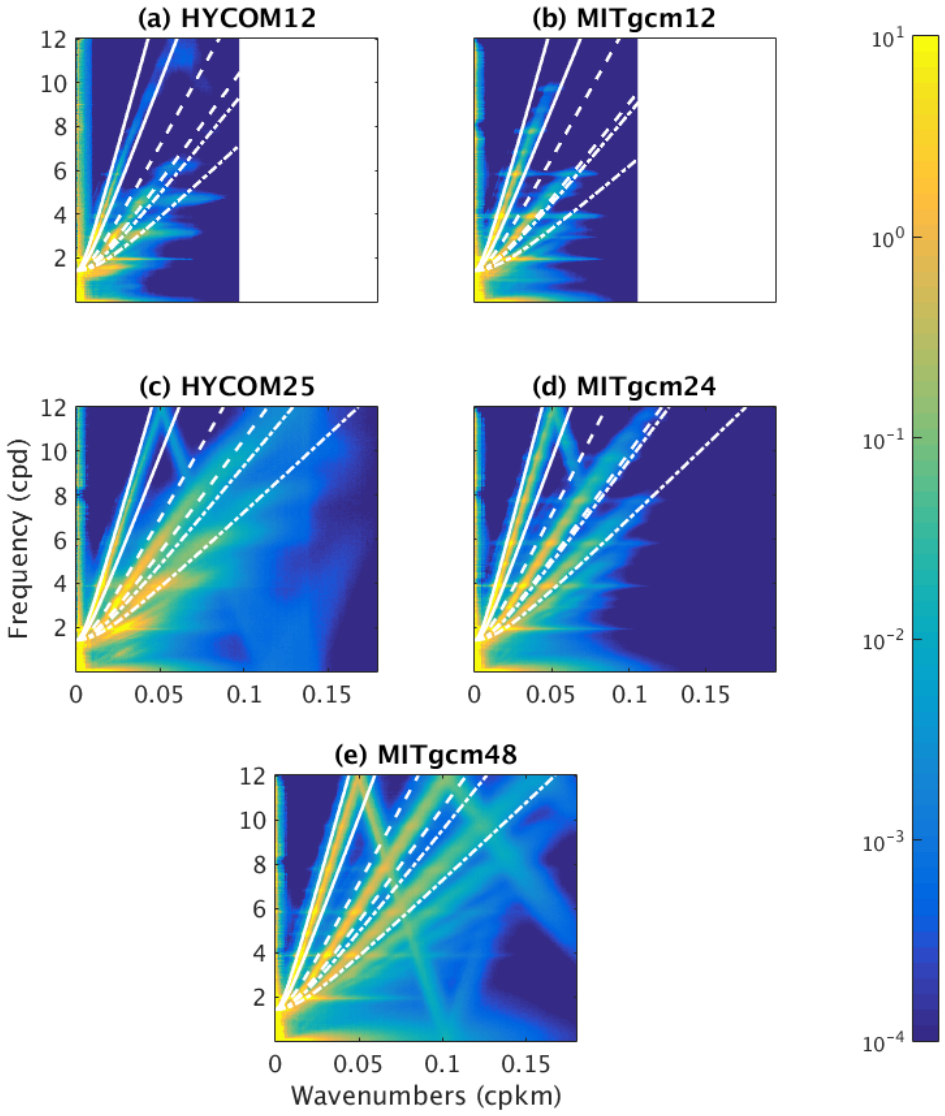

Figure 3.3: Sea surface height variance frequency-horizontal wavenumber spectral density of [$\mathrm{cm}^2/(\mathrm{cpd\,cpkm})$] computed in North Pacific region in all five simulations. Wavenumber axes are the same in each plot, and are set to the maximum wavenumber for the HYCOM25 calculation. White curves show theoretical IGW linear dispersion relations for first (solid), second (dashed), and third (dashed-dotted) vertical modes. Bounding curves for each vertical mode are computed from the maximal and minimal eigenspeeds along the northern and southern boundaries, as in *Müller et al.* (2015). Reprinted from *Savage et al.* (2017b).

in the other four simulations. In all regions, supertidal phenomena contribute very little at low wavenumbers, but are substantial at scales of approximately 100 km and smaller. At scales smaller than ~ 50 km, either the tidal or supertidal frequency bands dominate in every region. In all regions, the ratio of supertidal variance to total variance shows a sharp increase at ~ 250 km where it is a minimum, and increases continuously until it reaches nearly 1 at scales varying by location. The ratio of supertidal to total variance drops off at the highest wavenumbers in the South East Pacific, South Pacific, and Indian Ocean (Figures 3.4b, 3.4e, and 3.4g) and may be related to high wavenumber roll off described above. The two humps prominent in the Equatorial Pacific (Figure 3.4d) in the tidal and subtidal bands appear to occur at the wavenumbers affected by the aliasing in Figure 3.2d. This suggests that the energy in these two humps should actually be attributed to the supertidal frequency band, if the temporal sampling allowed for resolution of higher frequency IGWs. Less prominent humps can be seen in the North Pacific, South Pacific, and Indian Ocean regions, suggesting that this contamination is prevalent in regions of high IGW activity.

The wavenumber spectral densities of subtidal, tidal, and supertidal frequency bands for all five simulations in the Kuroshio region are shown in Figure 3.5. While the contributions from the three frequency bands of interest at low-wavenumber (scales ~ 100 km to $1,000$ km) are not strongly sensitive to model horizontal resolution, below these scales, the behavior of the supertidal band changes as horizontal resolution changes. Across all simulations, the subtidal and tidal bands dominate at large scales. The supertidal band appears to dominate in MITgcm24 and MITgcm48 (Figure 3.5d and 3.5e) at scales ~ 50 km and smaller. The ratio of supertidal variance to total variance has a minimum at scales of ~ 250 km in all simulations, and nears one at smaller length scales in the two highest resolution simulations of MITgcm. In both HYCOM simulations, the supertidal contributions only appear to surpass the subtidal and tidal contributions at wavenumbers unlikely to be truly resolved by

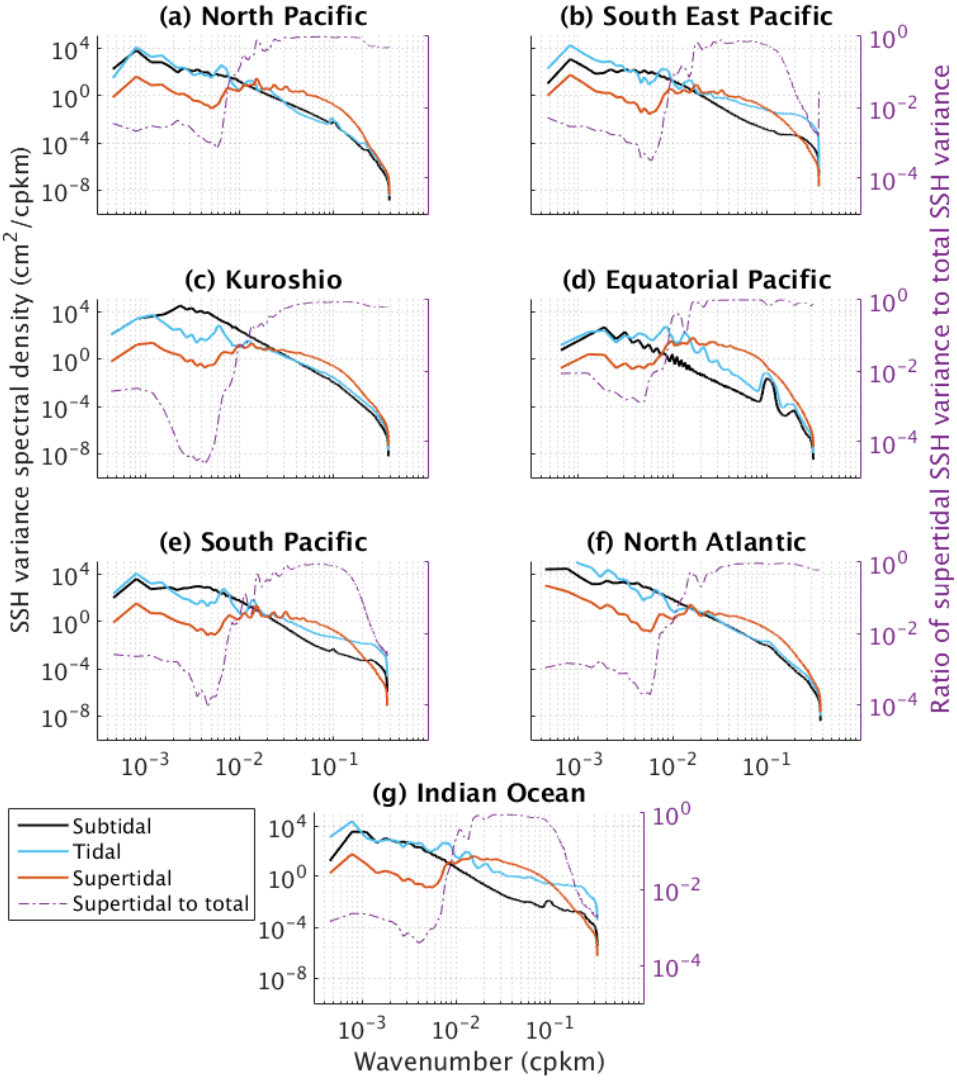

Figure 3.4: Horizontal wavenumber spectral density of SSH variance in all regions in MITgcm48 integrated over subtidal, tidal, and supertidal frequency bands (see text for definition of bands). The 95% confidence intervals span 76% to 137% of shown value for the subtidal band, 85% to 119% for the tidal band, and 94% to 107% for the supertidal band. Right-hand axis shows ratio of supertidal to total SSH variance as a function of isotropic wavenumber. Reprinted from *Savage et al.* (2017b).

the model (e.g., in the roll-off regime). Supplementary Figures 5-8 show that the contribution of supertidal variance to total variance differs by region and horizontal resolution, but is always largest at small scales. Additionally, the ratio of supertidal to total variance nears one in the North Pacific, Equatorial Pacific, and Indian Ocean regions, all regions known to have large IGW activity, in HYCOM25, MITgcm24, and MITgcm48. This differs from the results shown in Figure 3.5, suggesting that away from western boundary currents, the supertidal frequency band dominates at small scales in HYCOM and MITgcm simulations with sufficiently high horizontal resolution. While *Richman et al.* (2012) stated that the high-frequency contributions to high-wavenumber spectra were due to internal tides, *Müller et al.* (2015) demonstrated that some HYCOM simulations in fact carried a partial IGW continuum. Here, we have shown that the IGW continuum also contributes to the high-frequency portion of the SSH variance wavenumber spectral density (Figures 3.2-3.5), and in some regions dominates in the highest resolution simulations. As in *Qiu et al.* (2017), the length scale at which the supertidal band begins to dominate over the subtidal band was averaged over all simulations in each region, and the length scales are listed in the final column of Table 3.1. These length scales can be grouped into three categories: (1) highly eddying, high latitude regions (the Kuroshio and North Atlantic regions), (2) low eddying, high latitude regions (the North Pacific, South Pacific, and South East Pacific regions), and (3) low eddying, low latitude regions (the Equatorial Pacific and Indian Ocean regions). The highly eddying, high latitude regions tend towards the smallest transition length scales, whereas the low eddying, low latitude regions tend towards the largest transition length scales. As with kinetic energy, the transition length scales of SSH are dependent both on latitude and eddy activity (*Qiu et al.*, 2017). This suggests that the contamination of mesoscale and submesoscale motions in the upcoming SWOT mission will depend on latitude and eddy activity, correlating with the length scales at which supertidal frequencies dominate over the

subtidal frequencies.

The differences in the prominence of supertidal motions at small scales with increasing model resolution are more apparent in Figure 3.6, that plots the same spectral densities as in Figure 3.5 but with the subplots separated by frequency band instead of by horizontal resolution. In Figure 3.6 we therefore see spectral densities at different model resolutions on the same vertical scales. In addition, Figure 3.6 plots spectral densities for the North Pacific as well as for the Kuroshio. In the subtidal and tidal frequency bands (Figures 3.6a-3.6d), the five simulations are relatively well matched at low wavenumbers. The higher resolution simulations display greater high-wavenumber variance in the subtidal and tidal bands in both the North Pacific and Kuroshio regions. In the supertidal band (Figures 3.6e and 3.6f), the models show different behaviors in the two regions shown. In the North Pacific, there is a large increase in high-wavenumber variance as horizontal resolution increases in both models (Figure 3.6e). HYCOM25 has larger variance at these wavenumbers than its resolution counterpart, MITgcm24. However, in the Kuroshio, the increase of high-wavenumber supertidal variance with increased model horizontal resolution is highly pronounced in the MITgcm simulations, and less pronounced in the HYCOM simulations. As the output from HYCOM25 and MITgcm48 was collected from similar times of year, (October-January for MITgcm48 and January-March for HYCOM25), the seasonality of the Kuroshio extension (*Rocha et al.*, 2016b) is unlikely to contribute to this mismatch.

To further examine that the increase in energy with model horizontal resolution, the spectral slopes of the subtidal, tidal, and supertidal wavenumber spectral densities shown in Figures 3.4-3.6, and Supplementary Figures 5-8, were computed in all seven regions in all five simulations, and plotted in Figure 3.7. The slopes were computed over scales ranging from 70-250 km (*Xu and Fu*, 2012; *Richman et al.*, 2012) for the subtidal and tidal bands, and over scales 30-70 km for the supertidal

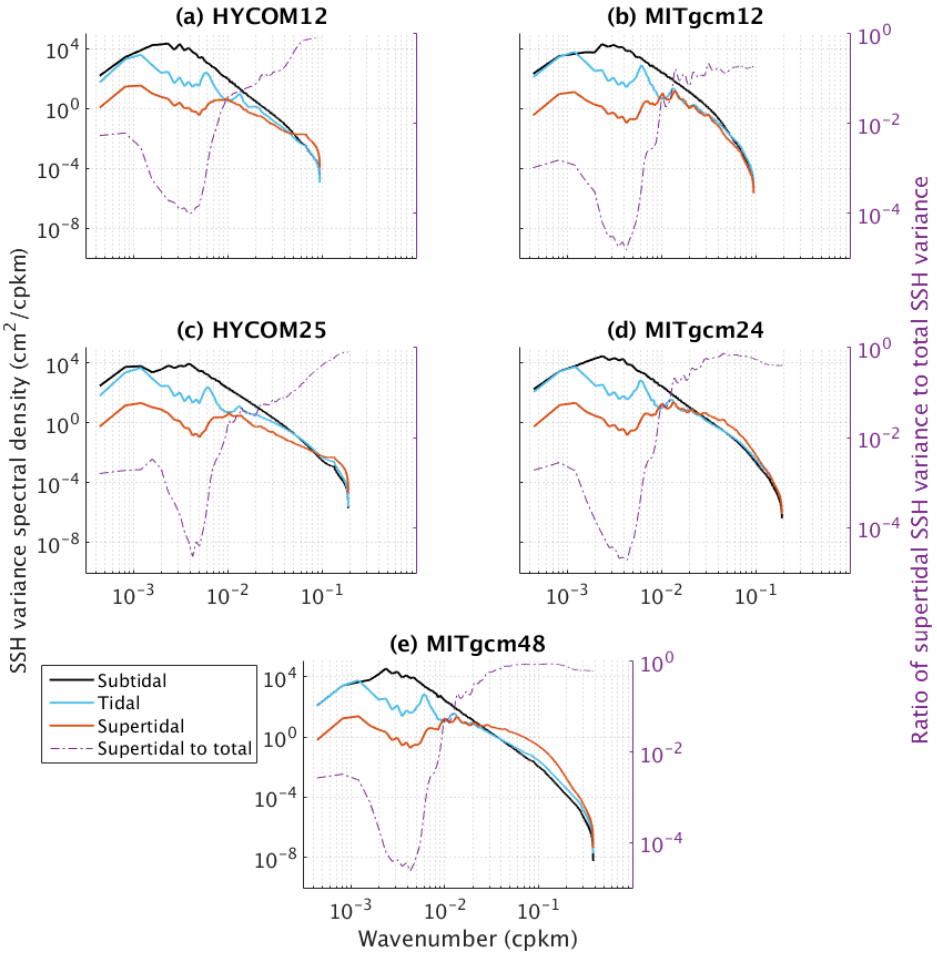

Figure 3.5: Horizontal wavenumber spectral density of SSH variance in Kuroshio region integrated over subtidal, tidal, and semidiurnal frequency bands in all five simulations. See text for definition of bands. The 95% confidence intervals span 76% to 137% of shown value for the subtidal band, 85% to 119% for the tidal band, and 94% to 107% for the supertidal band. Right-hand axis shows ratio of supertidal to total SSH variance as a function of isotropic wavenumber. Reprinted from *Savage et al.* (2017b).

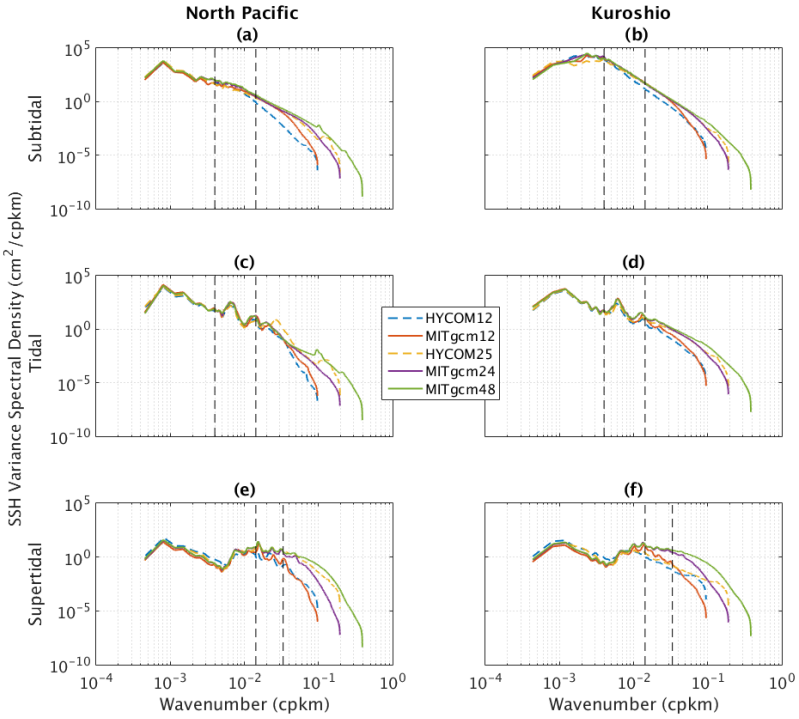

Figure 3.6: Horizontal wavenumber spectral density in Kuroshio and North Pacific regions integrated over subtidal, tidal, and semidiurnal frequency bands in all five simulations separated by frequency band. See text for definition of bands. The 95% confidence intervals span 76% to 137% of shown value for the subtidal band, 85% to 119% for the tidal band, and 94% to 107% for the supertidal band. The wavenumbers between the dashed lines were used to compute spectral slopes. Reprinted from *Savage et al.* (2017b).

band. The wavenumber ranges are given by dashed black lines in Figure 3.6. The wavenumber ranges used to compute spectral slopes in the supertidal band are chosen to be different than those of the other two frequency bands because the large jump in energy seen in the supertidal frequency band generally falls within the mesoscale band, making calculation of slopes over that region impractical. Figure 3.7a, displaying spectral slopes calculated from the subtidal band, shows that the slopes in five of the seven regions fall approximately within the internal quasi-geostrophy (k^{-5}) and surface quasi-geostophy ($k^{-11/3}$) theoretical slopes (*Stammer*, 1997; *Le Traon et al.*, 2008; *Sasaki and Klein*, 2012), indicated by black horizontal lines labeled QG and SQG, respectively. The slopes calculated from the Kuroshio region (labeled "KU" on the x-axis) are closest to the theoretical interior QG slopes, yet shallower, consistent with previous studies (*Le Traon et al.*, 2008; *Sasaki and Klein*, 2012; *Richman et al.*, 2012). The North Pacific region (labeled "NP" on the x-axis) shows flatter slopes than the other six regions, and shallower than the SQG prediction, similar to results in *Richman et al.* (2012). In the tidal band (Figure 3.7b), the slopes in all regions tend to shift upwards towards the k^{-2} (*Garrett and Munk*, 1972) internal gravity wave line (indicated by a black horizontal line labeled "IGW"). While some of the simulations in the North Atlantic (labelend "NA") have steeper slopes, all other tidal slopes in Figure 3.7b are shallower than k^{-3}. It should be noted that the *Garrett and Munk* (1972) predictions of k^{-2} are meant to be applicable to the supertidal IGW continuum, and are not necessarily expected to hold for internal tides. In the supertidal band (Figure 3.7c), the slopes measured span the full range shown, from almost k^{-7} in HYCOM12 in the Equatorial Pacific (labeled "EQPAC") to $\sim k^{-1}$ in all regions in MITgcm48. While there is little consistency regarding which simulation measures the steepest or shallowest slopes in Figures 3.7a and 3.7b, there is a clear trend in Figure 3.7c. Over all seven regions, the HYCOM25 slopes are always shallower than the HYCOM12 slopes, and the MITgcm slopes become progressively shallower as

resolution increases from MITgcm12 to MITgcm24 to MITgcm48. The MITgcm25 slopes generally lie closest to the predicted k^{-2} value, while the MITgcm48 slopes are shallower, hovering around k^{-1}. In the Kuroshio and North Atlantic regions, the supertidal slopes measured in HYCOM12 and HYCOM25 are similar, consistent with what is seen in Figure 3.6c. In the MITgcm simulations, the difference between the slopes measured in MITgcm12 and MITgcm24 are larger than the difference between slopes in MITgcm24 and MITgcm48 in the North Pacific, the Kuroshio, the Equatorial Pacific, and the North Atlantic regions. In most regions, the spectral slope of the supertidal frequency band computed from both models increases similarly between the $\sim 1/12^\circ$ and $\sim 1/24^\circ$ simulations. While neither HYCOM12 nor MITgcm12 consistently has slopes shallower than the other, the spectral slopes measured from MITgcm24 are consistently shallower than those measured in HYCOM25, except in the North Pacific, that appears as an outlier for HYCOM25 in Figure 3.7c. In general, the slopes measured from the MITgcm simulations tend to be similar across all regions for each horizontal resolution, but the slopes measured from the HYCOM simulations vary greatly by region, particularly in HYCOM12. Both models need to be compared to more data to discover which, if either, is more closely capturing oceanic IGW dynamics. Figures 3.6 and 3.7 suggest that, while these two models show some agreement at frequencies lower than $\sim 2\,\mathrm{cpd}$, their differences in wave drag, vertical discretization, subgridscale parametrizations, and resolution have a noticeable effect at high-frequencies that are a component of the small-scale phenomena (*Richman et al.*, 2012; *Callies and Ferrari*, 2013; *Rocha et al.*, 2016a) of interest for the upcoming SWOT altimeter mission.

3.4 Summary

The frequency-horizontal wavenumber spectral densities of SSH variance, computed over seven regions from five simulations of the two models, at horizontal reso-

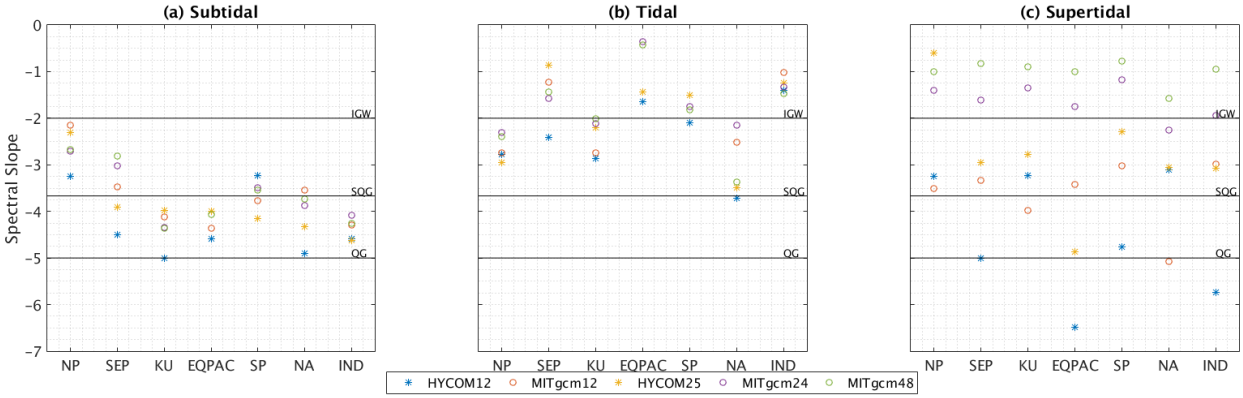

Figure 3.7: Spectral slopes computed from all five simulations in the (a) subtidal, (b) tidal, and (c) supertidal frequency bands. Slopes were computed over wavenumbers ranging from 1/250-1/70 cpkm in the subtidal and tidal bands, and over wavenumbers ranging from 1/70-1/30 cpkm in the supertidal band. Abbreviations for the regions are listed in Table 3.1. Reprinted from *Savage et al.* (2017b).

lutions ranging from 1/12° to 1/48°, display high variance along the linear dispersion curves of low vertical mode IGWs. This demonstrates that global ocean models such as HYCOM and MITgcm are beginning to resolve SSH signatures of the IGW continuum. We have also shown that increasing the model horizontal resolution increases the modeled IGW continuum SSH variance. The contributions to SSH wavenumber spectral density from three frequency bands (subtidal, tidal, and supertidal), reiterate the fact that high-frequencies contribute to, and sometimes dominate, the SSH variance at small scales of interest for the SWOT mission. The transition length scale where the supertidal band dominates the SSH variance wavenumber spectral density over the subtidal band is dependent on latitude (where low latitudes tend towards larger transition length scales) and eddy activity (where regions of high eddy activity tend towards smaller transition length scales). This is consistent with the transition length scales for kinetic energy derived from Acoustic Doppler Current Profiler observations, discussed in *Qiu et al.* (2017). Understanding this transition could be of vital importance to the SWOT mission, that aims to study wavelengths down to 15 km.

However, the differences in the HYCOM and MITgcm simulations, such as the presence of a topographic internal wave drag parametrization, differences in horizontal and vertical resolution, differences in vertical discretization schemes, and differences in subgridscale closures all impact the variance measured in the supertidal frequency band at scales $\sim 70\,\mathrm{km}$ and smaller. Tidal and supertidal motions, aliased by satellite altimetry, will need to be properly understood and mapped if we are to gain meaningful insight regarding the dynamics of both high- and low-frequency motions at small scales from this upcoming mission.

CHAPTER IV

Global maps of non-steric and steric sea surface height variance

4.1 Introduction

Global maps of sea surface height (SSH) variance attributed to different ocean dynamics have been displayed in numerous studies (*Ducet et al.*, 2000; *Le Provost*, 2001; *Carrère and Lyard*, 2003; *Zhao et al.*, 2016) and have facilitated the understanding of these dynamics. One simple way we can recreate many of these maps is by dividing the SSH variance into different frequency bands associated with different physical processes. Here, we use a $1/25^\circ$ resolution simulation of the HYbrid Coordinate Ocean Model (HYCOM) to construct global maps of SSH variability. The HYCOM output is separated into steric and non-steric SSH, and into subtidal, diurnal, semidiurnal, and supertidal frequency bands (Figure 1.1). The division of the modeled spectral densities into steric and non-steric components aids in associating the SSH variability with physical processes. For instance, mesoscale eddies and western boundary currents dominate subtidal steric SSH variability (*Le Traon and Morrow*, 2001). Atmospheric pressure loading and winds contribute importantly to non-steric SSH variance over a wide range of frequencies, from supertidal to annual and longer (*Ponte and Gaspar*, 1999; *Shriver and Hurlburt*, 2000; *Stammer et al.*, 2000; *Tierney et al.*, 2000; *Fu and*

Cazenave, 2001; *Carrère and Lyard*, 2003). Diurnal and semidiurnal barotropic tides contribute importantly to non-steric SSH (*Le Provost*, 2001) and diurnal and semidiurnal internal tides contribute importantly to steric SSH variance (*Ray and Mitchum*, 1997; *Shriver et al.*, 2012; *Ray and Zaron*, 2016). Finally, the internal gravity wave continuum contributes to the steric supertidal SSH variance (*Glazman and Cheng*, 1999).

A major focus of this study is the steric SSH variability due to stationary internal tides, non-stationary internal tides, and the internal gravity wave (IGW) continuum. As shown in Chapter III, high-frequency phenomena such as tides and IGWs have significant variance at the high wavenumbers targeted by the upcoming Surface Water and Ocean Topography (SWOT) satellite mission. Several previous studies have developed empirical maps of stationary internal tides (*Dushaw et al.*, 2011; *Ray and Zaron*, 2016; *Zhao et al.*, 2016). As the non-stationary internal tides and the IGW continuum are less predictable than the stationary internal tides, their aliased signals will be harder to identify than those of stationary internal tides, posing a greater challenge to the altimeter community. We take a step towards understanding this challenge by producing global maps of the geographical variability of non-stationary and stationary internal tides and the IGW continuum.

4.2 Methodology

To map the SSH variance of steric and non-steric SSH, we use hourly global HYCOM output (described in Section 2.2.1) that has been subsampled at $\sim 1/4^\circ$ horizontal resolution as a time saving measure. The steric and non-steric SSH was computed as given in Appendix B. We compute pointwise frequency spectral densities (Equation 2.2) and integrate over the four frequency bands shown in Figure 1.1 using Equation 2.3. From the maps, we compute a spatial average of SSH variance defined as

$$Spatial\ Average = \frac{\int\int \eta^2 dA}{\int\int dA}, \tag{4.1}$$

where η^2 is the SSH variance and dA is the area of an individual gridpoint. We compute the spatial average only over gridpoints in the deep ocean (seafloor depth$>$ 1 km). While the global maps displayed in this chapter were created using output from the 1/25° simulation of HYCOM, both the 1/12.5° (HYCOM12) and the 1/25° (HYCOM25) were used to create estimated spatial averages of variance to understand the dependence of variance on horizontal model resolution. In the construction of our global maps, within the diurnal and semidiurnal bands, we compute the total and non-stationary SSH variances. The non-stationary component is calculated by removing the harmonics of the five tidal constituents introduced into these HYCOM simulations via harmonic analysis (*Ray*, 1998) before spectral densities and variances are computed. The degree of non-stationarity computed here is a function of the one-year record length of our HYCOM output, consistent with *Ansong et al.* (2015), that showed that the non-stationarity of the tidal signal increases as the record length increases. The dependence of non-stationary signals on record length could be an important caveat in the study of tides via satellite altimetry.

4.3 Global Maps of SSH Variance

Here, we show global maps of steric and non-steric SSH integrated over subtidal, diurnal, semidiurnal, and supertidal frequency bands. The spatial average values (Equation 4.1) for the full, steric and non-steric SSH in subtidal, diurnal, semidiurnal, and supertidal bands, and for the non-stationary components of the diurnal and semidiurnal bands, are given in Table 4.1 and summarized visually in Figure 4.1, both of which will be referenced throughout the remainder of this section.

The maps of band-integrated steric and non-steric variance in the four frequency

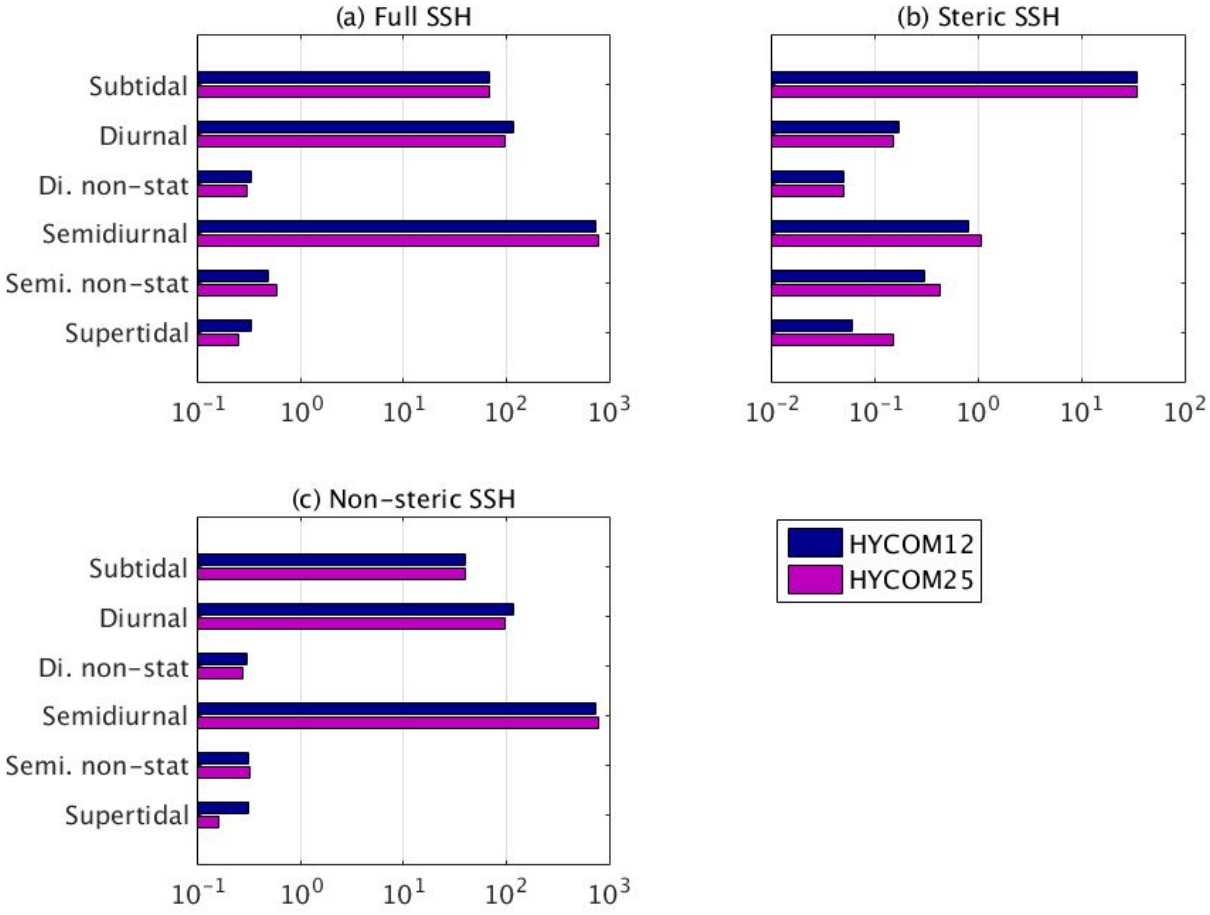

Figure 4.1: Bar graph of HYCOM12 and HYCOM25 variance in cm^2 in subtidal, diurnal, non-stationary diurnal, semidiurnal, non-stationary semidiurnal, and supertidal bands in (a) full, (b) steric, and (c) non-steric SSH. Variance was calculated over deep ocean gridpoints (seafloor depths greater than 1 km). Axis limits differ between subplots. Reprinted from *Savage et al.* (2017a).

SSH		Subtidal	Diurnal	Di. (non-stat.)	Semidiurnal	Semidi. (non-stat.)	Supertidal
Full	$H12$	68.71	117.05	0.33	735.12	0.48	0.33
	$H25$	69.24	97.41	0.30	785.06	0.58	0.25
Steric	$H12$	34.89	0.17	0.05	0.80	0.30	0.06
	$H25$	34.83	0.15	0.05	1.05	0.43	0.15
Non-Steric	$H12$	39.63	116.96	0.30	734.79	0.31	0.31
	$H25$	40.00	97.34	0.27	784.59	0.32	0.16

Table 4.1: Globally averaged variance (cm^2) for full, steric, and non-steric SSH in subtidal, diurnal (both full and non-stationary), semidiurnal (both full and non-stationary), and supertidal bands in HYCOM12 (H12) and HYCOM25 (H25). Variance was calculated over deep ocean gridpoints (seafloor depths greater than 1 km). Reprinted from *Savage et al.* (2017a).

bands, shown in Figures 4.2-4.7, exhibit features familiar from earlier studies, which will be discussed throughout this section. Note that the axis limits are not in general equal across the subplots. Figure 4.2 shows maps of steric and non-steric SSH variability in subtidal frequencies. The map of subtidal steric SSH, Figure 4.2a, highlights strongly eddying regions, such as western boundary currents, consistent with many earlier analyses, e.g. *Ducet et al.* (2000). The non-steric subtidal map, Figure 4.2b, shows high variability in the high latitudes, due to wind and pressure forcing (*Stammer et al.*, 2000; *Tierney et al.*, 2000; *Carrère and Lyard*, 2003). HYCOM includes the dynamic effects of atmospheric pressure as well as the static inverted barometer (IB) effect (*Ponte and Gaspar*, 1999). Pressure- and wind-forcing drive non-steric SSH variability over all frequency bands studied here and yield particularly strong variability at periods of 3-4 days, primarily at mid-high latitudes, where SSH variability can be as large as 15 cm (*Fu and Chelton*, 2001). These large variations occur primarily in the Southern Ocean where atmospheric pressure forcing is at a maximum. Our maximum HYCOM25 subtidal non-steric SSH variance in the Southern Ocean is 22 cm. The subtidal non-steric SSH variance is likely dominated by pressure-forcing and is also strongly impacted by atmospheric wind forcing (*Carrère and Lyard*, 2003).

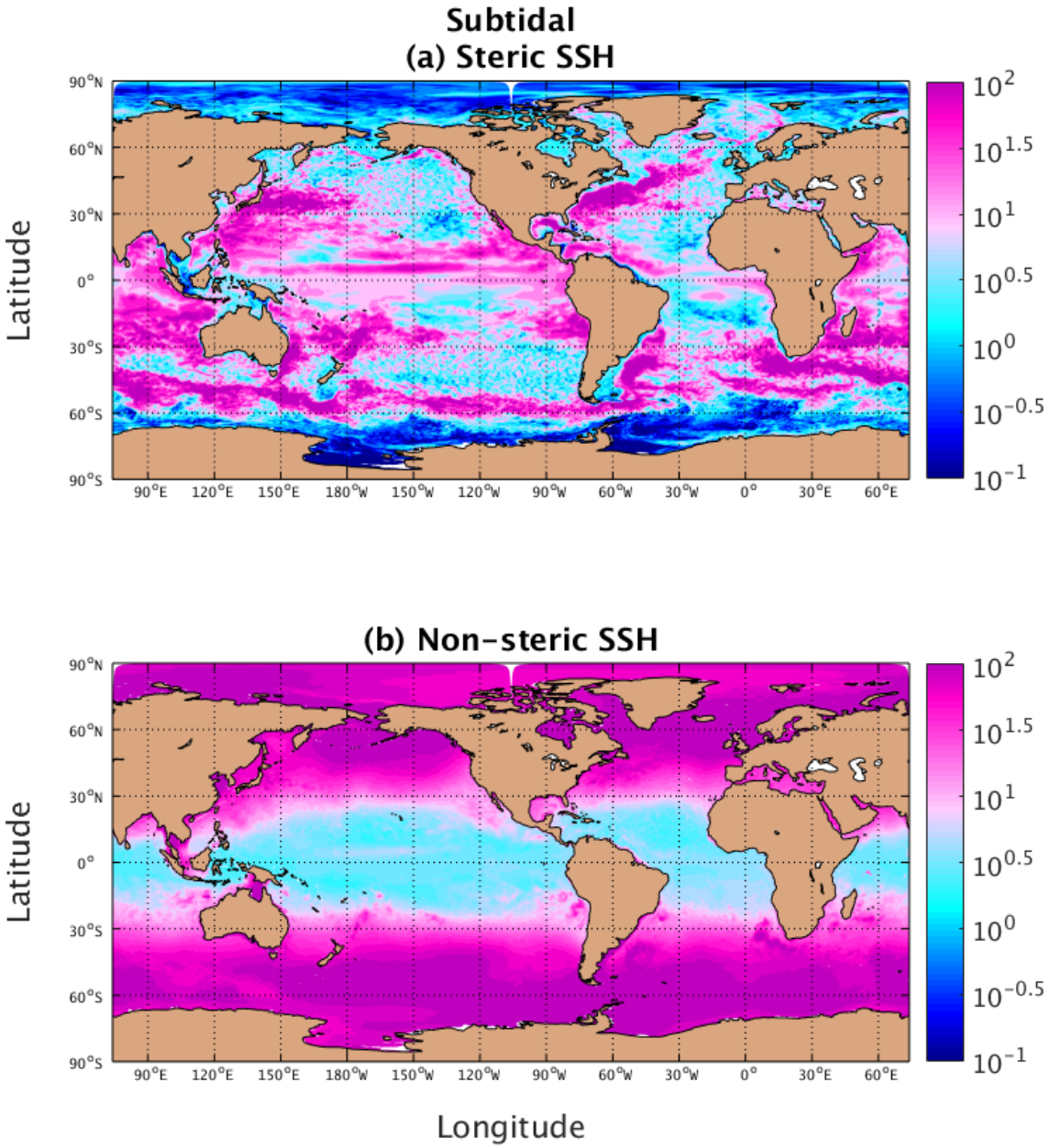

Figure 4.2: Global SSH variance (cm^2) from HYCOM25 in the subtidal band (frequencies 1/366 cycles per day to 0.86 cycles per day). The 95% confidence intervals range from 96% to 104% of shown value. In this and subsequent figures, steric (a) and non-steric (b) variances are shown. Reprinted from *Savage et al.* (2017a).

The non-steric maps of the diurnal and semidiurnal bands, respectively shown in Figures 4.3b and 4.4b, show the classic barotropic tidal patterns seen in many previous studies, e.g. *Le Provost* (2001) and *Egbert et al.* (1994). The HYCOM25 diurnal non-steric map has a spatially averaged global variance of $97.41\,\mathrm{cm}^2$ and the semidiurnal non-steric map has a spatially averaged global variance of $785.06\,\mathrm{cm}^2$ (Table 4.1). The HYCOM tidal variances found here are comparable with those of previous studies (*Arbic et al.*, 2004), though the semidiurnal variances are smaller by about 10% for unknown reasons. The five constituents used in HYCOM12 and HYCOM25 contribute 97% of the global variance found in the ten largest tidal constituents in GOT99.2 (**?**). Therefore, one could expect an increase in variance of a few percent in the non-steric and steric SSH variance estimates in both the diurnal and semidiurnal bands if more constituents were included in the HYCOM simulations. The steric diurnal and semidiurnal maps, Figures 4.3a and 4.4a, show the diurnal and semidiurnal internal tidal signals. The diurnal steric SSH, Figure 4.3a, does not propagate poleward of 30°, consistent with theory (*Gill*, 1982; *Shriver et al.*, 2012). The semidiurnal steric sea level map (Figure 4.4a) displays a spatial distribution similar to maps of the M_2 internal tide constructed from altimeter data (*Dushaw et al.*, 2011; *Ray and Zaron*, 2016; *Zhao et al.*, 2016). The map in Figure 4.4a highlights regions of known large semidiurnal internal tides, for example, north of the Hawai'ian islands, near French Polynesia, and between Tasmania and Australia. In both the semidiurnal bands, the global steric SSH (internal tide) variance increases from HYCOM12 to HYCOM25 (Figure 4.1), indicating that model resolution is an important factor in modeling the internal tides. The global variance for the semidiurnal internal tide increases from $0.80\,\mathrm{cm}^2$ in HYCOM12 to $1.05\,\mathrm{cm}^2$ in HYCOM25 (Table 4.1), approximately equal to the $\sim 0.96\,\mathrm{cm}^2$ estimated from *Zaron* (2015). For reasons we do not understand, but which may have to do with the lack of retuning of the wave drag in HYCOM25, the globally averaged full, steric, and non-steric SSH variances in the diurnal band

decrease slightly from HYCOM12 to HYCOM25, in contrast to the results in the semidiurnal band which shows increased variance with an increased resolution. The geographies of diurnal and semidiurnal internal wave generation differ from each other (*Egbert and Ray*, 2003), implying the wave drags for the two types of motions should be tuned separately; this would be very difficult to do in present simulations.

Figures 4.5 and 4.6 respectively show global maps of the diurnal and semidiurnal tidal band variance after the stationary part of the tide has been removed. Low-latitude and equatorial regions tend to display the largest signals in the non-stationary diurnal and semidiurnal steric (internal tide) maps (*Zaron*, 2017), and the high variance regions are correlated with the total internal tidal signals (Figures 4.3a and 4.4a). The global HYCOM25 maps of non-stationary steric SSH (internal tides) have a spatially averaged global variance of $0.05\,\mathrm{cm}^2$ in the diurnal band and $0.43\,\mathrm{cm}^2$ in the semidiurnal band (Table 4.1), the latter being comparable to the $\sim 0.33\,\mathrm{cm}^2$ estimated from *Zaron* (2015). HYCOM25 variance is nearly equal to HYCOM12 variance in the non-stationary diurnal band and is larger than HYCOM12 in the non-stationary semidiurnal band (Figure 4.1). The non-stationary component of the non-steric semidiurnal SSH ($0.32\,\mathrm{cm}^2$) is smaller than the non-stationary component of the steric semidiurnal SSH ($0.43\,\mathrm{cm}^2$; Table 4.1), consistent with the idea that semidiurnal internal tide signals have a substantial non-stationary component (*Zilberman et al.*, 2011).

Maps of the supertidal variance are displayed in Figure 4.7. The largest non-steric supertidal variance (Figure 4.7b) is along the coastlines where overtides (higher harmonics of the barotropic tide) are largest (*Ray*, 2007). The non-steric supertidal variance is approximately an order of magnitude smaller in the open ocean. The variance in this band is due in part to wind and atmospheric pressure forcing (*Carrère and Lyard*, 2003), and in part to overtides. The global non-steric supertidal variance is $0.16\,\mathrm{cm}^2$ in HYCOM25, less than the value in HYCOM12 (Figure 4.1). The drop in

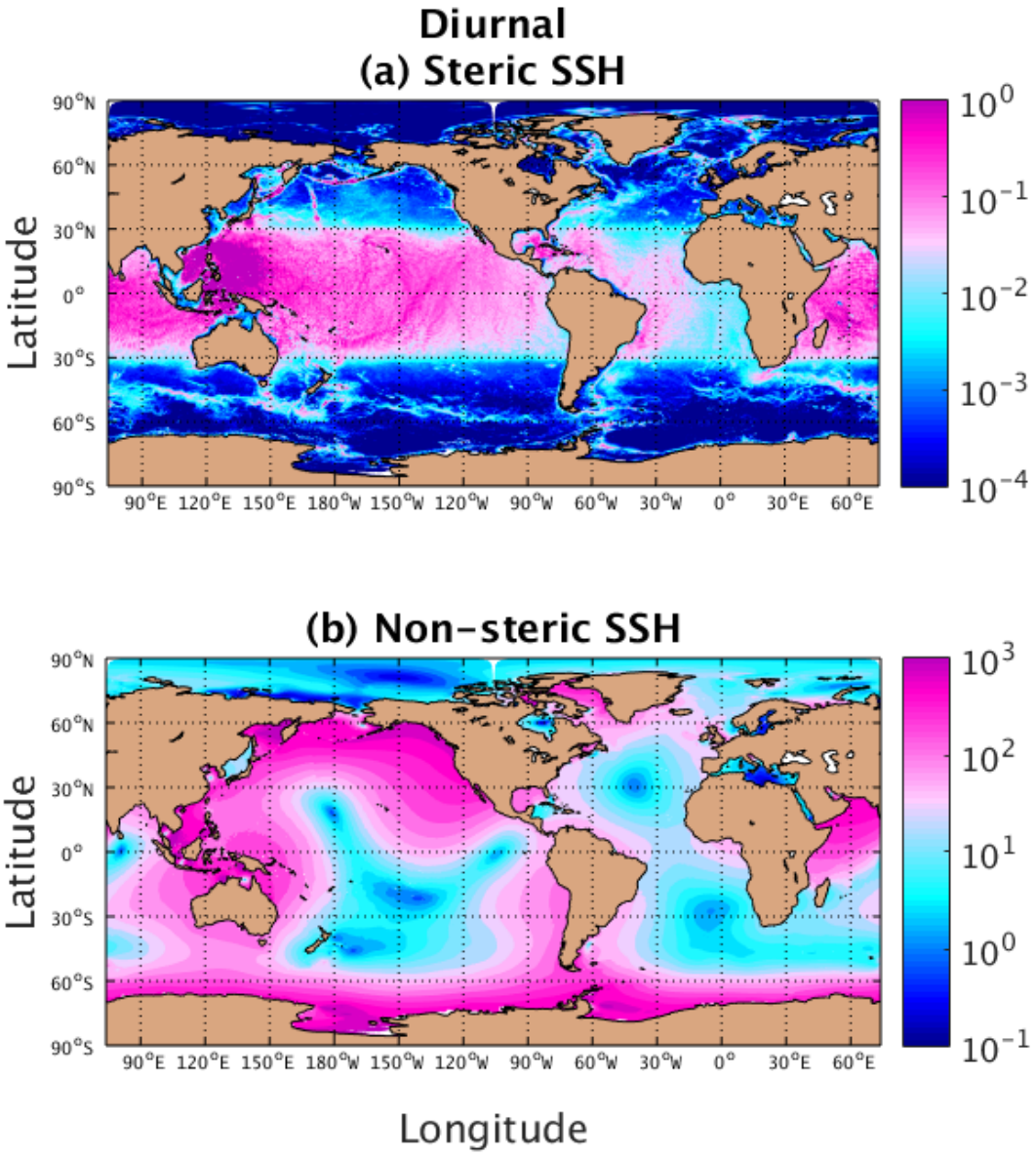

Figure 4.3: Global SSH variance (cm^2) from HYCOM25 in the diurnal band (frequencies 0.87 cycles per day to 1.05 cycles per day). The 95% confidence intervals range from 92% to 109% of shown value. Reprinted from *Savage et al.* (2017a).

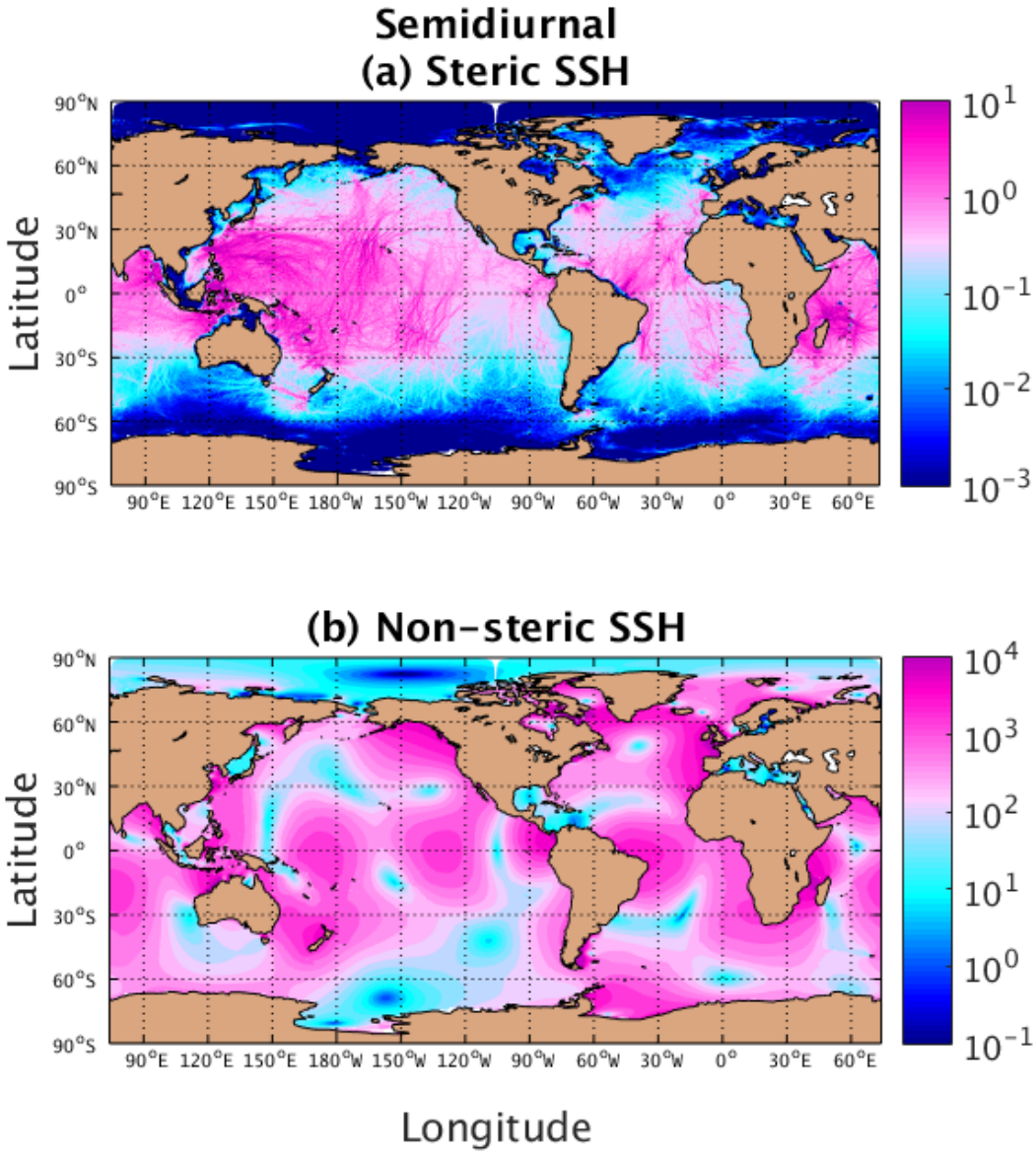

Figure 4.4: Global SSH variance (cm^2) from HYCOM25 in the semidiurnal band (frequencies 1.86 cycles per day to 2.05 cycles per day). The 95% confidence intervals range from 92% to 109% of shown value. Reprinted from *Savage et al.* (2017a).

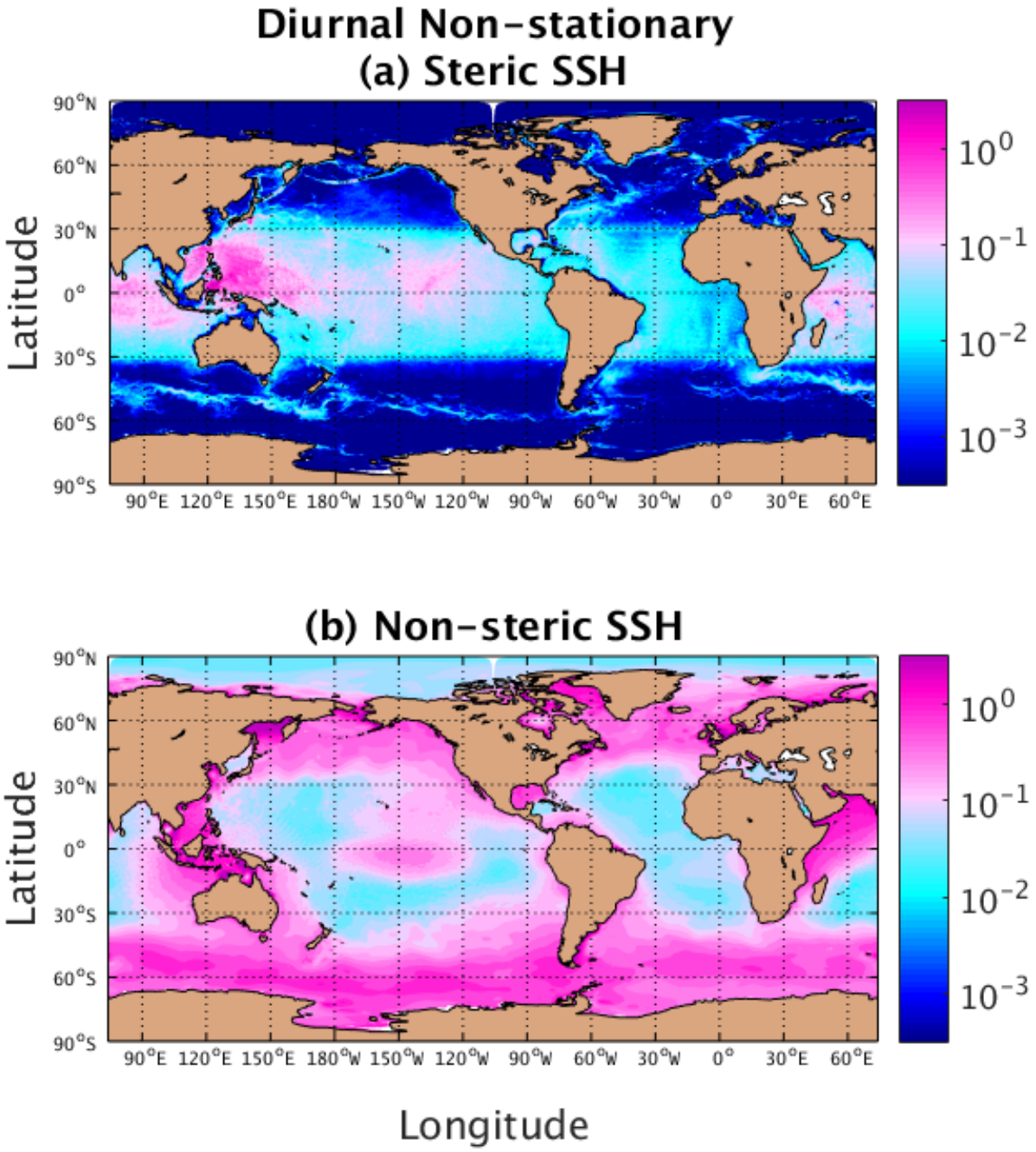

Figure 4.5: Global SSH variance (cm^2) from HYCOM25 in the diurnal band (frequencies 0.87 to 1.05 cycles per day) after stationary tides have been removed via harmonic analysis. The 95% confidence intervals range from 92% to 109% of shown value. Reprinted from *Savage et al.* (2017a).

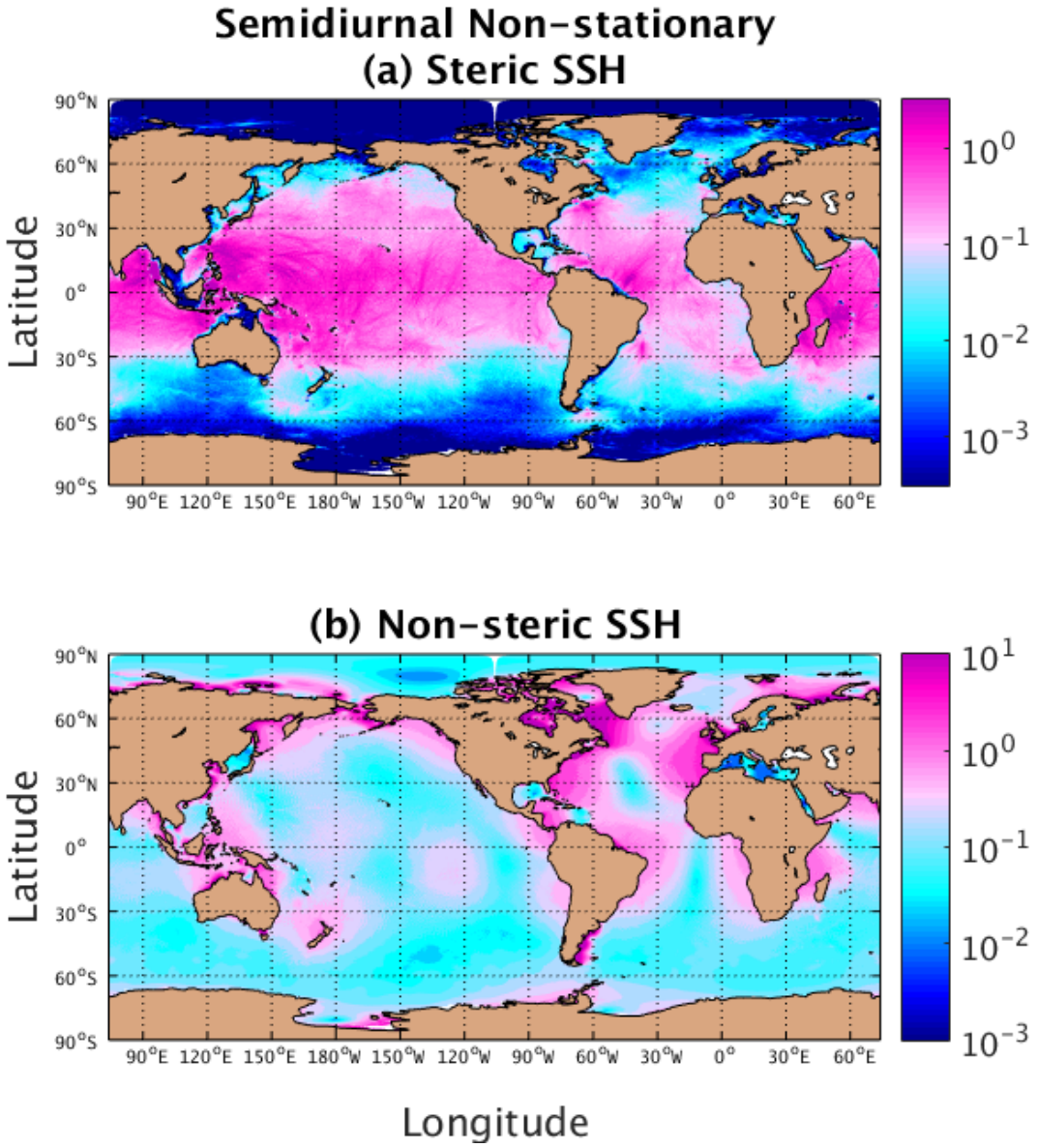

Figure 4.6: Global SSH variance (cm^2) from HYCOM25 in the semidiurnal band (frequencies 1.86 cycles per day to 2.05 cycles per day) after stationary tides have been removed via harmonic analysis. The 95% confidence intervals range from 92% to 109% of shown value. Reprinted from *Savage et al.* (2017a).

variance in the non-steric supertidal band from HYCOM12 to HYCOM25 is consistent with Table 2.3 and is perhaps related to the low amplitudes of overtides in HYCOM25 as discussed in Chapter 2.4.1.

The steric supertidal map, Figure 4.7a, represents a global estimate of SSH variance in the internal gravity wave continuum. As with the semidiurnal steric SSH map, the largest amplitudes are generally seen along the equator and in low latitudes. Again, comparison of HYCOM12 and HYCOM25 in Figure 4.1 indicates that increasing the horizontal resolution of the model yields increased variance in the IGW continuum, consistent with results in *Müller et al.* (2015). The global continuum variance increases from $0.06\,\mathrm{cm}^2$ in HYCOM12 to $0.15\,\mathrm{cm}^2$ in HYCOM25 (Table 4.1). The diurnal internal tidal band variance of $0.15\,\mathrm{cm}^2$, the semidiurnal internal tidal band variance of $1.05\,\mathrm{cm}^2$, the non-stationary internal semidiurnal tidal band variance of $0.43\,\mathrm{cm}^2$, and the IGW continuum band variance of $0.15\,\mathrm{cm}^2$ are measurable signals that contribute to the high-frequency, high-wavenumber variance of interest to SWOT (*Richman et al.*, 2012; *Callies and Ferrari*, 2013; *Rocha et al.*, 2016a).

4.4 Summary

In this chapter, we use a global general circulation ocean model forced by atmospheric fields and tides to map the global steric and non-steric SSH contributions in subtidal, diurnal, semidiurnal, and supertidal frequency bands. Comparison with previous results in the literature indicates that the model captures well-known phenomena such as mesoscale eddies and western boundary currents (steric subtidal), the barotropic tides (non-steric diurnal and semidiurnal), internal tides (steric diurnal and semidiurnal), and both low- and high-frequency barotropic motions driven by atmospheric pressure loading and winds (non-steric subtidal and supertidal).

The semidiurnal internal tides have variances of $1.05\,\mathrm{cm}^2$ ($0.43\,\mathrm{cm}^2$ in the non-stationary component). The non-stationary component is most prominent at low-

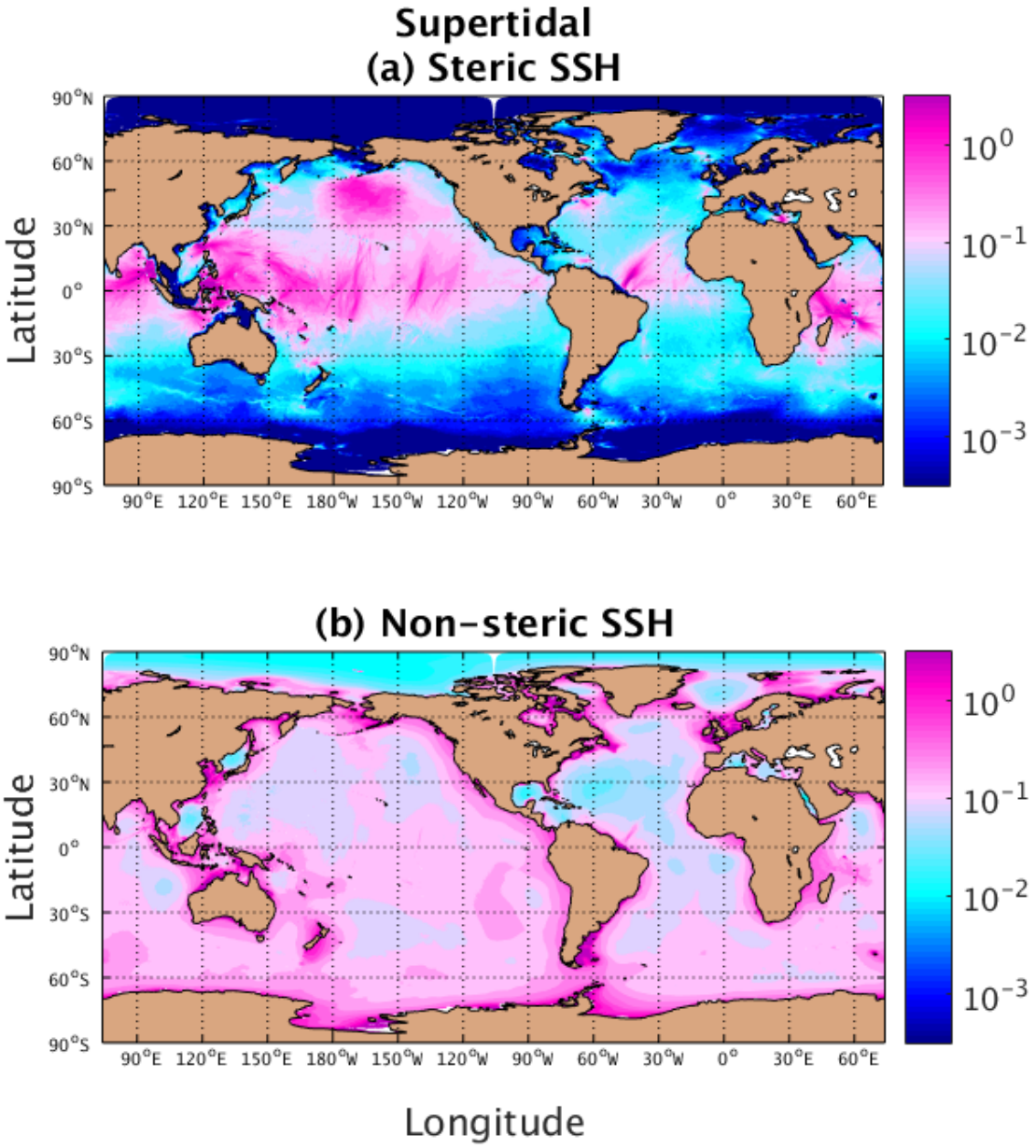

Figure 4.7: Global SSH variance (cm^2) from HYCOM25 in the supertidal band (frequencies 2.06 cycles per day to 12 cycles per day). The 95% confidence intervals range from 98% to 101% of shown value. Reprinted from *Savage et al.* (2017a).

latitudes. In the supertidal band, having periods ranging from 2 to 12 hours, the steric SSH variance increases from $0.06\,\mathrm{cm}^2$ in a $1/12.5^\circ$ resolution simulation to $0.15\,\mathrm{cm}^2$ in a $1/25^\circ$ resolution simulation, suggesting that the model has not yet achieved numerical convergence. The supertidal steric SSH signals in the model are generally most prominent in lower latitudes. The internal tides, both phase-locked and non-stationary, and the supertidal IGW continuum will appear as sources of "noise" in swath altimeter missions, and will obscure examination of low-frequency phenomena unless they can be accurately identified and removed.

CHAPTER V

Discussion

As internal gravity waves (IGWs) are small scale and high-frequency, they are difficult to observe and predict using current observational data. Here, we have shown that global high-horizontal resolution general circulation ocean models, such as the HYbrid Coordinate Ocean Model (HYCOM) and the MIT general circulation model (MITgcm), can be useful in the study of the internal gravity wave continuum. Both models have been compared to in-situ data. Frequency spectral densities were computed from SSH data from a set of 351 tide gauges and from SSH output from nearest neighbor grid points in $1/12.5^\circ$ and $1/25^\circ$ simulations of HYCOM. Comparison of the spectral densities shows that both simulations match data relatively well in both island and continental coastal locations. The variance in HYCOM, computed by integrating the spectral densities over four frequency bands, is representative of variance measured by tide gauges in the subtidal, diurnal, and semidiurnal bands, but is deficient compared to the tide gauge variance in the supertidal band. Comparison of the global averages of frequency band separated variance in the tide gauge data versus both HYCOM simulations shows that increasing the horizontal resolution increases the variance in the subtidal, and semidiurnal bands, and decreases in the diurnal and supertidal bands. The decrease of variance in these two bands may be due to the sensitivity of SSH variance to parametrized topographic wave drag in the model.

Frequency spectral densities of dynamic height were computed from both a 1/25° simulation of HYCOM and a 1/48° simulation of MITgcm and compared to those computed from in-situ McLane profiler data in nine locations. In five of the nine comparisons, both models resemble data relatively well across all frequencies. In the other four, there is a large gap between both models and data at frequencies just less than diurnal frequencies ($\omega < 1\,\mathrm{cpd}$). In comparing variance integrated over diurnal, semidiurnal, and supertidal frequencies, both HYCOM and MITgcm perform similarly well in the diurnal and semidiurnal bands, but, again, the 1/25° simulation of HYCOM underestimates the variance in the supertidal band compared to the in-situ data. The larger variance in the supertidal band in the 1/48° MITgcm simulation is likely a result of its higher horizontal resolution, as this is known to have an effect on the resolution of the internal gravity wave continuum. This validation against in-situ data demonstrates both models' potential to supplement the limited data available for study of the IGW continuum.

After comparing both models to in-situ data, we take advantage of the hourly, global coverage of the models to produce SSH variance frequency-horizontal wavenumber spectral densities that would be unobtainable using available in-situ data. The SSH variance frequency-horizontal wavenumber spectral densities were computed from seven locations in five simulations of HYCOM and MITgcm to study both regional dependence as well as model horizontal resolution dependence. In all simulations in all regions, large variance is seen along the linear dispersion relation curves for internal gravity waves. The large variance seen along these curves is more prominent in regions known to have large internal gravity wave activity (e.g. North Pacific region), and is less prominent in regions of high mesoscale eddy activity (e.g. Kuroshio an North Atlantic regions). It has been previously thought that high-frequency, high-wavenumber variability was dominated by internal tides. Upon integrating the frequency-horizontal wavenumber spectral densities over subtidal, tidal, and super-

tidal frequency bands, it is clear that while sometimes it is the tidal band that is dominant at small scales, in other regions the supertidal band dominates at scales of $\sim$ 30-50 km. The large variance along the IGW dispersion relation curves shows that it is likely the IGW continuum that dominates at these scales globally. However, as both models provide vastly different estimates of the supertidal frequency band contribution to small wavenumbers, more testing against data will be necessary in the near future. The transition length scale, at which the supertidal band dominates over the subtidal band, is also dependent on both latitude and eddy activity. As with kinetic energy, the SSH transition length scale tends to be smaller in regions of high-latitude, high-eddy activity. In regions of low-latitude, and low-eddy activity, the transition length scales are much larger, implying that high-frequency contamination of SWOT data will appear at larger scales in these areas.

Global maps of SSH variance arising from various oceanographic phenomena can be created by computing pointwise frequency spectral densities in non-steric and steric SSH output from both $1/12.5^\circ$ and $1/25^\circ$ simulations of HYCOM and integrating over subtidal, diurnal, semidiurnal, and supertidal frequencies. This technique is confirmed in its ability to recreate familiar maps of steric subtidal variability (mesoscale eddies and western boundary currents), non-steric diurnal and semidiurnal variability (barotropic tides), and steric diurnal and semidiurnal variability (internal tides). Because the SWOT mission will be primarily focused on small horizontal scales, the small-scale, non-stationary semidiurnal steric SSH signals are of greater interest to the SWOT mission than the larger-scale non-stationary semidiurnal non-steric SSH signals. The maps of the steric SSH variability in the tidal bands after the stationary part of the tide has been removed provide new estimates of non-stationary internal tide variance, with globally averaged variance of $0.05\,\mathrm{cm}^2$ for the diurnal non-stationary internal tide and $0.43\,\mathrm{cm}^2$ for the semidiurnal non-stationary internal tide in the $1/25^\circ$ simulation of HYCOM. This technique also produces the first global map

of supertidal steric SSH variance, attributed to the IGW continuum. The supertidal steric SSH map has a globally integrated variance of $0.16\,\mathrm{cm}^2$ with regions along the equator having variance exceeding $10\,\mathrm{cm}^2$.

With two-dimensional SSH data soon to be available from the upcoming SWOT satellite altimeter, wavenumber spectral densities will become available from a global two-dimensional dataset. These spectral densities will likely be useful in diagnosing ocean surface dynamics on a global scale. While SSH data provided by SWOT will have unprecedented global coverage, it will suffer from contamination due to aliasing of high-frequencies, as in previous altimeter missions. While phase-locked, high-frequency dynamics such as tides can be accurately removed from aliased records, aliasing of less predictable dynamics such as non-stationary tides and the IGW continuum will more likely cause contamination in the estimation of low-frequency signals from altimetry. The regions of large variance in the supertidal steric SSH maps, discussed in Chapter IV, are likely indicative of regions of large IGW activity, and may cause complications in the analysis of SSH data provided by SWOT. An additional complication arises due to the fact that the high-wavenumbers of interest for the SWOT mission are dominated by high-frequency phenomena such as internal tides, both stationary and non-stationary, and the IGW continuum. In order to gain meaningful insight concerning these small-scale dynamics, non-stationary tides and the IGW continuum will have to be properly understood and accurately mapped and removed before the low-frequency signals of interest can be accurately studied.

To continue the work presented here, two projects would likely provide invaluable insight. Firstly, as stated in Chapter III, the global models used for study are not expected to resolve submesoscale dynamics. The submesoscale is often thought to be small-scale ($\sim 10\,\mathrm{km}$) and fall within the subtidal band. To study the submesoscale with global ocean models, much higher horizontal and vertical resolution is required. It would be advantageous to repeat the diagnostics used in Chapter III, and com-

pute frequency-horizontal wavenumber spectral densities of SSH in simulations with high enough resolution to resolve submesoscale dynamics. Currently, preparations are being made to conduct such a study using an MITgcm simulation with 1/96° horizontal resolution and 300 vertical layers. It has been conjectured that in simulations such as these, the subtidal band would dominate at scales not measurable in the simulations described in this thesis, due to the models potential resolution of submesoscale dynamics. This could be crucial information to the SWOT community, as the low-frequency submesoscale is of primary focus for the SWOT mission. Secondly, an increased understanding of the physical manifestation of non-stationary internal tides would provide further insight into some of the results discussed in this thesis. As stated in Chapter IV, the non-stationary component of internal tides is largely dependant on the duration of the record. Additionally, the mechanism by which low-frequency eddies modulate the stationary tidal signal is not well understood. A project is planned to study the non-stationary tide in more detail than presented here. In this project, we will use models of simple harmonic oscillators and introduce low-frequency modulation and noise into the system to see how the spectral peak of the harmonic oscillator is affected. We will also take advantage of the steric/non-steric SSH split in HYCOM to examine how non-stationarity effects barotropic vs. baroclinic tides. An increased understanding of non-stationary tidal signals would undoubtedly aid the altimetry community in the removal of such signals from aliased data.

SWOT may be able to contribute to the study of the IGW continuum and its influence on ocean mixing. If the community were able to extrapolate information on the spatial distribution and dissipation of internal gravity waves, it may go a long way to providing ocean mixing data with unprecedented global coverage. While Argo floats have provided invaluable information regarding global mixing, still more observational data is necessary to understand the influences of both abyssal and

surface ocean mixing on the meridional overturning circulation and its associated poleward heat transport. Global maps of SSH variability from IGWs may also assist satellite missions measuring sea surface temperature and concentrations of carbon dioxide in understanding the absorption of excess heat and carbon dioxide from the atmosphere. The dataset to be provided by SWOT has the potential to provide vital information regarding changes in ocean mixing, and could aid in the study of changes in meridional overturning circulation and, in turn, our global climate.

APPENDICES

APPENDIX A

Sea surface height frequency-horizontal wavenumber and wavenumber spectral density figures to supplement Chapter III

A.1 Introduction

This appendix consists of eight figures that accompany Chapter III. These figures were not included in the chapter for the sake of brevity. In the chapter, frequency-horizontal wavenumber sea surface height variance spectral densities are computed from two simulations of the HYbrid Cooridinate Ocean Model (HYCOM) and three simulations of the Massachusetts Institute of Technology general circulation model (MITgcm) in seven regions of the world ocean. For the sake of brevity, the frequency-horizontal wavenumber spectral densities computed in all regions of only one simulation are shown in the main article file. Figures A.1-A.4 show the SSH frequency-horizontal wavenumber spectral densities in all seven regions in the remaining four simulations. This article also investigates the frequency content to wavenumber by integrating the frequency-horizontal wavenumber spectral densities over three frequency bands of interest: the subtidal band [$\omega < 0.86\,\mathrm{cpd}$], the tidal band [$0.87 <$

$\omega < 2.05\,\mathrm{cpd}$], and the supertidal band [$\omega > 2.06\,\mathrm{cpd}$]. Again, the article shows the frequency band integrated wavenumber spectral densities in all regions in just one simulation. Figures A.5-A.8 show the horizontal wavenumber spectral densities in all regions in the remaining four simulations.

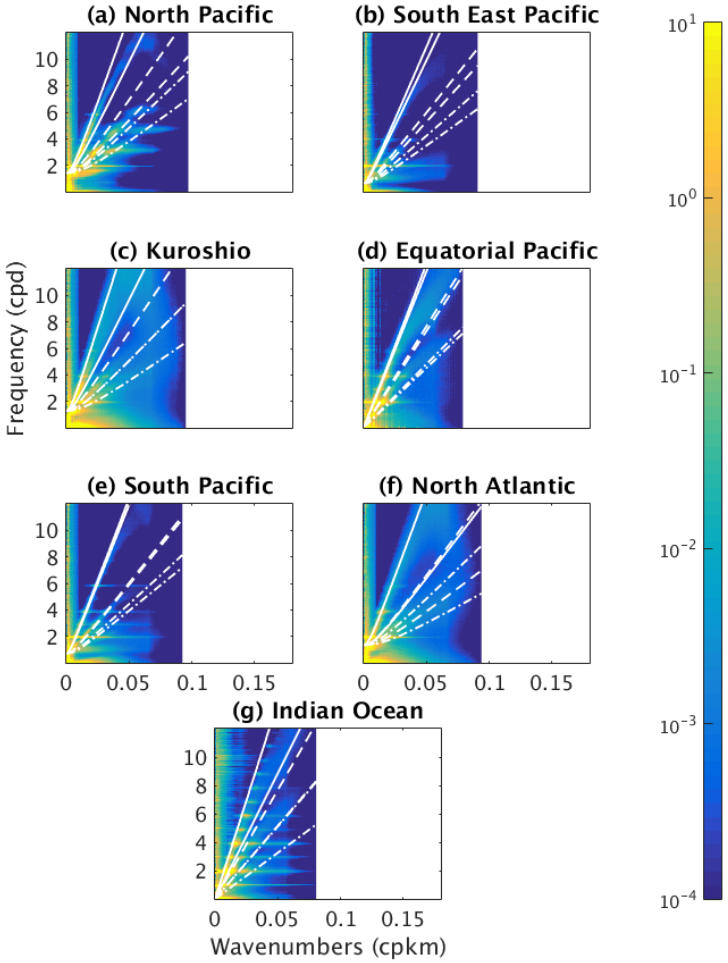

Figure A.1: Frequency-horizontal wavenumber spectral density of SSH variance [$\mathrm{cm}^2/(\mathrm{cpd\,cpkm})$] computed over seven regions from HYCOM12. Wavenumber axes are set to the maximum wavenumber for each region computed in HYCOM25. White curves show theoretical IGW linear dispersion relations for first (solid), second (dashed), and third (dashed-dotted) vertical modes. Bounding curves for each vertical mode are computed from the maximal and minimal eigenspeeds along the northern and southern boundaries, as in *Müller et al.* [2015]. Reprinted from *Savage et al.* (2017b).

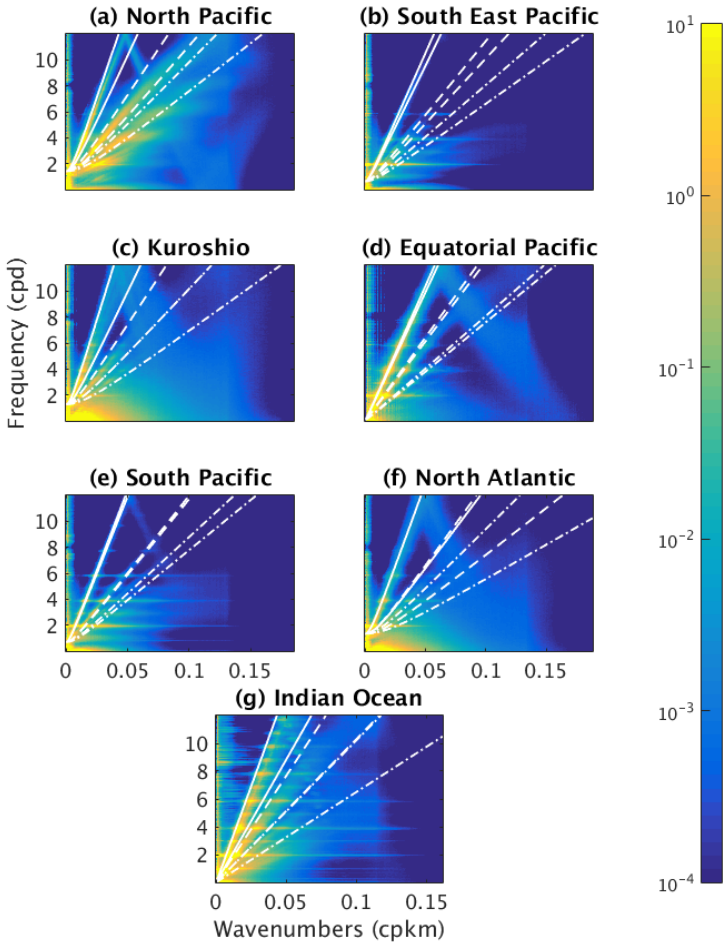

Figure A.2: Frequency-horizontal wavenumber spectral density of SSH variance [$\mathrm{cm}^2/(\mathrm{cpd\,cpkm})$] computed over seven regions from HYCOM25. Wavenumber axes are set to the maximum wavenumber for each region computed in HYCOM25. White curves show theoretical IGW linear dispersion relations for first (solid), second (dashed), and third (dashed-dotted) vertical modes. Bounding curves for each vertical mode are computed from the maximal and minimal eigenspeeds along the northern and southern boundaries, as in *Müller et al.* [2015]. Reprinted from *Savage et al.* (2017b).

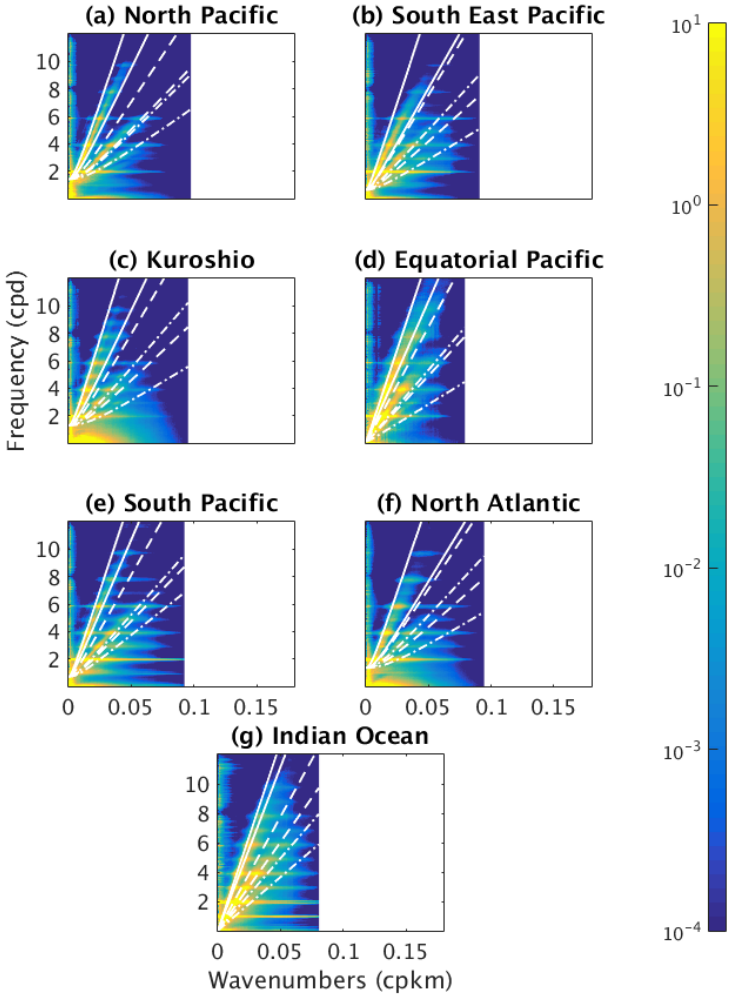

Figure A.3: Frequency-horizontal wavenumber spectral density of SSH variance [$\mathrm{cm}^2/(\mathrm{cpd\,cpkm})$] computed over seven regions from MITgcm12. Wavenumber axes are set to the maximum wavenumber for each region computed in HYCOM25. White curves show theoretical IGW linear dispersion relations for first (solid), second (dashed), and third (dashed-dotted) vertical modes. Bounding curves for each vertical mode are computed from the maximal and minimal eigenspeeds along the northern and southern boundaries, as in *Müller et al.* [2015]. Reprinted from *Savage et al.* (2017b).

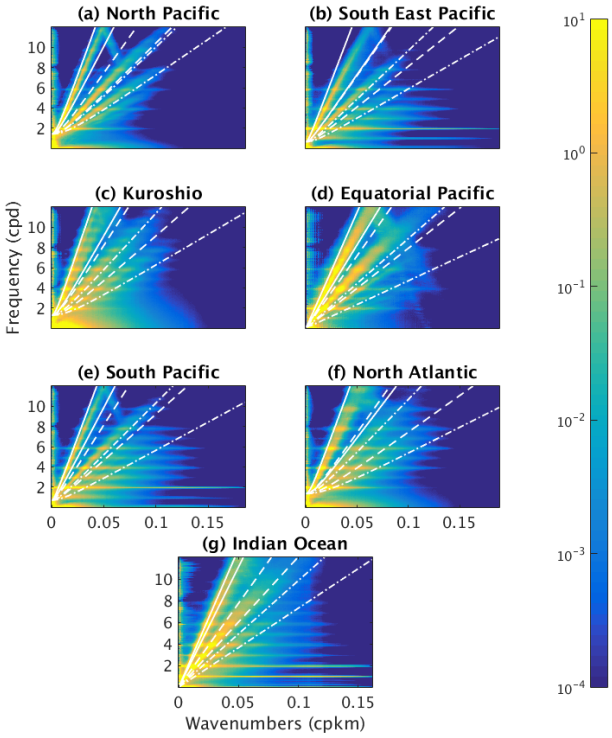

Figure A.4: Frequency-horizontal wavenumber spectral density of SSH variance [$\mathrm{cm}^2/(\mathrm{cpd\,cpkm})$] computed over seven regions from MITgcm24. Wavenumber axes are set to the maximum wavenumber for each region computed in HYCOM25. White curves show theoretical IGW linear dispersion relations for first (solid), second (dashed), and third (dashed-dotted) vertical modes. Bounding curves for each vertical mode are computed from the maximal and minimal eigenspeeds along the northern and southern boundaries, as in *Müller et al.* [2015]. Reprinted from *Savage et al.* (2017b).

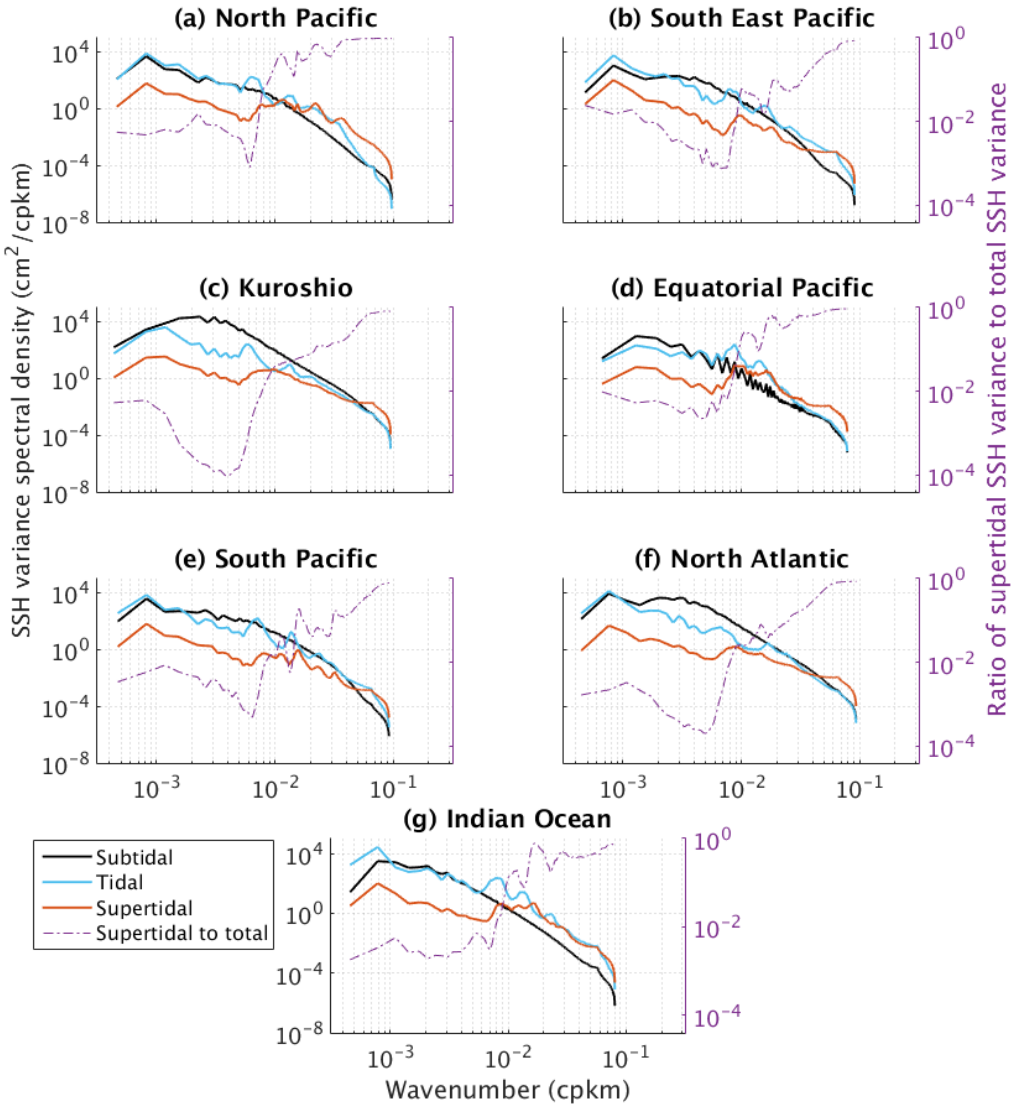

Figure A.5: Horizontal wavenumber SSH variance spectral density in all regions in HYCOM12 integrated over subtidal, tidal, and supertidal frequency bands (see text for definition of bands). The 95% confidence intervals span 76% to 137% of shown value for the subtidal band, 85% to 119% for the tidal band, and 94% to 107% for the supertidal band. Right-hand axis shows ratio of supertidal to total SSH variance as a function of isotropic wavenumber. Reprinted from *Savage et al.* (2017b).

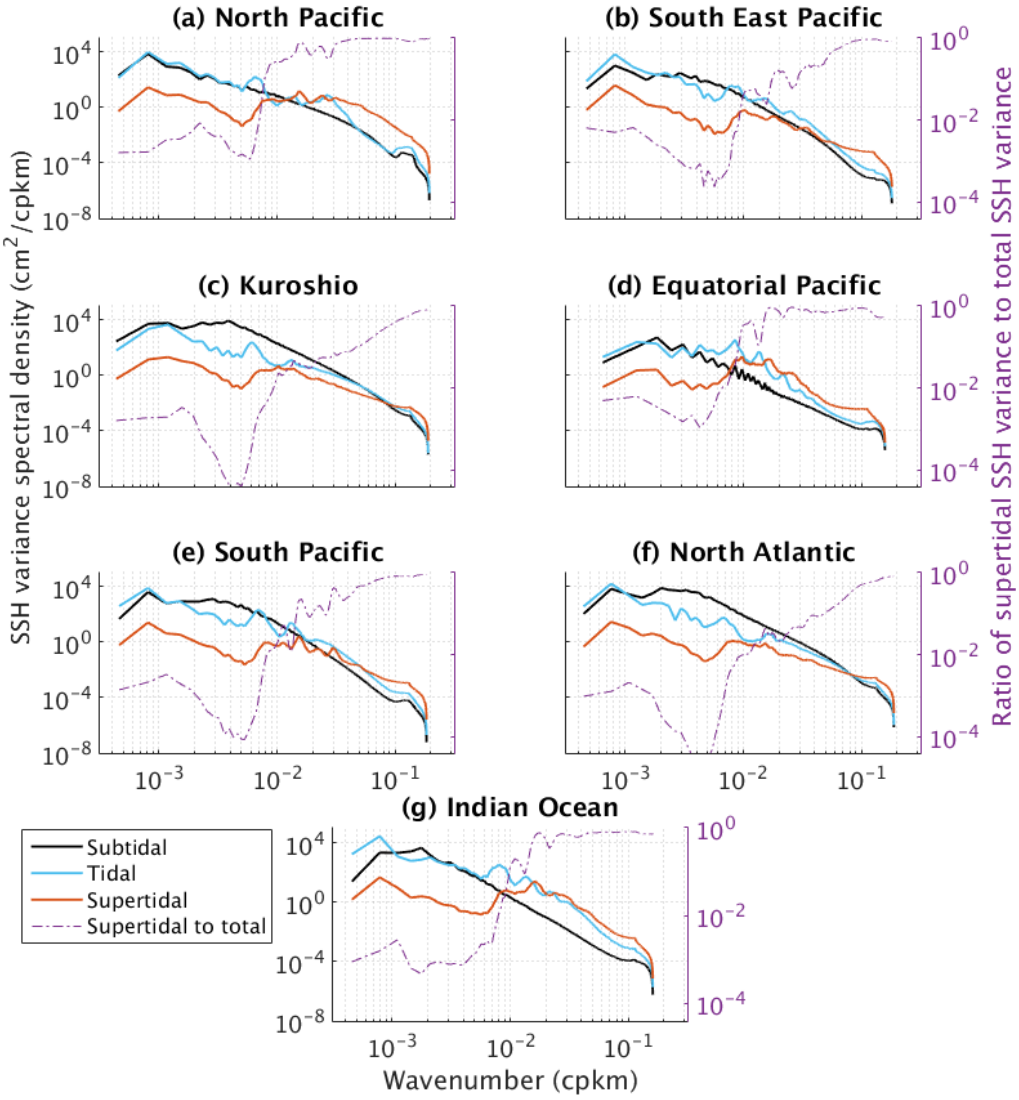

Figure A.6: Horizontal wavenumber SSH variance spectral density in all regions in HYCOM25 integrated over subtidal, tidal, and supertidal frequency bands (see text for definition of bands). The 95% confidence intervals span 76% to 137% of shown value for the subtidal band, 85% to 119% for the tidal band, and 94% to 107% for the supertidal band. Right-hand axis shows ratio of supertidal to total SSH variance as a function of isotropic wavenumber. Reprinted from *Savage et al.* (2017b).

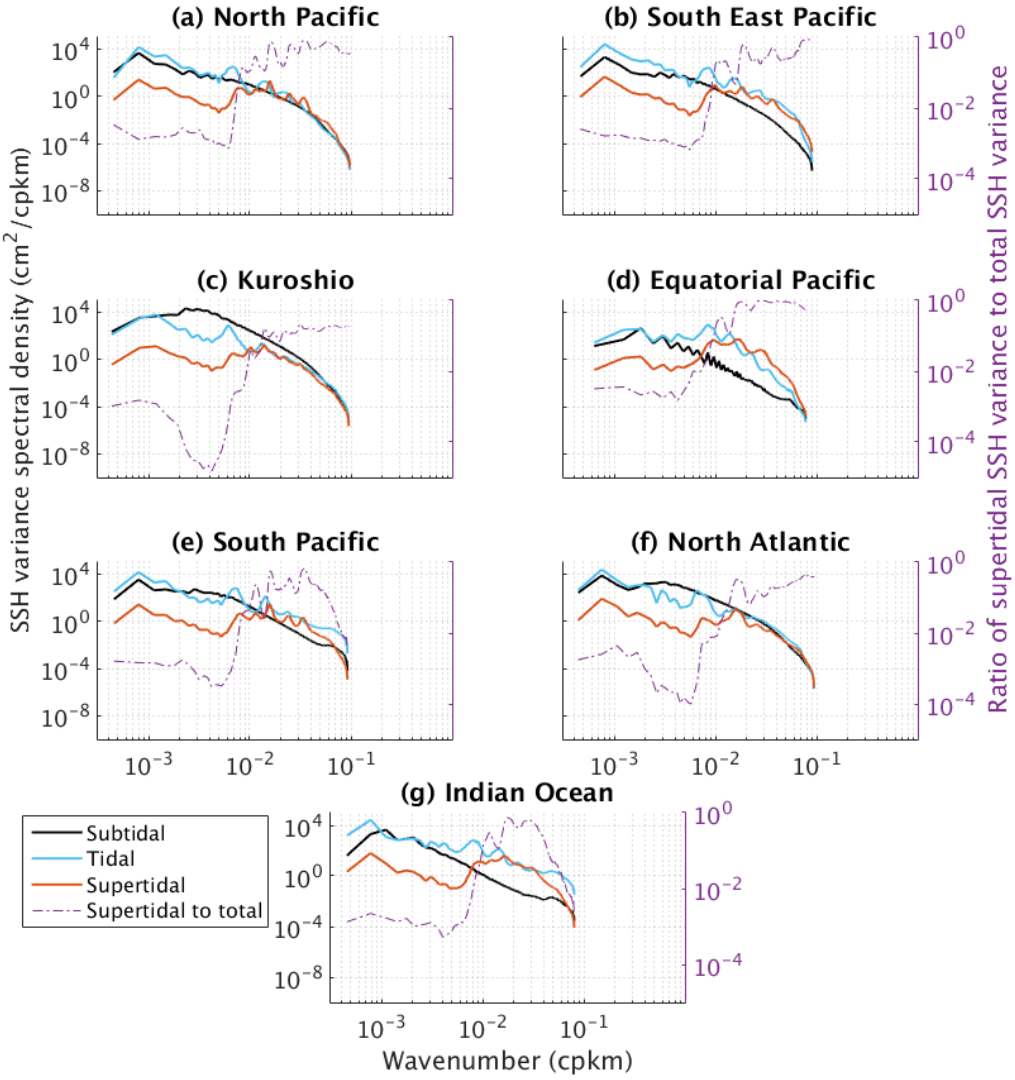

Figure A.7: Horizontal wavenumber SSH variance spectral density in all regions in MITgcm12 integrated over subtidal, tidal, and supertidal frequency bands (see text for definition of bands). The 95% confidence intervals span 76% to 137% of shown value for the subtidal band, 85% to 119% for the tidal band, and 94% to 107% for the supertidal band. Right-hand axis shows ratio of supertidal to total SSH variance as a function of isotropic wavenumber. Reprinted from *Savage et al.* (2017b).

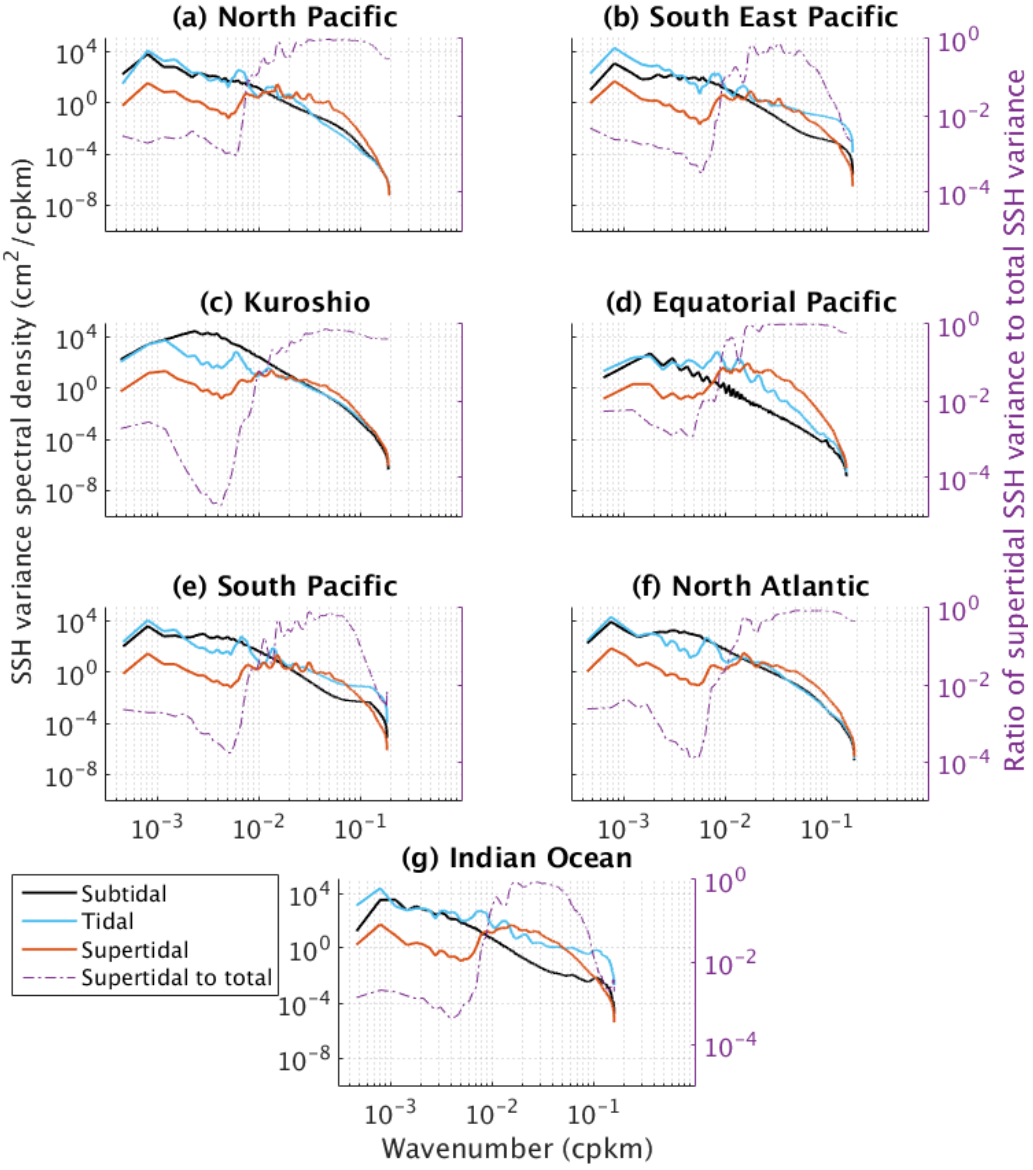

Figure A.8: Horizontal wavenumber SSH variance spectral density in all regions in MITgcm24 integrated over subtidal, tidal, and supertidal frequency bands (see text for definition of bands). The 95% confidence intervals span 76% to 137% of shown value for the subtidal band, 85% to 119% for the tidal band, and 94% to 107% for the supertidal band. Right-hand axis shows ratio of supertidal to total SSH variance as a function of isotropic wavenumber. Reprinted from *Savage et al.* (2017b).

APPENDIX B

Formulation of steric SSH in HYCOM

Steric sea surface height (SSH) is related to conservation of mass. We first assume local conservation of vertically integrated mass:

$$\rho_a(D + \eta_a^s) = \rho_b(D + \eta_b^s) \tag{B.1}$$

where

$$D = rest\, water\, column\, thickness$$

$$\rho_a = depth\, averaged\, density\, at\, time\, a$$

$$\rho_b = depth\, averaged\, density\, at\, time\, b$$

$$\eta_a^s = steric\, SSH\, at\, time\, a$$

$$\eta_b^s = steric\, SSH\, at\, time\, b.$$

We rewrite Equation 1 as:

$$\eta_b^s = \frac{\rho_a}{\rho_b}\eta_a^s + \frac{\rho_a - \rho_b}{\rho_b}D. \tag{B.2}$$

If we define time b as our time of interest, and time a as the long term mean, we can rewrite the standard steric SSH as

$$\eta^s = \frac{\bar{\rho}}{\rho}\bar{\eta^s} + \frac{\bar{\rho} - \rho}{\rho}D, \tag{B.3}$$

where the long term mean depth-averaged density, $\bar{\rho}$, is obtained from climatology or from a long term model mean, and ρ is the instantaneous depth-averaged density. We do not have an independent way to calculate mean steric SSH, $\bar{\eta^s}$, but we do have the total (steric plus non-steric) mean SSH, $\bar{\eta}$. Because most non-steric components are high-frequency, we assume the total mean SSH is entirely steric, i.e. $\bar{\eta^s} \approx \bar{\eta}$. HYCOM then calculates and writes out steric SSH as

$$\eta^s \approx \frac{\bar{\rho}}{\rho}\bar{\eta} + \frac{\bar{\rho} - \rho}{\rho}D. \tag{B.4}$$

BIBLIOGRAPHY

BIBLIOGRAPHY

Alford, M. H., J. A. MacKinnon, Z. Zhao, R. Pinkel, J. Klymak, and T. Peacock (2007), Internal waves across the Pacific, *Geophys. Res. Lett.*, *34*(L24601), doi: doi:10.1029/2007GL031566.

Alford, M. H., et al. (2011), Energy flux and dissipation in Luzon Strait: Two tales of two ridges, *J. Phys. Oceanogr.*, *41*(11), 2211–2222.

Alford, M. H., et al. (2015), The formation and fate of internal waves in the South China Sea, *Nature*, *521*, 65–69, doi:10.1038/nature14399.

Alley, R. B. (2007), Wally was right: Predictive ability of the North Atlantic Conveyer Belt hypothesis for abrupt climate change, *Annual Review of Earth and Planetary Sciences*, *35*, 241–272, doi:10.1146/annurev.earth.35.081006.131524.

Ansong, J. K., B. K. Arbic, M. C. Buijsman, J. G. Richman, J. F. Shriver, and A. J. Wallcraft (2015), Indirect evidence for substantial damping of low-mode internal tides in the open ocean, *Journal of Geophysical Research Oceans*, *120*, 7997–8019, doi:10.1002/2015JC010998.

Ansong, J. K., et al. (2017), Semidiurnal internal tide energy fluxes and their variability in a global ocean model and moored observations, *Journal of Geophysical Research–Oceans*, doi:10.1002/2016JC012184.

Arbic, B. K., S. T. Garner, R. W. Hallberg, and H. L. Simmons (2004), The accuracy of surface elevations in forward global barotropic and baroclinic tide models, *Deep Sea Research Part II: Topical Studies in Oceanography*, *51*, 3069–3101, doi: 10.1016/j.dsr2.2004.09.014.

Arbic, B. K., J. X. Mitrovica, D. R. MacAyeal, and G. A. Milne (2008), On the factors behind large Laborador Sea tides during the last glacial cycle and the potential implications for heinrich events, *Paleoceanography*, *23*, doi:10.1029/2007PA001573.

Arbic, B. K., A. J. Wallcraft, and E. J. Metzger (2010), Concurrent simulation of the eddying general circulation and tides in a global ocean model, *Ocean Modelling*, *32*, 175–187, doi:10.1016/j.ocemod.2010.01.007.

Arbic, B. K., J. G. Richman, J. F. Shriver, P. G. Timko, E. J. Metzger, and A. J. Wallcraft (2012), Global modeling of internal tides within an eddying ocean general circulation model, *Oceanography*, *25*, 20–29, doi:10.5670/oceanog.2012.38.

Buijsman, M. C., B. K. Arbic, J. A. M. Green, R. W. Helber, J. G. Richman, J. F. Shriver, P. G. Timko, and A. J. Wallcraft (2015), Optimizing internal wave drag in a forward barotropic model with semidiurnal tides, *Ocean Modelling*, *85*, 42–55.

Buijsman, M. C., J. K. Ansong, B. K. Arbic, J. G. Richman, J. F. Shriver, P. G. Timko, A. J. Wallcraft, C. B. Whalen, and Z. Zhao (2016), Impact of parameterized internal wave drag on the semidiurnal energy balance in a global ocean circulation model, *Journal of Physical Oceanography*, *46*, doi:10.1175/JPO-D-15-0074.1.

Caldwell, P. C., M. A. Merrifield, and P. R. Thompson (2015), Sea level measured by tide gauges from the global oceans-the Joint Archive for Sea Level holdings (NCEI Accession 0019568), Version 5.5, NOAA National Centers for Environmental Information, Dataset, doi:10.7289/V5V40S7W.

Callies, J., and R. Ferrari (2013), Interpreting energy and tracer spectra of upper-ocean turbulence in the submesoscale range (1-200 km), *Journal of Physical Oceanography*, *43*, doi:10.1175/JPO-D-13-063.1.

Carrère, L., and F. Lyard (2003), Modeling the barotropic response of the global ocean to atmospheric wind and pressure forcing: Comparison with observations, *Geophysical Research Letters*, *30*, 1275, doi:10.1029/2002GL016473.

Cartwright, D. E. (1999), *Tides: A Scientific History*, 192 pp., Cambridge Univ. Press, Cambridge, U. K.

Chambers, D. P. (2006), Observing seasonal steric sea level variations with GRACE and satellite altimetry, *Journal of Geophysical Research*, *3*, doi: 10.1029/2005JC002914.

Chassignet, E. P., et al. (2009), Global ocean prediction with the HYbrid Coordinate Ocean Model (HYCOM), *Oceanography*, *22*, 64–76.

D'Asaro, E. A. (1984), Wind forced internal waves in the north pacific and sargasso sea, *Journal of Physical Oceanography*, *14*, 781–794.

Dee, D. P., et al. (2011), The ERA-interim reanalysis: Configuration and performance of the data assimilation system, *Quarterly Journal of The Royal Meteorological Society*, *137*, 553–597, doi:10.1002/qj.828.

Doherty, K. W., D. E. Frye, S. P. Liberatore, and J. M. Toole (1999), A moored profiling instrument, *Journal of atmospheric and ocean technology*, *16*, 1816–1829, doi:http://dx.doi.org/10.1175/1520-0426(1999)016¡1816:AMPI¿2.0.CO;2.

Ducet, N., P. Y. L. Traon, and G. Reverdin (2000), Global high-resolution mapping of ocean circulation from TOPEX/Poseidon and ERS-1 and -2, *Journal of Geophysical Research*, *105*, 19,477–19,498, doi:10.1029/2000JC900063.

Dushaw, B. D., P. F. Worcester, and M. A. Dzieciuch (2011), On the predictability of mode-1 internal tides, *Deep-Sea Research Part 1*, *58*, 677–698, doi: 10.1016/j.dsr.2011.04.002.

Egbert, G. D., and R. D. Ray (2003), Semi-diurnal and diurnal tidal dissipation from TOPEX/Poseidon altimetry, *Geophysical Research Letters*, *30*, doi: 10.1029/2003GL017676.

Egbert, G. D., A. F. Bennett, and M. G. G. Foreman (1994), TOPEX/POSEIDON tides estimated using a global inverse model, *Journal of Geophysical Research*, *99*, 24,821–24,852.

Egbert, G. D., R. D. Ray, and B. G. Bills (2004), Numerical modeling of the global semidiurnal tide in the present day and in the last glacial maximum, *Journal of Geophysical Research*, *109*, doi:10.1029/2003JC001973.

Erofeeva, S. Y., G. D. Egbert, and P. M. Kosro (2003), Tidal currents on the central Oregon coast: Models, data, and assimilation, *Journal of Geophysical Research*, *108*, doi:10.1029/2002JC001615.

Ferrari, R., and C. Wunsch (2009), Ocean circulation kinetic energy: Resevoirs, sources, and sinks, *Annual Review of Fluid Mechanics*, *41*, 253–282, doi: 10.1146/annurev.fluid.40.111406.102139.

Fu, L. L., and A. Cazenave (Eds.) (2001), *Satellite Altimetry and Earth Sciences: A Handbook of Techniques and Applications*, Academic, San Diego, Calif.

Fu, L. L., and D. B. Chelton (2001), Large-scale ocean circulation, in *Satellite Altimetry and Earth Sciences: A Handbook of Techniques and Applications*, edited by L.-L. Fu and A. Cazanave, chap. 2, pp. 133–169, Academic Press.

Fu, L. L., D. Alsdorf, R. Morrow, E. Rodriguez, and N. Mognard (Eds.) (2012), *SWOT: The Surface Water and Ocean Topography Mission: Wide-Swatch Altimetric Measurement of Water Elevation on Earth, JPL-Publication*, 228 pp., Jet Propul. Lab., Pasadena, Calif.

Garrett, C., and W. Munk (1972), Space-time scales of internal waves, *Journal of Geophysical Research*, *2*, 225–264.

Garrett, C., and W. Munk (1975), Space-time scales of internal waves: A progress report, *Journal of Geophysical Research*, pp. 291–297, doi:10.1029/JC080i002p00291.

Gill, A. E. (1982), *Atmosphere-Ocean Dynamics*, Academic, San Diego, California.

Glazman, R. E., and B. Cheng (1999), Altimeter observations of baroclinic oceanic inertia-gravity wave turbulence, *Proceedings of the Royal Society A*, *455*, 90–123, doi:10.1098/rspa.1999.0304.

Harris, F. J. (1976), Windows, harmonic analysis, and the discrete Fourier transform, Undersea Surveillance Department, Naval Undersea Center, San Diego, CA.

Hastenrath, S. (1982), On meridonal heat transports in the world ocean, *Journal of Physical Oceanography*, *12*, 922–927.

Hendershott, M. C. (1972), The effects of solid earth deformation on global ocean tides, *Geophys. J. R. Astron. Soc.*, *29*, 389–402, doi:10.1111/j.1365-246X.1972.tb06167.x.

Hennessy, K., B. Fitzharris, B. C. Bates, N. Harvey, S. M. Howden, L. Hughes, J. Salinger, and R. Warrick (2007), Australia and new zealand, in *Climate Change 2007: Impacts, Adaptation and Vulnerability. Contribution of Working Group II to the Fourth Assessment Report of the Intergovernmental Panel on Climate Change*, edited by M. L. Parry, O. F. Canziani, J. P. Palutikof, P. J. van der Linden, and C. E. Hanson, pp. 507–540, Cambridge University Press, Cambridge, UK.

Hogan, T. F., et al. (2014), The Navy Global Environemental Model, *Oceanography*, *27*, 116–125, doi:10.5670/oceanog.2014.73.

Houghton, J. T., Y. Ding, D. J. Griggs, M. Noguer, P. J. van der Linden, X. Dai, K. Maskell, and C. A. Johnson (Eds.) (2001), *Climate Change 2001: The Scientific Basis*, Cambridge University Press, Cambridge, U. K.

Jakobsson, M., R. Macnab, L. Mayer, R. Anderson, M. Edwards, J. Hatzky, H. W. Schenke, and P. Johnson (2008), An improved bathymetric portrayal of the Arctic Ocean: implications for ocean modeling and geological, geophysical and oceanographic analyses, *Geophysical Research Letters*, *35*, doi:10.1029/2008GL033520.

Jan, S., R. Lien, and C. Ting (2008), Numerical study of baroclinic tides in Luzon Strait, *Journal of Oceanography*, *64*, 789–802, doi:10.1007/s10872-008-0066-5.

Jayne, S. R., and L. C. St. Laurent (2001), Parameterizing tidal dissipation over rough topography, *Geophysical Research Letters*, *28*, 811–814.

Knauss, J. A. (1997), *Introduction to Physical Oceanography*, 2nd ed., Waveland Press, Inc., 4180 IL Route 83, Suite 101, Long Grove, IL 60047.

Kundu, P. K. (1990), *Fluid Mechanics*, Academic Press, San Diego, CA, USA.

Large, W., J. McWilliams, and S. Doney (1994), Oceanic vertical mixing: A review and a model with nonlocal boundary layer parameterization, *Reviews in Geophysics*, *32*, 363–403.

Large, W. G., and S. G. Yeager (2004), Diurnal and decadal global forcing for ocean and sea-ice models: The data sets and climatologies, NCAR Tech. Note, Boulder, CO, 105 pp., doi:10.5065/D6KK98Q6, tN–460+ST (May).

Le Provost, C. (2001), Ocean tides, in *Satellite Altimetry and Earth Sciences*, edited by L.-L. Fu and A. Cazenave, chap. 6, pp. 267–304, Academic Press.

Le Quéré, C., et al. (2007), Saturation of Southern Ocean CO_2 sink due to recent climate change, *Science*, doi:10.1126/science.1136188.

Le Traon, P. Y., and R. Morrow (2001), Ocean currents and eddies, in *Satellite Altimetry and Earth Sciences: A Handbook of Techniques and Applications*, edited by L.-L. Fu and A. Cazanave, chap. 3, pp. 171–215, Academic Press.

Le Traon, P. Y., P. Klein, B. L. Hua, and G. Dibarboure (2008), Do altimeter wavenumber spectra agree with the interior or surface quasi-geostrophic theory?, *Journal of Physical Oceanography*, *38*, 1137–1142, doi:10.1175/2007JPO3806.1.

Leith, C. E. (1996), Stochastic models of chaotic systems, *Physica D.*, *98*, 481–491.

Levitus, S., J. I. Antonov, J. Wang, T. L. Delworth, K. W. Dixon, and A. J. Broccoli (2001), Anthropogenic warming of earth's climate system, *Science*, *292*, 267–270.

Losch, M., D. Menemenlis, J.-M. Campin, P. Heimbach, and C. N. Hill (2010), On the formulation of sea-ice models. part 1: effects of different solver implementations and parameterizations, *Ocean Modelling*, *33*, 129–144, doi: 10.1016/j.ocemod.2009.12.008.

Lumley, J. L. (1970), *Stochastic Tools in Turbulence*, 100 pp., Dover Publications, Inc., Mineola, NY.

MacKinnon, J. A., M. H. Alford, R. Pinkel, J. Klymak, and Z. Zhao (2013a), The latitudinal dependence of shear and mixing in the Pacific transiting the critical latitude for PSI, *J. Phys. Oceanogr.*, *43*(1), 3–16.

MacKinnon, J. A., M. H. Alford, O. Sun, R. Pinkel, Z. Zhao, and J. Klymak (2013b), Parametric Subharmonic Instability of the internal tide at 29N, *J. Phys. Oceanogr.*, *43*(1), 17–28.

Marshall, J., A. Adcroft, C. Hill, L. Perelman, and C. Heisey (1997), A finite-volume, incompressible navier stokes model for studies of the ocean on parallel computers, *Journal of Geophysical Research*, *102*, 5753–5766, doi:10.1029/96JC02775.

Martini, K. I., M. H. Alford, S. Kelly, and J. D. Nash (2011), Observations of internal tides on the Oregon Continental Slope, *J. Phys. Oceanogr.*, *41*(9), 1772–1794.

Martini, K. I., M. H. Alford, E. Kunze, S. M. Kelly, and J. D. Nash (2013), Internal bores and breaking internal tides on the Oregon continental slope, *J. Phys. Oceanogr.*, *43*(1), 120–141.

Menemenlis, D., J.-M. Campin, P. Heimbach, C. N. Hill, T. Lee, A. T. Nguyen, M. P. Schodlok, and H. Zhang (2008), ECCO2: High resolution global ocean and sea ice data synthesis, Mercator Ocean Quarterly Newsletter, 13–21 pp.

Moum, J. N., and W. D. Smyth (2000), Upper ocean mixing, Oregon State University.

Müller, M., B. K. Arbic, J. G. Richman, J. F. Shriver, E. L. K. R. B. Scott, A. J. Wallcraft, and L. Zamudio (2015), Toward and internal gravity wave spectrum in global ocean models, *Geophysical Research Letters*, *42*, 3474–3481, doi: 10.1002/2015GL063365.

Munk, W. (1981), Internal waves and small-scale processes, in *Evolution of Physicsl Oceanography: Scientific Surveys in Honor of Henry Stommel*, chap. 9, pp. 264–291, The MIT Press, Cambridge and London.

Munk, W., and C. Wunsch (1998), Abysall recipes II: energetics of tidal and wind mixing, *Deep Sea Research Part 1 Oceanographic Research Papers*, *45*, 1977–2010.

Nash, J. D., M. H. Alford, E. Kunze, K. I. Martini, and S. Kelly (2007), Hotspots of deep ocean mixing on the Oregon continental slope, *Geophys. Res. Lett.*, *34*(L01605), doi:10.1029/2006GL028,170.

Ngodock, H. E., I. Souopgui, A. J. Wallcraft, J. G. Richman, J. F. Shriver, and B. K. Arbic (2016), On improving the accuracy of the M_2 barotropic tides embedded in a high-resolution global ocean circulation model, *Ocean Modelling*, *97*, 16–26, doi:10.1016/j.ocemod.2015.10.011.

Ponte, R., and P. Gaspar (1999), Regional analysis of the inverted barometer effect over the global ocean using TOPEX/POSEIDON data and model results, *Journal of Geophysical Research*, *104*, 15,587–15,601, doi:10.1029/1999JC900113.

Ponte, R. M., A. H. Chaudhuri, and S. V. Vinogradov (2015), Long-period tides in an atmospherically driven, stratified ocean, *Journal of Physical Oceanography*, *45*, 1917–1928, doi:10.1175/JPO-D-15-0006.1.

Qiu, B., T.Nakano, S. Chen, and P. Klein (2017), Submesoscale transition from geostrophic flows to internal waves in the northwestern Pacific upper ocean, *Nature Communications*, doi:10.1038/ncomms14055.

Ray, R. D. (1998), Spectral analysis of highly aliased sea-level signals, *Journal of Geophysical Research*, *103*, 24,991–25,003.

Ray, R. D. (1999), A global ocean tide model from TOPEX/POSEIDON altimetry: GOT99.2., National Aeronautics and Space Administration Technical Memorandum, 58pp pp., nASA/TM-1999-209478.

Ray, R. D. (2007), Propogation of the overtide M_4 through the deep Atlantic Ocean, *Geophysical Research Letters*, *34*, doi:10.1029/2007GL031618.

Ray, R. D., and D. A. Byrne (2010), Bottom pressure tides along a line in the southern Atlantic Ocean and comparisons with satellite altimetry, *Ocean Dynamics*, *60*, 1167–1176, doi:10.1007/s10236-010-0316-0.

Ray, R. D., and G. T. Mitchum (1997), Surface manifestation of internal tides in the deep ocean: observations from altimetry and island gauges, *Prog. Oceanog.*, *40*, 135–162, doi:10.1016/S0079-6611(97)00025-6.

Ray, R. D., and E. D. Zaron (2016), M_2 internal tides and their observed wavenumber spectra from satellite altimetry, *Journal of Physical Oceanography*, *46*, 3–22, doi: 10.1175/JPO-D-15-0065.1.

Richman, J. G., B. K. Arbic, J. F. Shriver, E. J. Metzger, and A. J. Wallcraft (2012), Inferring dynamics from the wavenumber spectra of an eddying global ocean model with embedded tides, *Journal of Geophysical Research*, *117*, doi: 10.1029/2012JC008364.

Rocha, C. B., T. K. Chereskin, S. T. Gille, and D. Menemenlis (2016a), Mesoscale to submesoscale wavenumber spectra in Drake Passage, *Journal of Physical Oceanography*, *46*, doi:10.1175/JPO-D-15-0087.1.

Rocha, C. B., S. T. Gille, T. K. Chereskin, and D. Menemenlis (2016b), Seasonality of submesoscale dynamics in the Kuroshio Extension, *Geophysical Research Letters*, doi:10.1002/2016GL071349.

Roemmich, D., and W. B. Owens (2000), The Argo Project: observing the global ocean with profiling floats, *Oceanography*, *13*, 45–50, doi:10.5670/oceanog.2000.33.

Sasaki, H., and P. Klein (2012), Ssh wavenumber spectra in the north pacific from a high-resolution realistic simulation, *Journal of Physical Oceanography*, *42*, 1233–1241, doi:10.1175/JPO-D-11-0180.1.

Savage, A. C., et al. (2017a), Frequency content of sea surface height variability from internal gravity waves to mesoscale eddies, *Journal of Geophysical Research–Oceans*, doi:10.1002/2016JC012331.

Savage, A. C., et al. (2017b), Spectral decomposition of internal gravity wave sea surface height in global models, *Journal of Geophysical Research–Oceans*, in review.

Shriver, J. F., and H. E. Hurlburt (2000), The effect of upper ocean eddies on the non-steric contribution to the barotropic tide, *Geophysical Research Letters*, *27*, 2713–2716.

Shriver, J. F., B. K. Arbic, J. G. Richman, R. D. Ray, E. J. Metzger, A. J. Wallcraft, and P. G. Timko (2012), An evaluation of the barotropic and internal tides in a high resolution global ocean circulation model, *Journal of Geophysical Research*, *17*, doi:10.1029/2012JC008170.

Smagorinsky, J. (1993), Large eddy simulation of complex engineering and geophysical flows, in *Evolution of Physical Oceanography*, edited by B. Galperin and S. A. Orszag, pp. 3–36, Cambridge University Press.

Smith, W. H. F., and D. T. Sandwell (1997), Global sea floor topography from satellite altimetry and ship depth soundings, *Science*, *277*, 1956–1962, doi: 10.1126/science.277.5334.1956.

Soufflet, Y., P. Marchesiello, F. Lemarié, J. Jouanno, X. Capet, L. Debreu, and R. Benshila (2016), On effective resolution in ocean models, *Ocean MOdelling*, *98*, 36–50, doi:http://dx.doi.org/10.1016/j.ocemod.2015.004.

Stammer, D. (1997), Global characteristics of ocean variability estimated from regional TOPEX/poseidon altimeter measurements, *Journal of Physical Oceanography*, *27*, 1743–1769, doi:10.1175/1520-0485(1997)027¡1743:GCOOVE¿2.0.CO;2.

Stammer, D., C. Wunsch, and R. M. Ponte (2000), De-aliasing of global high-frequency barotropic motions in altimeter observations, *Geophys. Res. Lett.*, *27*, 1175–1178.

Stammer, D., et al. (2014), Accuracy assessment of global barotropic ocean tide models, *Reviews of Geophysics*, *52*, 243–282, doi:10.1002/2014RG000450.

Tierney, C. C., J. Whar, F. Bryan, and V. Zlotnicki (2000), Short-period oceanic circulation: Implications for satellite altimetry, *Geophys. Res. Lett*, *27*, 1255–1258.

Timko, P. G., B. K. Arbic, J. G. Richman, R. B. Scott, E. J. Metzger, and A. J. Wallcraft (2012), Skill test of three-dimensional tidal currents in global ocean model: A look at the North Atlantic, *Journal of Geophysical Research*, *117*, doi: 10.1029/2011JC007617.

Timko, P. G., B. K. Arbic, J. G. Richman, R. B. Scott, E. J. Metzger, and A. J. Wallcraft (2013), Skill testing a three-dimensional global tide model to historical current meter records, *Journal of Geophysical Research*, doi:10.1002/2013JC009071, in press.

Whalen, C. B., L. D. Talley, and J. A. MacKinnon (2012), Spatial and temporal variability of global ocean mixing inferred from argo profiles, *Geophysical Research Letters*, *39*, doi:10.1029/2012GL053196.

Wunsch, C. (1991), Global-scale surface variability from combined altimetric and tide gauge measurements, *Journal of Geophysical Research*, *96*, 15,053–15,082.

Wunsch, C., and R. Ferrari (2004), Vertical mixing, energy, and the general circulation of the ocean, *Annual Review of Fluid Mechanics*, *36*, 281–314, doi: 10.1146/annurev.fluid.36.05082.122121.

Xu, Y., and L.-L. Fu (2012), The effects of altimeter instrument noise on the estimation of the wavenumber spectrum of sea surface height, *Journal of Physical Oceanography*, *42*, 2229–2233, doi:10.1175/JPO-D-12-0106.1.

Zaron, E. D. (2015), Non-stationary internal tides observed using dual-satellite altimetry, *Journal of Physical Oceanography*, *45*, 2239–2246, doi:10.1175/JPO-D-15-0020.1.

Zaron, E. D. (2017), Mapping the non-stationary internal tides with satellite altimetry, *Journal of Geophysical Research*, at press.

Zhao, Z., M. H. Alford, J. A. MacKinnon, and R. Pinkel (2010), Long-range propagation of the semidiurnal internal tide from the Hawaiian Ridge, *J. Phys. Oceanogr.*, *40*(4), 713–736.

Zhao, Z., M. H. Alford, J. B. Girton, L. Rainville, and H. L. Simmons (2016), Global observations of open-ocean mode-1 M_2 internal tides, *Journal of Physical Oceanography*, *46*, 1657–1684, doi:10.1175/JPO-D-15-0105.1.

Zilberman, N. V., M. A. Merrifield, G. S. Carter, D. S. Luther, M. D. Levine, and T. J. Boyd (2011), Incoherent nature of M_2 internal tides at the Hawaiian ridge, *Journal of Physical Oceanography*, *41*, 2021–2036, doi:10.1175/JPO-D-10-05009.1.